UNIVERSITÀ POLITECNICA DELLE MARCHE

FACOLTÀ DI INGEGNERIA

Master's Degree in BIOMEDICAL ENGINEERING

Curriculum: Engineering of Medical Devices

3D Bioprinting of cell-laden nanocellulose based hydrogel bioink for auricle reconstruction

Supervisor:

Prof.ssa Alida Mazzoli

Candidate:

Sara Frezzotti

Co-supervisors:

Prof.ssa Pasquapina Ciarmela

Prof.ssa Francesca Luzi

A.Y. 2023/2024

ABSTRACT

Auricular reconstruction due to birth defects, trauma or cancer is very demanding and challenging. The external ear is a single piece of elastic cartilage with complex architecture made up of different detailed components. Having the extracellular matrix (ECM) primarily composed by collagen, auricular cartilage has viscoelastic properties. Recently, three-dimensional (3D) bioprinting has been proposed as a promising method for cartilage replacement. It is an additive manufacturing strategy that deposits layer by layer a special material called 'bioink'. There are different bioprinting approaches among which extrusion-based bioprinting that exploits pneumatic pressure or mechanical force to extrude the bioink through a nozzle orifice. A typical bioprinting process consists in the creation of a digital design that is sent to the bioprinting system where the bioink is loaded and finally the printed construct is transferred into the bioreactor for tissue-maturation. Indeed, the bioink is a material composed of living cells suspended in a polymer acting as a glue to adhere cells for assembling 3D live structure and providing a similar environment as *in vivo*. The bioink must be biocompatible as well as printable. Among the bioink-materials there are the hydrogels, a type of soft material composed of crosslinked hydrophilic polymers forming a 3D network structure, that have attracted attention as promising matrices for bioinks because of their low toxicity and high-water content. They divide into synthetic and natural hydrogels. The second are preferable since they are superior in terms of biocompatibility, biodegradability and bioactivity, although their lower mechanical and printability characteristics. The bioink is usually subjected to several tests to identify if it meets the biological, and the mechanical and printability requirements: rheological analysis, characterization tests, biological analysis through imaging techniques. 3D bioprinting has gained attention as potential and alternative method for elastic cartilage, with respect to autologous graft and synthetic implants, because the resulted engineered auricular implant should ideally exhibit biochemical and mechanical properties that are more similar to the native tissue. Among the natural hydrogels that better mimic *in vivo* condition of auricular cartilage there is alginate. Despite its availability, biological characteristics and structural similarity to ECM, alginate has poor structural fidelity and mechanical stiffness. One strategy to strengthen alginate is to combine it with other natural gels such as nanocellulose (NC) that has gained increased interest due to its mechanical characteristics. Despite the primary cells of the auricular cartilage are chondrocytes, it does not exist one single type of cell that is generally accepted as the best cell resource for the bioink. Before being tested and manageable, the bioink must be crosslinked. Among the crosslinking strategies for alginate-based hydrogels there are ionic and free radical polymerization crosslinking: the second one provides better stability than the first one. In this thesis a hybrid bioink composed of Sodium-Alginate

and Crystalline Nanocellulose (CNC) was realized and its suitability for extrusion-based bioprinting explored. Different bioink formulations were prepared and compared with concern to printability, shape fidelity post-printing and post-crosslinking as well as swelling and degradation behaviour in culture medium. The printability of the tested bioinks enabled printing of both two-dimensional (2D) structures and 3D constructs. The structures were crosslinked by using $CaCl_2$ at different concentrations and combined with $BaCl_2$ to identify the crosslinker that enabled the least structural deformation. The best sample, according to the tests done, was employed in the auricular structure printing by using a 3D Computer-aided design (CAD) model as blueprint. Finally, human fibroblast cells were printed in the selected hybrid bioink. CNC-based bioinks demonstrated good shear-thinning behaviour and swelling behaviour, essential characteristic for 3D bioprinting. The selected bioink, 3 % w/v alginate combined with 4 % w/v CNC, demonstrated superior shape fidelity post-printing, with only 0.88 mm^2 of mean area discrepancy, and post-crosslinking, with only 6.49 % of deformation. Furthermore, it showed well-preserved stability and mechanical properties 7 days after immersion in culture medium at 37°, releasing only 38.45 % of gel. Crosslinker with barium enhanced the scaffold stability. Finally, microscopy analysis has revealed the sustained capacity of the CNC-based scaffold to promote cellular adhesion, growth and aggregation. All these results confirmed the potential use of the produced cost-effective CNC-based hydrogel for 3D bioprinting of living tissues and organs, like the auricle.

INDEX

INTRODUCTION

Auricular reconstruction is one of the greatest challenges and sophisticated operations for plastic surgeons, as it demands to produce a complex structure that should be durable and aesthetically pleasant. Malformations of auricle can be due to birth defects, trauma, infections, burns or cancer, and they have a significant effect on physiological function, psychological and social status, personal development and even the least ones could influence the quality of life. Although the great demand for partial ear reconstruction, there is also a relatively low percentage of patients needing total reconstruction (e.g. microtia) [1]. Microtia, translated form Greek, means 'little ear' and it is a medical word used to indicate a small or absent ear in newborn babies. Affecting one in around 8000-10000 births, microtia can be unilateral or bilateral, even if ninety percent of cases are unilateral, with the right side being affected more frequently than the left. It is more prevalent in males than females, and it can appear in isolation or as a consequence of other syndromes such as Hemifacial microsomia or Treacher Collins syndrome [2].

Currently, the standard procedure for ear reconstruction is using autologous cartilage, in particular rib one. Even if this surgical technique has been used in clinical practice for decades, there still exist a variety of risks, including donor site morbidity and long-term complications. To overcome these difficulties, alloplastic materials have been advocated as substitutes for autologous tissue, such as silicone and polyethylene. Despite synthetic materials convey superiority in terms of printability and mechanical characteristics, as well as shape preservation, they are associated with risks of infection, extrusion, no biocompatibility and uncertain long-term durability which may limit their applicability in a clinical setting [3]. Thus, considering the disadvantages of the traditional methods applied for auricular cartilage reconstructions, researchers and clinicians are seeking for novel implants that can maintain their shape without absorption in the body, and can simultaneously promote tissue regeneration. Recently, three-dimensional (3D) bioprinting, as an advancement of conventional tissue engineering (TE) approaches, has been proposed as a potential method for cartilage replacement. It is an additive manufacturing strategy that deposits layer by layer a special material called 'bioink' to generate tissue-like structures. [4]. The goal of 3D bioprinting for ear reconstruction is 'to produce 3D artificial tissues consisting of cells, scaffold and a microenvironment which mimic the *in vivo* condition of auricular cartilage'. According to previous studies, the most preferred cells sources for cartilage tissue are chondrocytes but alternatives can be evaluated too, finding the best compromise among ready availability, high proliferation rate and the most optimal type for the considered tissue. As concerns biomaterials, chondrocytes, as well cells in general, typically grow and proliferate best in highly aqueous hydrogels, mainly for the microenvironment that they offer. Typically, hydrogels

are divided into those made of natural polymers, and those made of synthetic polymers like poly-caprolactone (PCL); even combination of them are accepted. A major drawback of synthetic polymers, despite their strength and printability, is their limited bioactivity: they fail in mimicking extracellular matrix (ECM) leading to pour affinity for cellular adhesion, growth, migration and differentiation. Moreover, biodegradable materials show risk of toxicity and immunogenicity, while the non-degradable ones are generally discarded due to the risk of extrusion and impedance of de-novo tissue formation [3]. As such, there has been a progressive shift in the use and refinement of natural materials. The ideal material should have good mechanical properties to allow bioprinter deposition and acceptable stiffness to support potential stresses *in vivo* and above all, support cellular attachment, function and proliferation [5]. Furthermore, in 3D bioprinting field is challenging to mimic the heterogenous tissues that most organs and tissues are formed. In the present case of auricle, it is challenging to fabricate heterogeneous cell-laden scaffolds for the reconstruction of the fatty, cartilaginous and skin parts. Another critical challenge lies in the high cost and limited accessibility of bioinks. Obtaining materials requires purchasing them from the same companies that supply bioprinters and the high prices of these materials represent another obstacle particularly in the research field where budgets can be tight. Efforts to simplify the manufacturing process, reduce costs, and establish more accessible bioink resources are critical to unlocking the potential of this technology. Thus, overcoming these challenges will not only improve the viability of 3D bioprinting, but also increase its impact in various fields, from research to regenerative medicine and more.

Among the natural polymers alginate is a widely used polysaccharide in tissue regenerative fields because of its high-water content, resembling the ECM, biocompatibility and non-toxicologic properties. However, the rheological properties of pure alginate formulations result in poor printability and patter fidelity [6]. Previous studies have found the efficacy of nanoparticles, such as nanocellulose (NC), to improve the mechanical properties and maintain the structure of printed scaffolds. NC is also characterized by high water content, adequate biocompatibility and exceptional physical and chemical properties [3]. In this thesis cost-effective biomaterials are used: Sodium-Alginate is blended with Crystalline Nanocellulose (CNC) and the obtained composite printed via pneumatic extrusion-based technique. While as cells human dermal fibroblasts are used. The primary goal is to identify the right concentrations of the two biomaterials that supply to the bioink the optimal printability, stability and shape fidelity post-printing, necessary to print a complex structure like the external ear. Furthermore, several strategies are tested to reduce the intended original shape loss during crosslinking. Secondary, the bioink must have a controlled degradation behaviour in a physiological environment while promoting cell viability and proliferation.

1. EAR ANATOMY

Despite the evolution of the current reconstructive options, the complexity of the auricular anatomy makes it challenging to achieve a satisfactory aesthetic external ear. Surely, the advent of tissue engineering and 3D bioprinting have furthered efforts toward fabricating cartilaginous frameworks satisfying patients' needs. However, several obstacles remain, including the need for high cell proliferation, resistance to deformation forces and sustainable framework longevity. Thus, before presenting a potential novel solution to auricular framework, "bioink", the biochemical and biomechanical properties of human auricular cartilage need to be detailed described.

Firstly, the ear can be divided into the external, middle and inner ear. The external ear (auricle or pinna) is a single piece of elastic cartilage, organised in two layers of perichondrium and covered by hairless skin. It has a complex architecture made up of different components: Helix (HE), Lobule (LO), Antihelix (AH), Antitragus (AT), Concha (CO), Scapha or scaphoid fossa (SC) and Triangular fossa (TF), shown in Fig. 1. The LO is the only part that is devoid of cartilage and is made up of connective tissue. Embryologically, the external ear starts to form at 6 weeks' gestation and is completed by 18 weeks. This complex process involves six mounds of tissue, called the hillocks of His. The first three hillocks arise from the first pharyngeal arch to form the Tragus (TR), Helical root (HR) and HE; the next three arise from the second pharyngeal arch to form AH, CO and AT. The cartilage is then covered by ectodermal-derived epithelium to form a recognizable ear structure as early as the 18th gestational week. The AH, HE, and SC are the least rigid, most variable, and highly significant in terms of aesthetics; in conjunction with TF and AT, they are formed from the rear free fold which makes them most susceptible to deformational forces in utero and/or ex utero. When examining a patient with possible microtia, it is important to evaluate which components are missing, in addition, it should be known that the process of the auricular cartilage folding varies among individuals [7].

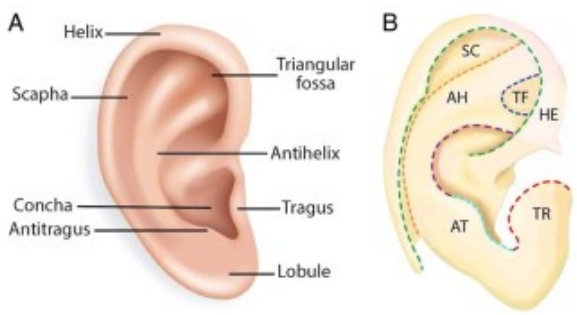

Fig. 1. Ear anatomy. (A) Anterior surface of the auricle. (B) Anterior surface of the auricular cartilage. AH stands for antihelix; AT, antitragus; HE, helix; SC, scapha; TF, triangular fossa, TR; tragus [7].

1.1. Cartilage

Cartilage is a connective tissue relatively rigid with a flexible ECM similar to rubber. ECM is a dynamic well-organized 3D network of macromolecules, as can be seen in Fig. 2, that provides structural support for the cells and tissues; it plays also regulatory roles since it organizes and supervises cell signalling, functions, properties and morphology. Particularly, certain matrix components affect cell processes and functions, such as cell proliferation and survival, migration, differentiation, autophagy, angiogenesis and immunity regulation. The building blocks of this multiplicate architectural network are the collagens, proteoglycans (PGs) and glycosaminoglycans (GAGs), elastin and elastic fibres, laminins, fibronectin and other proteins/glycoproteins such as matricellular proteins. PGs consist of a protein core decorated with negatively GAGs. They hold both structural and biological roles, as being responsible for the mechanical resistance to compression and hydration of the tissues; they also serve to trap grow-factors (GFs) in the ECM. The distribution, concentration, and ratio of the various ECM molecules determine the unique biomechanophysical properties of distinct tissues [8].

Among several functions, the cartilage gives shape to nose and ear, supporting them; it covers partially the larynx, the trachea and the thoracic cavity. Cartilage is produced by stem cells called chondroblasts that produce the matrix which surrounds them until being entrapped in small cavities named as lacunae. In the lacunae the cells are called chondrocytes. The cartilage rarely contains blood vessels and when it happens, they pass through it without forming capillaries for tissue nutrition. Thus, nutrition and scores disposal exclusively depend on the diffusion of solutes through the rigid matrix. Since this process is slow, the metabolic activities and the cellular divisions are slow too and the damaged cartilage recovers much slowly. The matrix is rich in GAGs and

fibres of collagen, mainly of type II, that range from being too small nearly invisible to very gross. Differences among fibres allow to classify the cartilage in three types: hyaline cartilage, elastic cartilage and fibrous cartilage, shown in Fig. 3. The hyaline cartilage is characterized by a light and vitreous matrix and fibres of collagen not visible, and chondrocytes arrange in small groups; it forms the articular cartilage and costal one. The elastic cartilage has the fibres that form an articulated mesh among the lacunae; its characteristic locations are the external ear and epiglottis. The fibrous cartilage instead is characterized by fibres of collagen parallel to each other and it is mainly present in the intervertebral disks [9].

Auricular cartilage

The auricular cartilage is an elastic cartilage whose mature chondrocytes become spheroids through the ECM, where elastic fibres form a reticular mesh. Its main function is to provide elastic and flexible support. The matrix is composed chiefly of water, PGs, lipids and collagens. PGs are a series of mucoprotein copolymers, conjoined in large lateral chains without rami, of condroitin-4-sulfate glycosaminoglycans (sGAGs), condroitin-6-sulfate and keratin sulphate. The proportions are modified with age: keratan sulphate increases with age. The resistance to compression and the viscoelasticity are referred to PGs' content of GAGs, while the resistance to tension to the collagen and elastic fibres content [10].

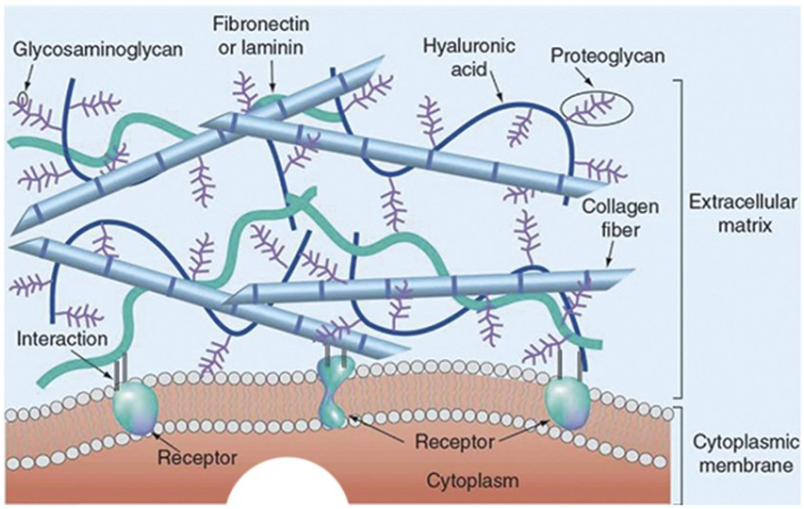

Fig. 2. The 3D structure model of the natural ECM [11].

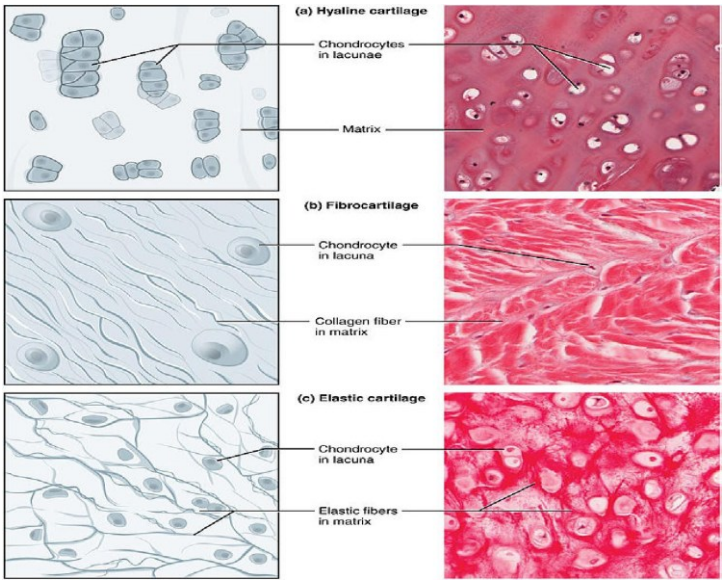

Fig. 3. Differences between a) Hyaline cartilage, b) Fibrous cartilage and c) Elastic cartilage.

1.1.1. Microstructure and Tissue organisation

As introduced in the previous sub-paragraph, the principal cells of cartilage, especially of auricular cartilage, are chondrocytes residing within lacunae surrounded by an abundant, compact ECM composed of elastin, collagen and sGAGs. Elastin is present in all cartilage components of the auricle, both intracellularly and extracellularly and appears as thin fibres in the ECM forming a dense lattice network around the individual chondrocytes. Griffin et al. have found that auricle is homogeneous in chondrocyte morphology, ECM and elastin content; they observed chondrocytes with similar morphologies across all anatomic regions of auricular cartilage. However, Melgarejo-Ramírez noticed a change in the shape of chondrocytes as they approach the perichondrium. In addition, the matrix is also more compact near to the perichondrium. In contrast to Griffin, Kana and colleagues noted that the external surface of SC is less cellular, with oval-shaped chondrocytes and a higher density of elastic fibres. Differently, the external surface of HE and AH is characterized by an increased number of chondrocytes that are more elongated and fusiform in shape and surrounded by a lower concentration of elastic fibres. Overall, the auricular cartilage shows a tri-lamellar structure with a greater concentration of elastic fibres in the central one than both the external zones. Furthermore, light microscopy analysis revealed differences in the number of chondrocytes among different age groups: cartilage from young individuals has increased quantity of chondrocytes than older ones. However, aged human cartilage has better mechanical properties than young one, due to aged-related variations in the ECM components. Regarding the thickness, it has

been found that is not uniform among the several auricular parts and higher for the older adults than young ones. Researchers have also studied tissue architecture under pathological conditions, such as microtia, and, through histologic analyses, they have found that the internal tissue organization is similar to that of healthy cartilage.

1.1.2. Mechanical properties

Auricular cartilage has viscoelastic properties; its structural composition, composed primarily of collagen and elastin fibres that encompass a proteoglycan gel, allows the cartilage to retain water which translates into an elastic response to load. Elastin is the major contributor to the intrinsic mechanical properties of the auricular cartilage. It promotes stiffness at equilibrium and allows the ear to be flexible, maintaining its shape against the micromechanical forces exerted during an individual's lifetime and post-surgery. To study the micro-deformation characteristics of the human auricular cartilage, its mechanical properties are in general characterized through tensile and compressive testing. Auricular cartilage has homogeneous compressive properties: an average compressive modulus of around 1±2 MPa. Instead, its stiffness is quantified by the Young's modulus in tension of around 5 MPa.

2. THREE-DIMENSIONAL BIOPRINTING

3D bioprinting can be defined as a computer-aided layer by layer additive bio-fabrication of cell-laden constructs and/or scaffolds for various tissue types. This technology includes both hardware (3D bioprinter) and software (digital model): 3D bioprinter is a robotic dispensing device which precisely places biomaterials alone or with living cells in 3D space according to a digital model. Since it refers to 3D cell assembling with printing, it can simply be named as cell, tissue or organ printing [12, 13]. Not only living cells are deposited, but also other substrates such as nucleic acids, drug particles, proteins, ECM components, GFs and other biological components in a layer-by-layer fashion [14].

There is a huge gap in organ transplantation, indeed, the success rate of matching is low all over the world due to insufficient organ donations; a great number of patients die while waiting for a suitable organ transplantation. Another aspect that cannot be ignored is the high cost. Furthermore, there are risks of morbidity at donor site, and allogenic transplant causing immune rejections are huge hurdles for the recipients. So, manufacturing of tissues or organs *in vitro* has become a primary goal for humans. At present, there is search for more precise and complex models *in vitro* to resemble the complexity of human tissues and organs, as well as their *in vivo* conditions. 3D bioprinting represents an optimal solution rather than the traditional ones based on two-dimensional (2D) cell culture and animal experiments. Indeed, 2D culture is different from the 3D environment *in vivo* and great differences of the internal environment cannot be ignored between animals and humans. Furthermore, many ethical problems exist in animal experiments. Nevertheless, there are still a lot of complications: many intrinsic mechanisms of development need to be further understood in biology and reengineering the structure of the objective organ is also a huge challenge [15]. 3D bioprinting represents a tremendous advancement of conventional TE too: it allows to deposit biomaterials and cells simultaneously to the designed locations, while the second seeds the cells on the constructed scaffolds. Above all, it is hard to deposit different kinds and various densities of cells at the desired positions of the scaffolds, therefore, it is difficult to mimic the structures of the soft tissues and organs. Additionally, TE methods allow to control only bulk properties, but the pore size, shape, network, internal architecture and topology cannot be determined. Moreover, requirements of porosity and precision cannot be achieved easily through TE approaches [14].

3D bioprinting is characterized by three tasks: preparing bioinks, printing the soft live structures with multiple cells by selected bioprinters and rebuilding the interaction among cells. There are different bioprinting approaches according to various printing principles: extrusion-based,

droplet-based and photocuring-based bioprintings, with their own different characteristics and specific requirements for bioinks. Droplet-based bioprinting employs discrete droplets to stack into 3D models and it can be roughly divided into inject bioprinting, electrohydrodynamic jetting (EHDJ) and laser-assisted bioprinting (LAB). Instead, photocuring-based bioprinting solidifies photosensitive polymers to form constructs under precisely controlled light-ing with high printing precision and fast printing speed. It can be further classified in stereolithography (SLA), projection-based printing or digital light processing (DLP) [16].

2.1. Extrusion-based bioprinting

Extrusion-based bioprinting is the most widely used bioprinting method at present; a series of extrusion 3D bioprinting technologies have been commercialized, making it more popular. Extrusion 3D bioprinting can print human-scale tissue, which is difficult to achieve by other bioprinting methods [17]. A typical extrusion-based bioprinter combines a dispensing head and an automated three-axis robotic system. It allows to extrude cell-laden bioinks through a nozzle orifice, using pneumatic pressure or mechanical force by means of a piston or screw, in manner of continuous filaments repeated layer-by-layer on a receiving substrate until a 3D structure is obtained. Since the filaments are generated by the continuously applied force, extrusion bioprinting system can be applied to bioinks with various viscosities, especially the most highly viscous. Materials with higher viscosities offer more support for maintaining bioprinted structures, while lower viscosities material provide better micro-environment for cell viability and functionalization. It has been found that materials with viscosities ranging from 30 to 6 x 10^7 mPa/s are compatible with extrusion-based bioprinters. Furthermore, materials with temperature-sensitive or shear-thinning properties which meet the printability requirements are often chosen. The presence of multiple printer heads allows to use different kinds of biomaterial at the same time; the extrusion speed, procedure and deposit location can be flexibly adjusted by the computer aided operator. Besides, a typical extrusion bioprinter is able to control the shapes, pores, porosity and cell distribution of the printed scaffolds. Nevertheless, its resolution is usually about 200 microns, which not only makes it difficult to accurately simulate tissue structures but also limits its wide application. Additionally, when printing cell-laden materials, the rapid printing speed and/or the high viscosity of the bioink can provide high shear stress in the nozzle and finally result in decrease of cell

viability. Thus, in order to print cells, the nozzle diameter is limited to the cells size, conversely limiting the printing resolution.

Extrusion-based bioprinting is based on different dispensing approaches: pneumatic-driven, piston-driven or screw-driven extrusion systems and solenoid micro-extrusion-based bioprinting, illustrated in Fig. 4. They rely on the same working principle: bioinks are loaded into a syringe barrel and are extruded through a micro-nozzle tip. The last mechanism exploits electrical pulses to open a valve at the base of the syringe; this type of extrusion allows for dispensing of sub microliter range volume of materials [14,16].

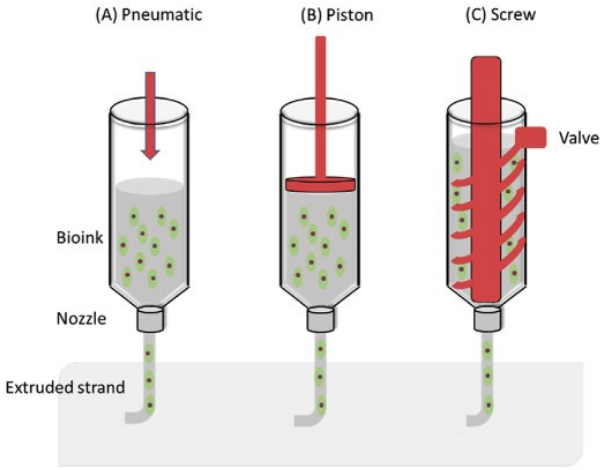

Fig. 4. Schematic diagram of extrusion-based bioprinting pneumatic and mechanical methods: (A) Pneumatic via pressurized air, (B) Piston-driven mechanical extrusion and (C) Screw-driven mechanical extrusion [18].

2.1.1. Pneumatic extrusion-based bioprinting

Pneumatic-based systems are extensively used due to their simplicity and high viability in material deposition; compared to other bioprinting techniques, they operate better for highly viscous materials. These systems utilize pressurized air using valve-free or valve-dependent configurations. The first ones are simple, but they provide less control over the materials having low viscosity since they leak out of the nozzles; the second, instead, allow users to control both pressure and pulse frequency resulting in more precise procedure and result. During the printing process the bioink is pressurized to move from the syringe to and though the nozzle with a specific diameter and geometry. It is suggested to use hydrogels with shear thinning properties to preserve filament shape upon exposure to the shear stress generated during the printing process. Shear stress affects also cell and their viability: the effect of fluid flow on cells can be neglected in the syringe but in the nozzle, where the maximum velocity

gradient as well as the maximum shear stress are experienced, leading to cell deformation. Theoretically, as the shear stress increases cell damage increases in an exponential form. However, distinct cell types may differ in their sensitivity and response towards shear stress, and consequently cell viability values differ as well [18].

2.2. Bioprinting process

A typical bioprinting process, depicted in Fig. 5, is characterized by three phases: pre-processing, processing and post-processing phase. The pre-processing involves digital design obtained from medical images, and selection of suitable materials. Then, the designed images are sent to the bioprinting system and the bioinks are loaded for processing. Finally, the printed constructs are transferred into bioreactor for tissue maturation during the post-processing phase.

2.2.1. Pre-processing

Before starting the bio-fabrication process, it is necessary to have a blueprint in the form of computer-aided-design (CAD) of the designed tissue or organ and the detailed information of the printed structure, as well as cell locations in 3D should be determined. In case of a simple scaffold, the 3D model data include details such as surface geometry, porosity and material distribution. There are several approaches by which it is possible to get information about the anatomy, histological structure, composition and topology of human organs necessary for CAD process. Firstly, clinical bioimaging and ultrasound allow to discern the gross anatomical characteristics of organ even while they are still inside their owner. The main advantage of this approach is to get anatomical information without the need of removing the individual's organ in order to examine it. However, tissue composition and cell distribution cannot be precisely identified as yet. A second approach is based on computer-aided reconstruction of a histological section. This method provides a high level of resolution and information about the size and shape of the organ, as well as details about its composition. However, this inspection is possible only after death, so, organs are subjected to change and distortion. Moreover, this approach is labour-intensive, time consuming and is not patient specific. A third approach is based on a mathematical computational anatomical model: several pieces of software permit the creation of a realistic anatomical model from bioimages. The most frequently used techniques to obtain medical images are Magnetic Resonance Imaging (MRI) and

Computed Tomography (CT) scans. A Bio-CAD system can mimic the 3D anatomic structures, differentiate heterogeneous tissue types and create desired computational tissue models. Bio-CAD can be combined with Bio-Computer aided manufacturing (CAM) that allows to simulate the designed models to predict the fabrication process feasibility. Furthermore, this technique enhances the understanding of the physical and chemical mechanisms during printing [13,14]. In addition, in the pre-processing stage, suitable cell type and biomaterials that meet application requirements are chosen. Biomaterials should provide mechanical support as well as the idoneous microenvironment for cells viability. Factors such as biodegradation rate, biocompatibility, viscosity, printability and crosslinking should be taken in account to ensure high cell viability and high resolution [18].

2.2.2. Processing

During the processing stage a suitable bioprinter is used to print the desired 3D structures using appropriate bioinks. The bioink, composed of cells and biomaterial, is loaded into the printing system chosen and deposited to build a 3D construct. The printing capacity is determined by various physical and chemical properties of bioinks. During the processing stage cells are subjected to mechanical forces of different types that play a major role in controlling cell growth, differentiation and motility. During extrusion-based bioprinting mainly, shear stress is of special significance as mechanical force, and it is considered the main cause for cell damage/death. Nevertheless, it can be modelled mathematically and computationally in order to optimize the printing process, and therefore, maximize the number of living cells post printing [14,18].

2.2.3. Post-processing

In the post-processing phase, bioink is crosslinked either by physical or chemical strategies such as ionic solution or UV light; this step is critical to provide stability and adequate mechanical integrity to the construct. Afterwards, the construct is placed either in an incubator or a bioreactor to mimic the in vivo environment for different tissues guaranteeing the survival, the maturation and other biological functions. Finally, the tissue becomes ready to be used *in vitro* for several tests and then to be implanted into the host.

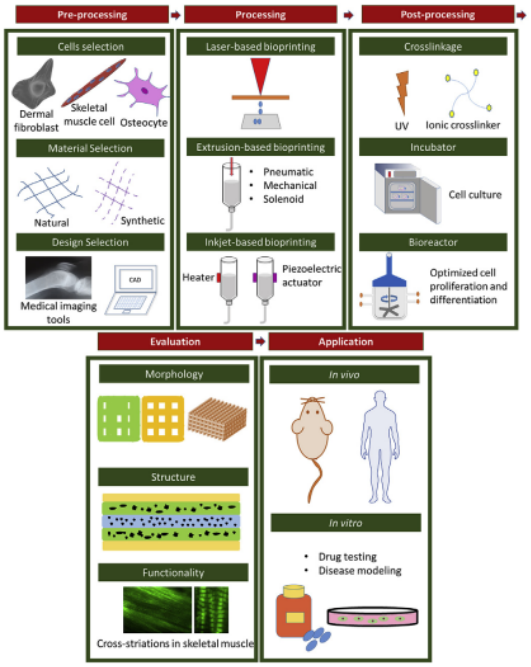

Fig. 5. Illustration of a typical bioprinting process: pre-processing, processing, postprocessing, evaluation and application [18].

3. BIOINK

Bioink is a material composed of living cells suspended in a polymer, serving as a supportive scaffold, with good printability for 3D cell assembling; it may be characterized by the presence of other additives such as small molecules and GFs. After being solidified, it looks like jelly, more or less stiff according to the material used, and it has two functions: 1) acting as a glue to adhere cells for assembling 3D live structures and 2) providing a similar environment as *in vivo*. When bioprinting a scaffold and cells simultaneously, the most challenging aspect is the bioinks properties. The challenge lies in meeting both the biological requirements and those for good printability [18,19]. Thus, the bioink must be biocompatible and be noncytotoxic, supporting cellular attachment, viability, proliferation and function. Furthermore, for extrusion bioprinting, bioink must have suitable rheological properties and crosslinking mechanisms to enable accurate and precise deposition. So, the material should exhibit gel-like characteristics or be sufficiently viscous to be dispensed as a free-standing filament; however, if the gel is too strong, large shear forces are required to extrude the ink likely resulting in cell death and gel fracture. Additionally, the material should have sufficient strength and stiffness to maintain structural integrity after printing [20]. Once the bioink has been implanted should degrade in a suitable time according to the type of tissue that must be replaced. Some biomaterials are unsuitable for bioprinting since they cannot be printed or the printing process will cause cells damage, others can be seeded with cells after printing but not directly formulated with cells. Generally, bioink-materials are usually composed of three types of materials: hydrogels, decellularized extracellular matrix, and microcarriers [17].

3.1. Biomaterials

Hydrogels have been widely used in extrusion-based bioprinting, alone or in combination; they are a type of soft material composed of crosslinked hydrophilic polymers forming a 3D network structure. One of the key properties of hydrogels as bioinks is the ability to complete the transition between liquid and solid state under certain conditions to realize the printing process [17]. Hydrogels have attracted most attention as promising matrices for bioinks because of their excellent properties: biocompatibility, low cytotoxicity and high-water content, mimicking natural ECM [21,22]. Indeed, the highly hydrated network permits the exchange of gases and nutrients and ensures cells do not dry out during printing. Furthermore, hydrogels interact well with cells and provide ideal conditions for adhesion, migration and proliferation and differentiation, as well as innervation and vascularization, but their

low stiffness and strength can be a limitation [23]. Hydrogels can be divided into synthetic hydrogels and natural ones according to their sources. Synthetic hydrogels are frequently used in bioengineering due to their superior mechanical and printability characteristics, with the additional advantage of being easily modifiable regarding their strength and rheological properties, and their ability to be programmed and reproduced; but lack of degradability and bioactivity represent their major drawbacks. A failure to mimic ECM results in a poor affinity for cellular adhesion, growth, migration and differentiation. Of the biodegradable synthetic materials, the degradation process may result in the release of by-products presenting a risk of toxicity or immunogenicity when implanted into humans. Whereas the nondegradable synthetic materials, despite offering superior shape preservation, risk extrusion and impedance of de-novo tissue formation. Nevertheless, polyethylene glycol (PEG), poly (vinyl alcohol) (PVA) and poly hydroxyethyl methacrylate (pHEMA) are examples of popular synthetic hydrogels due to their biocompatibility and high water-retaining capacity. In addition, PCL, PEG copolymers and poly(lactic-co-glycol acid) (PLGA), biodegradable synthetic materials, have attracted a lot of attention due to their capacity of breaking down over time and be replaced by natural tissue [3,23]. Compared with synthetic hydrogels, natural hydrogels, composed of natural substances such as sugars, proteins and nucleic acids, have received much attention due to their rich sources, low price and properties: outstanding biocompatibility, biodegradability and non-immunogenicity. Among them, natural polysaccharide polymers such as alginate, cellulose, chitosan, agarose and hyaluronic acid (HA), as well as proteins such as fibrin, collagen and gelatine, are important part of living organism structures and participate in many physiological activities. They possess bioactive components that enhance cell identification, adhesion, multiplication and biological maintenance. In addition, because of their aqueous environment with biologically relevant chemical and physical signals, they mimic the characteristics of ECM [21,24]. However, natural hydrogels have restricted mechanical behaviour and their application as bioinks in biofabrication of constructs with relevant dimensions and complex shapes can be challenging due to their suboptimal printability, tendency to degrade rapidly and unpredictably under biological circumstances. Their gel precursor solutions have low viscosity and Newtonian flow behaviour at low shear rates, thus prohibiting shape retention of the constructs after printing process. These limitations can be overcomed by increasing the molecular weight or adding viscosity

modifier macromolecules, even nanoparticles, to the gel solutions before printing and/or through crosslinking strategies [23,25].

3.2. Cells

According to the definition of bioink, both biomaterials and cells are important: printing cells with appropriate materials in a defined and organized manner is essential to produce constructs as biological substitutes promoting tissue regeneration and functional restoration. Biomaterial is significant as a carrier to support cells to form a stable spatial distribution, to maintain their activity in the printing process, to make them proliferate and differentiate after printing. At the same time, only when there are enough living cells in the bioink, the printed device can have cells arranged in a specific space, and only after the later period of culture the organs with complete functions can be formed. Therefore, cells are indispensable in the bioink [17]. The bioink used for extrusion printing can be loaded with various types of cells such as dispersed cells and aggregated cells: cell spheroids, cell pellet and tissue strands. The existence of different loaded cells is mainly due to the fact that the diameter of the injection port can vary over a wide range, usually between 50 μm and 100 μm.

Dispersed cells combined with biomaterials to form bioinks are widely used to build 3D tissue structures. Nevertheless, there is a little or no communication between the dispersed cells, that will lead to loss of cell functions, and poor anti-inflammatory ability, immunity resistance *in vivo* and low tissue regeneration, limiting their application in clinical medicine and other biomedical fields.

Instead, aggregated cells have a similar microenvironment to the tissue or organ *in vivo* and possess many advantages including anti-inflammatory ability, enhanced effect of tissue regeneration and immunity, as well high survival rate. Thus, cell aggregation is ideal for constructing tissues and organs. For example, cell spheroids can be loaded in the bioink: they are spherical aggregates of cells ranging from 200 to 400 μm in diameter. Several techniques exist for fabrication of tissue spheroids such as drop method, microfluidic-assisted technology, acoustic wave-assisted cell assembly etc. One of the most popular methods consists in culturing cells for 24-48 hours in microwells in rounded-ends on a cell-adhesin inert mold made of hydrogels; cells fall to the bottom of the microwells and settle in close contact with each other, promoting spontaneous aggregation. Whereas there are some technical problems during the printing process. First of all, a large number of uniform cell spheroids needs

to be obtained; secondly, it is difficult to collect and load cell spheroids into the sterilized syringe for extrusion, and cell spheroids have the ability of fast fusion which may lead to their aggregation at the exit of extrusion, inhibiting the printing process. The cell pellet technique is another method to create aggregates without the need of sophisticated systems; it is based on centrifugal or gravitational forces that concentrate cells at the bottom of conical tube. Then, the pellet is transferred for example in a mold to intercellular cohesion. Cells at very high density are injected into hollow alginate tubes that allow exchange of medium with nutrition and oxygen; cells grow in a given shape as they do not attach to alginate surface. When cells aggregate into a neo-tissue, the tube is dissolved using a decrosslinker solution and the formed tissue placed into a bioprinter head and extruded mechanically [17,26]. Almost all types of mammalian cells, such as cardiac cells, osteoblasts, pluripotent cells, endothelial cells etc., have been successfully bioprinted to engineer various tissue types. While not all the materials satisfy the requirements required to be combined with cells forming bioinks; natural polymer hydrogels are optimal choice [14]. Hydrogels have gained so much attention even for being softer than the other materials, thus, enhancing the interaction with cells: their modulus is generally less than 1 kPa, and the enhanced hardness hydrogels modulus is up to 1 MPa. Meanwhile, cells loaded into the biomaterial affect the material itself; high cell density could accelerate tissue formation after printing, but the presence of cells also significantly affects the printability and the mechanical strength of bioinks. Furthermore, long term proliferation and migration of cells in bioinks will change the performance of bioinks, such as cell traction and matrix remodelling by enzyme degradation [17].

4. ANALYSIS TECNIQUES

Bioinks should meet the requirements of mechanical properties in the process of 3D bioprinting and the requirements of proliferation and differentiation of cells in the structure after printing. In this chapter tests that are usually performed on the printed scaffold, without cells, and on the bioprinted scaffold, with cells, are listed and explained.

4.1. Rheometer and Rheological properties

Bioink behaviour can also be assessed practically by examining its rheological characteristics, such as viscosity. This analysis is important since high viscosity can keep the shape of the extruded bioinks, improve the mechanical stability and facilitate the printing of multi-layer structure. Meanwhile, high viscosity will cause blockage of the nozzle and lead to discontinuous and uneven accumulation of bioink. Moreover, high viscosity represents the effect of increased extrusion force on cell structure damage. Conversely, low viscosity results in uneven cell dispersion and cell deposition in the bioink. Thus, as already highlighted, materials with shear-thinning rheological properties have been widely used in bioinks [17].

Rheology is a branch of physics that allows to describe the deformation and flow behaviour of all kinds of material. Rheometry is the measuring technology used to determine the rheological properties. Rheometer, differently from other instruments such as a viscometer that is able to determine only the viscosity values of the sample, is able to analyse many more **rheological parameters**. Viscosity is the internal friction that occurs when all components, in a flowing liquid, are forced to slide along each other; because of this internal friction they develop a flow resistance. Generally, for the determination of viscosity rotational tests are performed: rheometers operate both with continuous rotation and rotational oscillation, as can be observed in Fig. 6 [27].

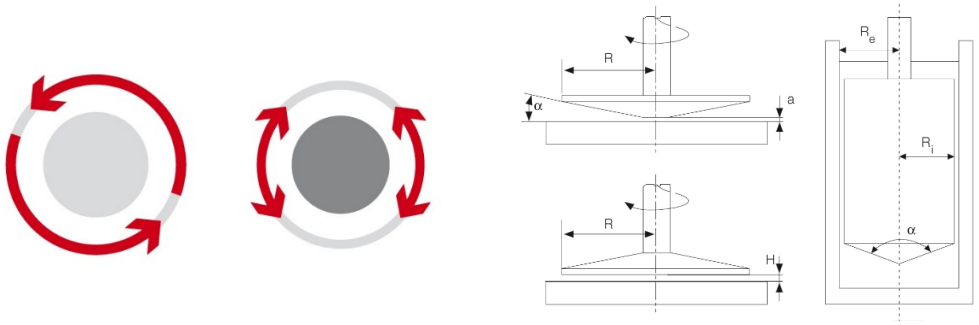

Fig. 6. The image on the left shows the measuring principle of a typical rheometer for rotational tests with continuous rotation (left) or rotational oscillation (right). The image on the right instead shows the measuring system: cone-plate (with radius R, cone angle α, truncation a); plate-plate (with radius R, distance between plates H); and concentric cylinders (with bob radius R_i and cup radius R_e and internal angle α at the tip of the bob).

Rotational tests and viscosity

Rotational test on a sample consists in the upper plate that rotates while the lower plate is stationary. Two operation modes exist, the first is to present the velocity via rotational speed, n, or controlled shear rate, γ, the second to present the driving force via torque, M, or shear stress τ. They simply differ in the preset parameters. Nevertheless, for calculating the viscosity, the type of operation mode is irrelevant because the parameters shear stress and shear rate are both available, either as a preset value or as result of the test [28].

The two-plates model is used to define the rheological parameters needed for the description of the *flow behaviour*: the lower stationary plate is mounted on a very rigid support, and the upper plate can be moved parallel to the lower plate, the sample is sandwiched between the two plates.

Before calculating the viscosity, it is necessary to define the shear stress and the shear rate. Shear is applied to the sample.

Shear stress is given by eq. (1) with shear stress τ, shear force F (in N) and shear area A (in m^2). The unit for shear stress is 1 N/m^2 = 1 Pa. The rheometer records the shear force via the torque at each measuring point.

$$\tau = \frac{F}{A} \tag{1}$$

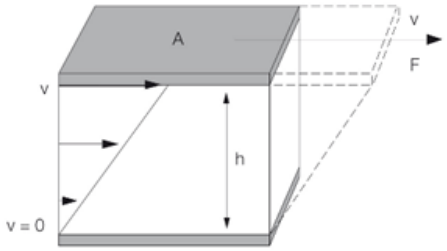

Fig. 7. Two-plates model for the calculation of shear stress and shear rate.

Shear rate is given by eq. (2) with shear rate $\dot{\gamma}$, the velocity v (in m/s) and shear gap h (in m). The unit for shear rate is 1/s = 1 s^{-1}. A rheometer records the velocity as the rotational speed at each measuring point.

$$\dot{\gamma} = \frac{v}{h} \tag{2}$$

Viscosity η is defined as shear stress τ dived by shear rate $\dot{\gamma}$, eq. (3)

$$\eta = \frac{\tau}{\dot{\gamma}} \tag{3}$$

Viscosity values are not constant as they are affected be many conditions.

Ideally *viscous flow behaviour* (or Newtonian flow behaviour), depicted in Fig. 8, means that the measured viscosity is independent of the shear rate. Typical materials of this group are water, mineral oil etc.

Shear thinning behaviour (or: pseudoplastic flow behaviour), depicted in Fig. 8, is characterized by decreasing viscosity with increasing shear rates. Typical materials that show this behaviour are coatings, polymer solutions and polymer melts. This behaviour is related to the internal structures of the samples.

Shear thickening behaviour (or: dilatant flow behaviour), depicted in Fig. 8, means increasing viscosity with increasing shear rates. Materials that typically display such behaviour include highly filled dispersions, such as ceramic suspensions (casting slurries), dental filling masses (dental composites) as well as special composite materials for protective clothing.

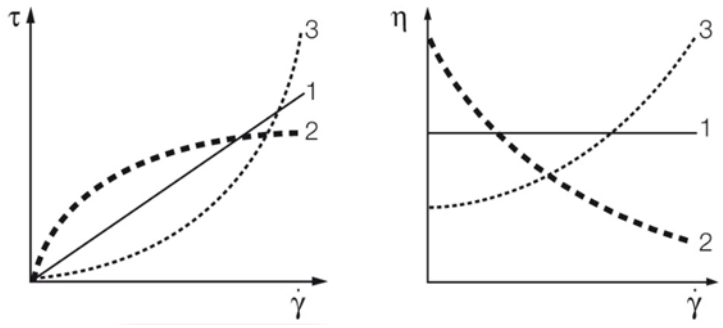

Fig. 8. Flow curves (left) and viscosity curves (right) for (1) ideally viscous, (2) shear-thinning, and (3) shear-thickening flow behaviour.

The **yield point** is the lowest shear-stress value above which a material will behave like a fluid, and below which the material will act like a – sometimes very soft – solid matter. Thus, the yield point or yield stress is the minimum force that must be exceeded in order to break down a sample's structure at rest, and thus make it flow. Too much of it can damage cells and 3D printing equipment.

For the characterization of the rheological properties of bioinks, time-dependent behaviour is investigated. A step test should be carried out, a rotational test with three intervals, where at each interval the shear is maintained constant. Below the three intervals:

- Interval (1): very low shear is applied to simulate behaviour at rest at a preset low shear rate. This stage represents the initial outflow stage when the bioink just starts to flow. At this moment the viscosity is the static one and the shear force is the yield stress.
- Interval (2): strong shear is applied to simulate structural breakdown of the sample during processing at a preset high shear rate. This stage is the shear-thinning stage after extrusion, thus the viscosity of the bioink decreases with the increase of shear rate, which is suitable for continuous extrusion, the formation of uniform filaments and enhancing/increasing the survival rate of cells during extrusion. However, there is a lower limit for viscosity reduction, below which the bioink becomes a droplet rather than a uniform filament when extruded.
- Interval (3): very low shear is applied to simulate structural regeneration at rest after application using the same preset low shear rate as in the first interval. This third stage is the post-print recovery stage, during which post-print curing

ability of bioink is characterized through the relationship between viscosity and time, which is related to the stability of size and the dispersity of cells. For example, slow viscosity recovery may result in the sedimentation of cells.

In contrasts, other materials show no structural regeneration, but gel formation or curing under constant shear conditions [28].

Oscillation tests and viscoelasticity

Those materials that show a mixture of viscous and elastic behaviour when sheared have a *viscoelastic behaviour*. Often the elastic portion of the viscoelastic behaviour is more pronounced under certain conditions, such as faster movements that means a higher rate of deformation and shear rate or a higher oscillation frequency and lower temperatures. In both cases, the molecular networks will be less flexible and stiffer. Instead, the slower the motion and/or the higher the temperature, the more flexible and mobile the behaviour of the molecules will be [27].

The two-plates model is also used for the definition of the rheological parameters needed for the description of *deformation behaviour*.

Shear strain (or shear deformation) is given by eq. (4) with shear strain γ, deflection path s (in m), and shear gap h (in m). The deformation is dimensionless.

$$\gamma = \frac{s}{h} \tag{4}$$

Shear modulus is given by eq. (5) with shear modulus G, shear stress τ (in Pa), and shear strain γ.

$$G = \frac{\tau}{\gamma} \tag{5}$$

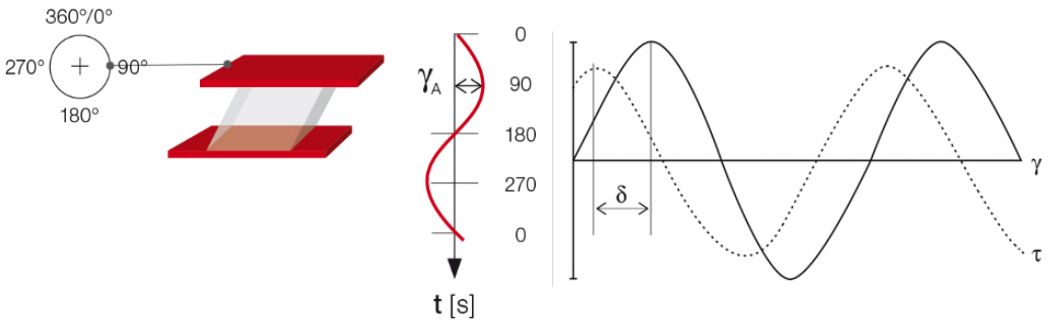

Fig. 9. On the left: oscillatory test using the two-plates model; on the right: time dependent strain value with the amplitude γ_A of the upper plate. On the right: oscillatory test for viscoelastic behaviour, presented as a sinusoidal function versus time, with preset shear strain γ and resulting shear stress τ. The two curves are offset by phase shift δ.

The two-plates model can also be used for explaining oscillatory tests, Fig. 9. A push rod mounted to a driving wheel moves the upper plate back and forth parallel to the lower plate, as long as the wheel is turning. At constant rotational speed, the model operates at a correspondingly constant oscillating frequency. The deflection path of the upper, movable plate is measured and rheologically evaluated as strain that is plotted versus time resulting in a sine curve with the maximum strain amplitude γ_A. In addition, the force that acts upon the lower, stationary plate, and required to keep it in position, is measured. The signal is rheologically evaluated as shear stress τ. If the sample is not strained by too large a deformation, the resulting diagram over time is a sinusoidal curve of the shear stress with the amplitude τ_A, otherwise the inner structure of the sample would be destroyed, and the resulting curve no longer be sinusoidal [28].

For a completely rigid sample, such as one made of steel or stone with ideally elastic behaviour, there is no time lag between the preset and the response sine curve. Most samples show viscoelastic behaviour, like biopolymers, and, in this case, the sine curves of the preset parameter and the measuring result show a time lag for the response signal. This lag is called the **phase shift** δ, highlighted in Fig. 9, where $0° > \delta < 90°$.

For the fluid state, $45° < \delta < 90°$. In this case, the material at rest is fluid. Moreover, $\delta = 0°$ for ideally elastic deformation behaviour and $\delta = 90°$ for ideally viscous flow behaviour. All kinds of viscoelastic behaviour take place between these two extremes.

For the solid, gel-like state, $0° < \delta < 45°$. In this case, the material at rest is solid, such as gels.

For oscillatory shear tests the law of elasticity, eq. (6), is used, with complex shear modulus G^*(in Pa), shear-stress amplitude τ_A (in Pa), and strain amplitude γ_A (dimensionless). The complex modulus describes the entire viscoelastic behaviour of the sample.

$$G^* = \frac{\tau_A}{\gamma_A} \tag{6}$$

In Fig. 10 the phase shift is now represented as an angle below the G^* vector. The part of the G^* value that runs along the x-axis is the elastic portion of the viscoelastic behaviour presented as G' while the part of the G^* vector that is projected onto the y-axis is the viscous portion G''.

The **storage modulus** G'(in Pa) represents the elastic portion of the viscoelastic behaviour, which quasi describes the solid-state behaviour of the sample. The **loss modulus** G'' (in Pa) characterizes the viscous portion of the viscoelastic behaviour, which can be seen as the liquid-state behaviour of the sample. The first one represents the stored deformation energy while the second the lost energy through internal friction when flowing. Viscoelastic solids have higher storage modulus than loss modulus ($G' > G''$), on the other hand, viscoelastic liquids have a higher loss modulus than storage one, ($G'' > G'$). This is due to inks inside the material: viscoelastic solids predominantly consist of chemically bonded molecules, or structures with other strong interaction forces. Whereas, liquids are typically composed of mainly unlinked individual molecules, which may show some entanglement as, for example, uncrosslinked polymers. With $G' > G''$ the printability of a bioink increases and it has been demonstrated that G' value between 154-382 Pa favours printing fidelity and cell viability [29].

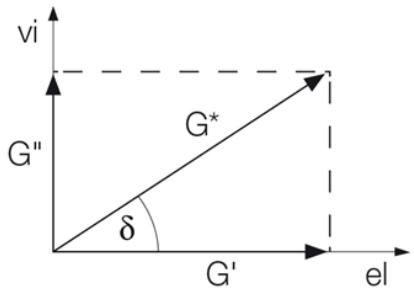

Fig. 10. The diagram illustrates the relationship between complex shear modulus G, storage modulus G' and loss modulus G'' using the phase-shift angle δ. The elastic portion of the viscoelastic behaviour is presented on the x-axis and the viscous portion on the y-axis.*

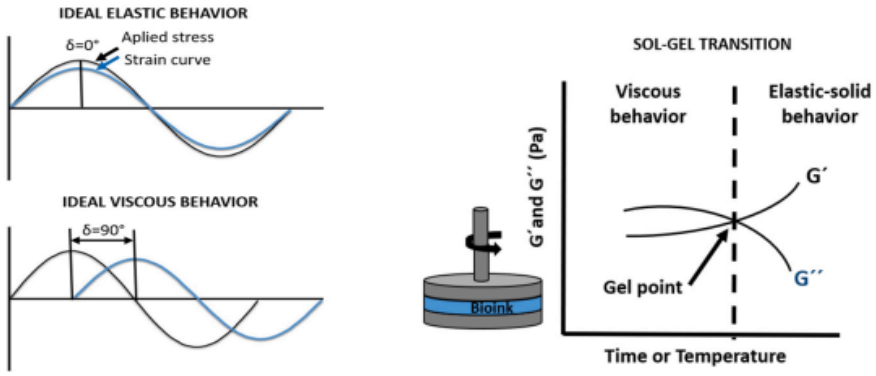

Fig. 11. In the image on the left the lag, δ angle, between the applied stress and the and oscillatory (sinusoidal) deformation, response, is shown. It reflects the predominance of the elastic (small values) or viscous (high values) behaviour of the sample. In the image on the right the intersection, between the G' and G'' curves, stands for the sol–gel transition. Thus, G" > G', viscous behaviour; G" = G', gel point; G' > G", elastic solid behaviour [29].

Another rheological parameter is the **loss factor**, or damping factor, that describes the ratio of the two portions of the viscoelastic behaviour, eq. (7), thus, it is dimensionless.

$$\tan \delta = \frac{G''}{G'} \tag{7}$$

As can be seen from Fig.11 (left):

- for ideally elastic behaviour $\delta = 0°$. There is no viscous portion. Therefore, $G'' = 0$ and with that $\tan \delta = 0$;
- for ideally viscous behaviour $\delta = 90°$. There is no elastic portion. Therefore, $G' = 0$ and thus the value of $\tan \delta$ approaches infinity.

$Tan\ \delta$ is often related to the printability of hydrogel-based bioink. Low values reflect predominantly gel-like behaviour, and high values are related to more fluid-like behaviour. In the first case the bioink may be printed under low pressure, but the printing is too weak to preserve the structure. Stiffer bioinks, second case, must be printed under greater pressure which could damage cell integrity; moreover, irregular printing lines could be produced. It has been found that $\tan \delta$ in the range between $0.25 - 0.45$ is appropriate for printing [29].

The loss factor $\tan \delta$, when is plotted in addition to the curves of $G' = 0$ and $G'' = 0$, as in Fig. 11 (right), is also called **sol/gel transition point** or simply the gel point. It means that the character of the sample has changed during the measurement from the liquid or sol state to the solid or gel state and vice versa. Sol/gel transition can be

triggered by changes in temperature, polymer concentration, pH and crosslinking inductors.

In a **temperature sweep**, the intersection of $G'$and G'' indicates the gelation temperature, or the point at which the bioink changes from a viscous fluid to an elastic solid. Knowledge of the gelation temperature could facilitate the selection of the appropriate printing temperature to ensure the gel-like behaviour of the ink. In addition, knowledge of the sol/gel transition point aids determination of the temperature at which the ink exhibits fluid behaviour, permitting homogenous blending of the cells into the formulation [29].

Amplitude sweeps generally aim at describing the deformation behaviour of samples in the non-destructive deformation range or linear viscoelastic region (LVR) and at determining the upper limit of this range (Fig. 12). Often, it is also interesting to characterize behaviour that occurs if this upper limit is exceeded with increasing deformation, when the inner structure gets softer, starts to flow, or breaks down in a brittle way.

The **yield point** τ_y, also called yield stress, is the value of the shear stress at the limit of LVR. The **flow point** τ_f, also called flow stress, is the value of the shear stress at the crossover point $G' = G''$. At higher shear the viscous portion dominates and the sample flows [30]. See Fig. 12.

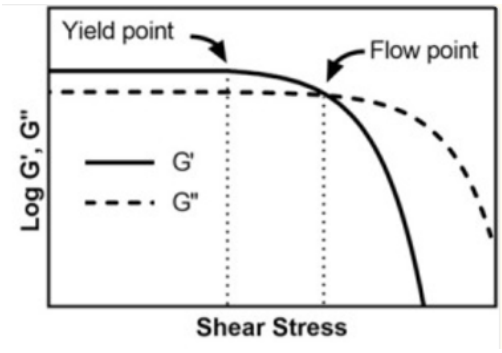

Fig. 12. Amplitude sweeps of a viscoelastic substance represented as a function of the shear stress, showing the yield point as the limit of the linear viscoelastic region and the flow point, e.g., the stress at which the viscous modulus G'' is above the elastic modulus G' and therefore flow can occur [30,31].

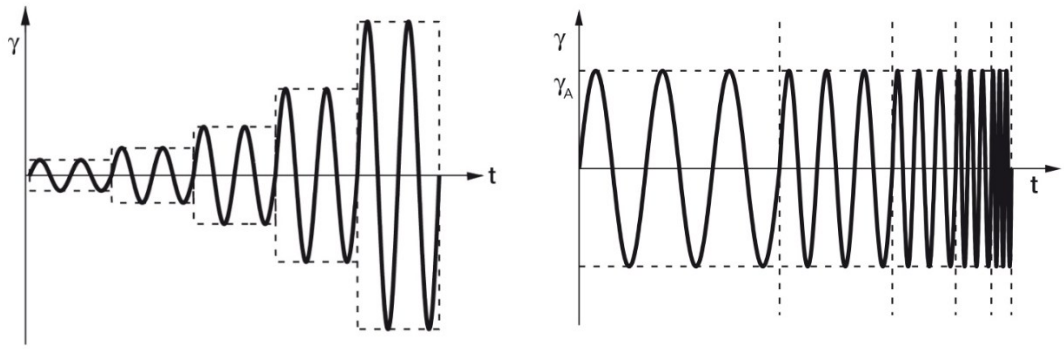

Fig. 13. Difference between a preset of an amplitude sweep and a preset of a frequency sweep: in the first case (left) the strain is controlled, and the amplitude is increased in five steps. Frequency is kept constant at all five measuring points. In the second case the shear strain is controlled, and the frequency is increased or decreased in five steps. The strain amplitude γ_A is kept constant over all five measuring points.

Frequency sweeps generally serve the purpose of describing the time-dependent behaviour of a sample in the non-destructive deformation range. High frequencies are used to simulate fast motion on short timescales, whereas low frequencies simulate slow motion on long timescales or at rest. In frequency sweeps the oscillation frequency is increased or decreased step-wise, Fig. 13 (right), from one measuring point to the next while keeping the amplitude constant.

Even for viscoelastic materials time-dependent behaviour, where amplitude and frequency kept constant at each interval, and temperature dependent behaviour, where only temperature changes, can be performed.

4.2. Scaffold characterization

Several tests must be done on the printed scaffold to assess if the blend chosen would be an optimal bioink; thus, resuming what has been already explained in the previous chapters, the ink should enhance cell viability and proliferation as well as be able to survive at physiological temperatures in an acceptable time allowing the formation of the neo-tissue. Moreover, the structure should emulate as much as possible the ECM, in terms of water content and substances uptake capability. Meanwhile, the scaffold must have similar mechanical properties of the native tissue, such that it is able to maintain its shape and to withstand stresses *in vivo* conditions. In this section some of the most used tests are shown, most of which have been selected to reach the goal of this thesis.

4.2.1. Swelling

Swelling can be defined as water uptake capacity of the printed scaffold. It is one of the essential characteristics of the scaffolds for tissue engineering applications. Indeed, it enables the structure to have a high uptake of nutrients and signalling molecules, enhancing cell viability and proliferation. Moreover, swelling of scaffolds in aqueous media is sometime desirable in biomedical applications since the pore size would increase initially, accommodating cells. At the same time, swelling is influenced by the internal porosity of the printed structure [32]. Although, swelling would lead to weaker mechanical properties: the material's stiffness would decrease, decreasing its capacity of withstanding external stresses, and also the shape of the construct could be altered. A denser network structure with a more compact porosity, as well as high viscosity, could decrease the swelling behaviour [33]. The test can be performed by monitoring the weight gain of the dried sample in culture medium at 37 °C, to simulate the physiological conditions, or simply in water at certain time points. Then, the swelling ratio can be computed through eq. (8):

$$SR\% = \frac{m_w - m_d}{m_d} \times 100 \tag{8}$$

where m_w is the weight of the wet sample at each time point while m_d the dried one [34].

4.2.2. Porosity and microporosity

A porous scaffold is desirable since it is characterized by an augmented surface available for cells adhesion and colonization; interconnected structure not only enables enough space for cell compatibility, growth and oxygen and nutrient diffusion, but also maintains the mechanical properties. Moreover, it facilitates the spreading of signal transduction and regulation. The average pore size depends on the tissue-type being substituted and, thus, on dimension of cells that must grow. There are several methods to evaluate the porosity as well as other morphological parameters such as surface area to volume ratio, pore size, interconnectivity, cross-section area and permeability. Porosity can be calculated by measuring the weight of absorbed ethanol according to eq. (9); where m_f is the sample saturated weight while m_i is the dried weight, ρ is the density of ethanol (0.789 g·mL^{-1}) and V the sample volume [34].

$$\varphi(\%) = \frac{m_f - m_i}{\rho \times V} \times 100$$

(9)

Optical microscopy or Scanning Electron Microscopy (SEM) can also be used to examine the surface, morphology and porous structure of the scaffolds. Microscopy is another technique that allows a direct and more precise measure of pores dimension and thickness.

4.2.3. Shrinkage

It is the comparison of the apparent volume of the sample before and after drying. It characterizes hydrogels and it leads to high dimensional changes due to a large amount of preserved water in their network. It influences the porosity; water uptake capacity and it is critical for cell survival. Generally, the higher the mechanical strength of the scaffold the lower the shrinkage [34].

4.2.4. Degradation and gel release

Degradation studies are essential in the evaluation of the behaviour of the scaffolds and their implications on cell studies, like differentiation and *in vivo* tissue formation. A desirable feature in regenerative medicine is the synchronization of scaffold degradation with the replacement by natural tissue produced from cells. Degradation rate too slow would impede the formation of neo tissue, making cell proliferation and protein release difficult to achieve. On the other hand, fast degradative scaffolds have been demonstrated to be inefficient in tissue regeneration. Degradation rate is related to material characteristics and crosslinking procedure; stable crosslink networks allow the material to exist for a longer time. Degradation test is performed by firstly measuring the scaffold area, then placing it in culture medium at 37 °C and, at selected time points, measuring again. The area loss can be calculated by using eq. (10) [33]:

$$Area\ loss\ (\%) = \frac{A_{before} - A_{after}}{A_{before}} \times 100$$

(10)

Degradation can be evaluated also in terms of gel release. Generally, the quantity lost is calculated 7 days after immersion using eq. (11):

$$GR\ (\%) = \frac{m_d - m_f}{m_d} \times 100$$

(11)

where m_d is the weight of the dried scaffold and m_f is the weight of the dried scaffold after 7 days of immersion [34].

4.2.5. Mechanical tests

In terms of macroscopic mechanical properties, the key indicators of a bioink are hardness, viscoelasticity, yield stress and strain. As supporting materials of cells, hydrogels should ensure that that these parameters support requirements after extrusion to avoid the occurrence of subsidence or deformation. Additionally, as goal of 3D bioprinting, the values of these indicators should be close to those of the organs in vivo [17].

Compression test is a kind of mechanical test that can be performed with load cell. The load to exert depends on the type of tissue that the bioprinted scaffold has to replace; generally, it is of the order of some N. Cylindrical or cubical structures are used as test samples; the load is applied on both surfaces of the scaffold and the change in length is recorded by software. The stress and the strain applied on the scaffold are calculated, by eq. (12) and eq. (13) respectively, to determine the mechanical strength of the scaffold.

$$\theta = \frac{F}{A}$$

(12)

$$\in = \frac{(L_1 - L_2)}{L_1}$$

(13)

F is the force applied and A the surface area that are calculated; $L_1$is the initial height and L_2 is the height after compression. [35].

The potential loss in compressive modulus over time of the scaffold stored in culture medium, respectively in incubation at 37 °C and in refrigeration at 3 °C, can be studied. The compression test is then performed at fixed days [20].

Not only the compressive strength of the printed, acellular, scaffold can be analysed, but also uniaxial tension test can be performed by using a tensile tester: the construct is stretched until sample failure. The modulus is then calculated from the initial linear regions of the stress-strain curves [22].

The mechanical properties of the bioink used for bioprinting should not only be considered for the construction of complex structures, but also for the interaction between cells and materials. Indeed, as already introduced in the previous chapters, cells are sensitive to the external mechanical environment and can change cell behaviour according to changes in the mechanical environment. In particular, the elastic modulus or hardness of the bioinks would affect the encapsulated cell behaviour. The mechanical properties of bioink should not only have the ability to support cells on the macro level, but also regulate the growth, proliferation and differentiation of cells on the micro level [17].

4.3. Biological analysis-imaging techniques

In general, the design of the bioink, the setting printing parameters and the post-printing treatments affect the cell activity, which will affect the subsequent cell behaviour, such as cell proliferation, differentiation and tissue formation. Indeed, cells must have sufficient survival rate to proliferate and differentiate into tissues; according to most studies, under optimal conditions, cell activity is usually between 70 and 90%, while under suboptimal conditions, cell activity becomes very low.

The extrusion printing process has a nonnegligible effect on cell activity. It includes the extrusion pressure, the injection speed, the extrusion outlet shape and the nozzle diameter. As mentioned above, bioinks with poor rheological properties need more extrusion force, which will cause damage to cells. Moreover, the components of the bioink, and the toxicity of crosslinking agent and crosslinking processes, such as photo-crosslinking, chemical crosslinking and thermal crosslinking, can damage cell structure and reduce cell activity [17]. Thus, once scaffolds have been characterized, cytotoxicity evaluation was needed prior to the introduction of cells into inks. Then, imaging analysis should be performed to control cell number, viability, growth, morphology and differentiation, as well as cell-cell and cell–matrix interactions.

To analyse any potential harmful effects of hydrogel-based inks on cell viability, the adhesion, direct contact and indirect contact cytotoxicity tests can be performed according to ISO 10993-5-2009 [33].

Since most cells are too small to see with the naked eye, the use of microscopes to produce biological images haven been promoted since the past. All microscopes have limitations on the size and detail with which they can be used to visualize objects. These limitations are linked to the particles used to create the images (i.e., photons or electrons); the wavelength at which these particles travel has a direct impact on the level of detail that can be reached in the image. Limitations of microscopes are considered in terms of magnification and resolution [36].

4.3.1. Optical microscopy

The most traditional tool to image cells and the first to be invented was the optical microscopy illumination technique. It can be further divided into transmitted light microscopy and emitted light microscopy. For the first type the simplest version is the brightfield light microscopy, while for the second there are for example fluorescence light microscopy and confocal light microscopy.

Brightfield light microscopy

Brightfield microscopy is primarily used for routine analysis such as monitoring cell number and analysing the morphology after scaffold bioprinting. With this type of microscopy, the image is created by the white light that is able to pass through the illuminated sample; contrast in the sample is caused by attenuation of the transmitted light in dense areas of the sample. Through light microscopy live cells can be viewed and recorded in real time and specific structures can be labelled for viewing reducing the “noise” in the sample. Nevertheless, it has a resolution of about 0.2 μm, which is its main limitation. Indeed, at this range it is possible to see bacteria and maybe even some large viruses (but not all and definitely not well). It can be seen also some of the larger subcellular organelles in a cell (like the nucleus and mitochondria), but not much of the smaller organelles. Thus, the limit of resolution restricts the amount of detail that can be seen of internal cellular structures [36].

Fluorescence light microscopy

Fluorescence light microscopy mainly differs from white light microscopy for the light source that comes from the samples themselves. Moreover, not only it allows to view

live samples, as other forms of light microscopy do, but it also allows to label (or tag) specific macromolecules / cell structure so that they can be racked within the cell. Structures are tagged using fluorescent molecules (called fluorochromes or fluorophores). Then, using fluorescent microscope, the sample is illuminated with light of a particular wavelength, and the fluorophore responds by emitting light at a second known wavelength that can be then detect. The great advantage of this technique is that only the molecule or structure of interest shows up in the image, and the rest of the sample, which is not emitting light, is dark. Moreover, it is possible to develop genetic engineering protocols so that one could add a fluorescent tag to any protein in the cell. Through fluorescence microscopy it is possible to assess differences in DNA content, cell viability, cell number, proliferation, differentiation and metabolic capacity of cells in bioprinted scaffolds thorough assay kits [36].

There are several chemical stains that can be added to live cells that latch onto specific components of cells and then fluoresce. This is known as *direct staining*. An example of this is DAPI. DAPI (4′,6-diamidino-2-phenylindole) is a blue-fluorescent DNA stain that exhibits ~20-fold enhancement of fluorescence upon binding to AT regions of dsDNA. It is excited by the violet (405 nm) laser line, and it is commonly used as a nuclear counterstain in fluorescence microscopy, flow cytometry, and chromosome staining. DAPI's spectral properties make it ideal for use with green (Invitrogen Alexa Fluor 488, FITC, GFP) and red (Invitrogen Alexa Fluor 594, rhodamine, Invitrogen Texas Red, mCherry, mKate-2) fluorophores in multicolor experiments. Because of its high affinity for DNA, it is also frequently used for counting cells, measuring apoptosis, sorting cells based on DNA content, and as a nuclear segmentation tool in high-content imaging analysis. DAPI is generally used to stain fixed cells since the dye is cell impermeant, although the stain will enter live cells when used at higher concentrations. Cell viability test can be conducted by using the ability of cells to exclude the nuclear dye propiudium iodide whereby nuclear staining indicates loss of plasma membrane integrity. Samples after immersion in dye solution are observed on an inverted fluorescence microscope: total cells are represented by phase image and dead cells by fluorescence one [20]. This is great when there is interest in exploring a sample for which a fluorescent live-cell stain exists. Sadly, that is not always the case.

Another option is *immunolabeling*. In this case, antibodies, bound to a fluorophore that has been specifically created to bind to the protein or structure of interest, are used to label the cell. If the structure/molecule of interest is on the cell surface, then this works just fine. However, if the structure is in the interior of the cell, then the antibody will have difficulty accessing it. In this case, the cell is usually treated with fixatives, which kill it but also hold everything in place. Then the membrane can be disrupted just enough to allow the antibodies to access the interior of the cell. Immunohistochemistry (IHC) is the most common application of immunostaining. For example, IHC can be applied for the detection of collagen types I and II, and cartilage PG in a bioink for cartilage reconstruction [37].

Confocal laser scanning microscopy (CLSM)

Confocal microscopy offers several distinct advantages over traditional widefield fluorescence microscopy, including the ability to control depth of field, elimination or reduction of background information away from the focal plane (that leads to image degradation), and the capability to collect serial optical. In light microscopy, illuminating light is passed through the sample as uniformly as possible over the field of view. For thicker samples, where the objective lens does not have sufficient depth of focus, light from sample planes above and below the focal plane will also be detected. In fluorescence microscopy, any dye molecules in the field of view will be stimulated, including those in out-of-focus planes. The out-of-focus light will add blur to the image reducing the resolution. Confocal microscopy provides instead a means of rejecting the out-of-focus light from the detector such that it does not contribute blur to the images being collected. Thus, this technique allows for high-resolution imaging in thick tissues. Moreover, a significant advantage of the confocal microscope is the optical sectioning provided, which allows for 3D reconstruction of a sample from high-resolution stacks of images [38]. CLSM can be used for cell viability assay and histological analysis [22]. Previously, it has been highlighted that the cells also affect the mechanical properties of the bioink; the mismatch of material results in stress concentration at the cell-matrix interface which in turn affects the mechanical properties of the material. There is also a weak force between the cells and the bioink, which affects the partial performance of the bioink. The traction between the cells and the bioink can be observed by the cell traction microscope, where CLSM is usually applied.

4.3.2. Electron microscopy

Electron microscopy works in a very similar way to light microscopy, except that it uses a beam of electrons instead of light to image the sample. Electrons have a much shorter wavelength than photons of the visible light spectrum, roughly 200,000 times smaller. Because of that, the resolution limit of an electron microscope is much smaller; there are some kinds of electron microscope that can view individual atoms. More commonly, the most used electron microscopes have resolution at a size range from 200 nm to 0.2 nm. As such, this resolution limit is small enough that a lot of the finer structural details inside the cell become visible. A single double helix of DNA is 2 nm in diameter, and the thickness of the average lipid bilayer is between 4 and 10 nm; it is possible to see both in an electron microscope. Since electrons can easily be scattered by air molecules, almost all electron microscopy is done in a vacuum.

Transmission electron microscopy (TEM)

TEM is analogous to traditional brightfield light microscopy, but with much greater capabilities with respect to magnification and resolution. The sample sits between the electron source and the detector so that the beam of electrons passes through the sample on its way to the detector. Empty spaces will show up as white in the image while areas where the electrons are absorbed by the sample will be grey or black.

SEM

If TEM provides high resolution images of inner structures, SEM generates high resolution images of surfaces only. Since this microscope also uses electrons to image, the magnification and resolution are similar to TEM. In SEM the sample is dried and coated with a very thin layer of gold, platinum, or another heavy metal. The electron beam is “scanned” across the surface of the sample. As the beam hits the sample, secondary electrons are scattered from the surface of the specimen. These are collected by a detector that builds an image electronically based on electron intensity (from white to black) [36].

Nevertheless, these two techniques have some limits such as the preparation of the sample, to withstand vacuum, that requires time.

5. THREE-DIMENSIONAL BIOPRINTING AS POTENTIAL TECNIQUE FOR AURICULAR CARTILAGE REPLACEMENT

Cartilage together with bone, skin, vasculature, heart and neural tissues is one of the tissues that can be generated by various bioprinting approaches. Cartilage is a highly hypocellular tissue with the only cell type being chondrocytes which do not divide in mature cartilage. Furthermore, it is one of the few tissues in the body that is not vascularized and does not possess any-self repair abilities: it does not contain any nerves or blood vessels to allow vascular transport of repair cells. Therefore, surgical reconstructive procedures are required to restore shape and function of the affected anatomical part when the cartilage tissue is damaged or congenitally deformed. From a reconstructive point of view, cartilage is tolerant to hypoxia, thus, auto transplanted cartilage has a good ability to integrate with the surrounding tissue without shrinkage or development of necrotic deformations. This is an important prerequisite for a successful long-term result of the reconstruction [37,39,40].

Auricular cartilage reconstruction for external ear is challenging as it demands constructing a complex structure with durability and aesthetically pleasant. Rib cartilage is the gold "autologous graft" and, even if it has some benefits such as long-term durability of the shape, it relies on the surgeon's expertise, unpredictable durability of the fabricated cartilage, donor site morbidity, complex and long-term surgical procedure and aesthetically undesirable results. Additionally, average compressive Young's Elastic Modulus of costal cartilage is higher than that of auricular cartilage, about 11.43 MPa. This mismatch may cause discomfort. On the other hand, synthetic implants, made from nonabsorbable polymers, have higher infection rates and complications and can eventually protrude. Silicone and Gore-tex have limited collagen ingrowth due to the low porosity (10 to 30 micrometres); while, porous high-density polyethylene, alloplastic material known as Medpor, is too much more rigid than auricular cartilage (227-307 MPa) that leads to unnatural feel and because of the mismatch there can be micro-movement between the skin and the implant contributing to extrusion. Indeed, this material has shown 15% complication rate including extrusion or infection [1,2]. Thus, novel therapies are required.

Owing to reproducibility, structural complexity, and high-precision control of the distribution of constituents such as cells, 3D bioprinting has received considerable attention; it is a promising and potential alternative technology for elastic cartilage [40]. Given the ability of this technology not only to spatially control the placement of cells, biomaterials and biological molecules, but also biofabricate biomimetic shaped 3D structures unique to target issue or organ if combined with CAM/CAD technology, the engineered auricular implant should ideally exhibit biochemical

and mechanical properties that are more similar to the native elastic cartilage. Furthermore, it improves the aesthetic outcome and eliminate the multiple-step surgical procedure that requires harvesting large pieces of rib cartilage, causing donor-site morbidity. [41].

Nevertheless, it is still challenging to fabricate and maintain, both *in vivo* and *in vitro*, the complex structure of human auricle [40]. Firstly, its unique shape requires a patient-specific approach while highlighting the anatomical details to ensure an aesthetically satisfactory result after implantation. Secondly, the maintenance of that shape should be ensured for a lifetime, requiring excellent cellular performance and long-term balance between stiffness and flexibility. This means that cartilage matrix deposition should be abundant and properly organize to appropriately mimic the native tissue's microscopic anatomy and biochemical properties. However, these properties of ear-shaped construct are inferior to the native situation, as well as deformation and collapse are frequently reported in long-term *in vivo* studies in part due to nutrient limitation and inferior mechanical integrity of the developing neo-tissue. Thirdly, the production of a large structure requires a significant number of autologous cells. Additional challenges in the application of a tissue-engineered cartilage implant for the reconstruction of the external ear are the limited availability of patient's cranial skin to sufficiently cover the implant and the requirement of high mechanical integrity of the implant to withstand the compressive forces of the overlying skin. These forces maybe generated while the patient put on a cap or sleeps on the later side. These challenges may be fronted by 3D bioprinting approach by employing customized patient-specific shapes with adequate reinforcement, potent regenerative cells and improved tissue quality [41]. The development of hydrogel-based bioinks, that may retain tissue-specific structural and functional molecules that regulate cell behaviour and tissue homeostasis, with bioactive properties that guide cellular fate processes and good printability would contribute to translation of this promising technology into clinic [24].

6. BIOINK FOR AURICULAR CARTILAGE

The goal of auricular cartilage 3D bioprinting is to fabricate a 3D artificial tissue consisting of cells and biomaterials which mimic the *in vivo* condition of auricular cartilage. A lot of efforts have been made for the searching of the biomaterial that meets all the requirements for auricular cartilage regeneration. The ideal material for the bioink of interest should have suitable sweeling property, short-term durability, but more than 7-21 days, and biocompatibility for long-term transplantation. Besides, since bioprinted tissue grow *in vivo*, it must be capable of remodelling and enabling the formation of structures according to cellular and physiological needs. Thus, an ideal material should support cellular attachment, function and proliferation. In addition, proper crosslinking mechanism is necessary to facilitate bioprinter deposition, particularly in case of complex structures like the ear. The scaffold should simulate the auricular cartilage tissue even in terms of mechanical properties to prevent deformation when implanted beneath the skin, providing the definition of the auricular shape and sustaining the external loads, generally of about 1/3 N [5].

6.1. Materials

Hydrogels are optimal biomaterials to be employed in bioink for auricular cartilage reconstruction because of their attractive properties described in chapter 3; chondrocytes typically grow and proliferate best in highly aqueous and homogenous environment. Precisely, natural hydrogels are widely used in cartilage tissue regeneration since they include polymers existing in ECM components, such as gelatine, collagen, laminin and fibronectin, along with other natural polymers such as chitosan, alginate, agarose, NC etc. Alginate has been widely used in 3D bioprinting cartilage tissue engineering applications and showed successfully results, enhancing neocartilage formation and maintaining the chondrogenic phenotypes of chondrocytes. Nevertheless, common challenge when 3D bioprinting hydrogels is that the printed shapes tend to collapse due to low viscosity. One solution can be increasing the concentration and molecular weight of alginate to augment its viscosity, but this is not enough for achieving shape fidelity while printing, thus, alternative methods should be adopted. To increase the structural fidelity and reach the desired mechanical stiffness, like cartilage requires ECM to be mechanically strong, hydrogels are often printed in combination. For example, alginate combined with chitosan has shown encouraging results for bioprinting elastic cartilage. Instead, alginate and agarose were found to be the best support for the formation of hyaline cartilage. While polyethylene

glycol methacrylate (PEGMA) and gelatine-methacrylic or acid (GelMa) based hydrogels better support fibrocartilage development. Alginate can be combined even with synthetic materials, such as PCL, because of their durability and appropriate mechanical strength. Even if, among the several reasons, the lower biodegradability and higher stiffness that may cause discomfort do not make synthetic materials the first choice for auricular cartilage reconstruction. Recently NC use in cartilage regeneration has gained a lot of attention, because of biodegradability and, excellent mechanical, barrier and colloidal properties [5,24].

6.1.1. Alginate

Alginate-based natural hydrogels have gained considerable attention. Alginate is a naturally occurring block copolymer comprised of a combination of β-D-mannuronate (M) and α-L-guluronate (G) polymer blocks, whose structure is represented in Fig. 14; the length of the connected G units is directly related to the mechanical properties, while the content of M units is related to immunogenicity [20]. Alginate has become one of the research hotspots because of its several attractive characteristics. First of all, in nature alginate exists in the form of sodium salt mainly in the cell wall and intercellular mucilage of different species of brown algae, such as *Laminaria* sp., *Durvillaea* sp. and *Sargassum* sp., as well as in some bacteria such as pseudomonas and nitrogen-fixing bacteria; thus, the structure and the source of alginate are abundant [43]. In addition, alginate has a favourable biocompatibility, biodegradability, solubility, stability, and specific physiological functions such hypoglycaemia, anti-oxidation and enhancing immune activity. Furthermore, due to the structural similarity of alginate to ECM, hydrogel gels are already used in cell delivery vehicles, drug delivery beads and ECM models for cell experiments matrices for TE. More importantly, the main chain of alginate contains a large number of hydrophilic groups such hydroxyl and carboxyl groups which are easy to modify, so alginate has attracted a great attention among biomedical materials. Nevertheless, alginate is known to quickly lose its mechanical properties and reverse back to its soluble form through ion exchange with monovalent cations [21,44]. Stiffness and degradability are important factors for cell proliferation. In many cases it is desirable to have the matrix material that degrades in a short time, allowing the material itself to be replaced with the host cells; furthermore, it has been reported that softer matrices allow better proliferation rather than stiffer gels since a less dense network structure lets cells be free to move, grow, divide and differentiate.

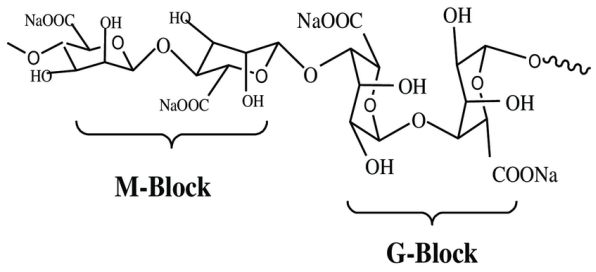

Fig. 14. Molecular structure of sodium alginate [42].

Anyway, cartilage reconstruction requires a scaffold with a certain degree of stiffness and that does not degrade in few days, otherwise preventing the formation of new tissue [44]. Several ways exist to strengthen alginate-based hydrogels. The viscosity of the alginate solution depends on the average molecular weight (Mw), the molecular weight distribution, the average chain segment ratio (G to M ratio), the concentration of the polymer and the pH of the solution; thus, increasing the concentration of the hydrogel constituent and so the density of the alginate, the compressive modulus increases and as consequence the hydrogel strength. Nevertheless, this strategy may make the hydrogel too much viscous that high shear forces are generated during printing, or it cannot be printed at all. The first case is dangerous for the viability of cells [44]. In a study researchers have increased the concentration of alginate up to 9-11%, with concentration of gelatine varying between 6-10%, to increase the mechanical properties of the blend; but the gelation occurred to rapidly and the blend was too viscous to be printed and undesirable for cells [20].

According to the previous considerations alginate printability can be changed, making this material an attractive hydrogel for bioprinting applications, by altering the polymer density but also through crosslink. This alternative makes alginate become structural. The preparation of alginate-based hydrogels involves several different chemical or physical crosslinking strategies, among which that from ionic bonds between divalent cations and carboxyl groups on alginate is the most common. However, the obtained pure alginate-based hydrogels may still have some disadvantages such as unstable performance and single function; therefore, the formation of composite hydrogels by introducing organic or inorganic units is one of the current research projects [21].

One solution could be combined alginate with other natural gels such as proteins, staches and hydrocolloids like chitosan and gelatine. Gelatine can be used to increase the viscosity of the hydrogel satisfying the extrusion and printing criteria. Moreover, since on its own alginate does not provide mammalian cell-adhesive ligands, gelatine can be added to facilitate cell adhesion and differentiation [20]. Nevertheless, if alginate is known to quickly lose its mechanical properties and reverse back to its soluble form through ion exchange with monovalent cations, gelatine reverses to its soluble form at physiological temperature. Indeed, due to a conformational change from coil to helix, at temperature above 35-40 °C gelatine is a solution, while if it is cooled under 29 °C it reversibly forms a gel [43,44]. In a study, it has been observed that the addition of gelatine increases the viscosity and the storage modulus of the hydrogel-based ink and the cell viability is over 90%, but all samples show close to 50% drop in modulus after 4 days in cell culture medium and more than 80 % after 14 days [44].

6.1.2. Nanocellulose

Even if the increase in the concentration and in the MW can augment the alginate viscosity, as seen in the previous sub-paragraph, that is not sufficient to achieve shape fidelity during printing and avoid that the printed scaffold collapses. Instead, printing hydrogels with other materials can be successful to increase the structural fidelity. Another material that can be added to alginate and that shows much better mechanical properties than gelatine is NC or NC fibrils, fibrils with one dimension in the nanometre range. NC is characterized by the general properties of cellulose: hydrophilicity and broad chemical modification capacity, combined with properties specific for nanoscale materials due to their high surface area [45]. Depending on the cellulose source and its processing conditions, cellulose nanofibrils are divided into three main categories: nanofibrillated cellulose (NFC), nanocrystalline cellulose (NCC) and bacterial nanocellulose (BNC). Different sources and preparation methods determine NC intrinsic properties, including morphology, size, mechanical strength and crystallinity. Some of their differences are shown in Table 1 [45]. Interestingly, NC has gained increased interest as biomaterial during the past decade due to its desirable characteristics which include renewability, abundance and low cost of the raw material (cellulose), as well as a large surface-to-volume ratio, high strength and stiffness, very low coefficient of thermal expansion, low weight, low density, high aspect ratio and biodegradability. Applications of NC include reinforcement of

composite materials, moistening masks for cosmetic applications, filtration media, thickening agents, rheology modifiers, adsorbents, paper reinforcement, etc. It is also attractive for biomedical applications due to its mechanical properties, biocompatibility and tissue integration capability. Several *in vitro* studies of NC scaffolds seeded with bovine articular chondrocytes and human articular, auricular and nasal chondrocytes have exhibited good cell adhesion, proliferation, and demonstrated the maintenance of chondrogenic phenotype; as confirmed by the synthesis of cartilage-specific ECM. Furthermore, bioinks with varying ratios of nanocellulose and alginate have been developed showing remarkable printability and offering a biologically relevant 3D environment. NC-based bioinks are highly viscous and shear-thinning, even at low solid content. Such properties make it possible to bioprint complex, 3D anatomically shaped constructs, such as human auricle [24].

Table 1. Differences between NFC, NCC and BNC in terms of size, crystallinity and mechanical strength.

Type of nanocellulose	Typical size	Crystallinity	Mechanical strength	Characteristic
Nanofibrillated cellulose (NFC)	High aspect ratio; lengths: 0.5–2 µm; diameters: 5–60 nm	Contain both amorphous and crystalline regions; crystallinity about 60%	Tensile strength: 1 GPa, Young's modulus: 30 GPa	Good biocompatibility, biodegradability, water retention
Nanocrystalline cellulose (NCC)	High aspect ratio (~70); the smallest nanoscale dimensions of any nanocellulose; lengths: 0.05–0.5 µm; diameters: 3–5 nm	Crystallization zone only; highly crystalline (54–88%)	Tensile strength: 7.5 GPa, Young's modulus: 120 GPa	High mechanical strength, high crystallinity, good biocompatibility, biodegradability
Bacterial nanocellulose (BNC)	Lengths: several micrometers; diameters: 20–100 nm	Super high crystallinity (up to 95%)	Young's modulus up to 70 GPa	High water absorption, high air permeability, porous structure, good biocompatibility, biodegradability, high purity, simple purification process, expensive

6.1.2.1. Cellulose

Cellulose is the most highly abundant, renewable, biodegradable biopolymer on earth [46]. Cellulose is the major component of wood and most natural fibres such as cotton, flax, hemp, jute, ramie and sisal; it is also produced by a family of sea animals called tunicates, by several species of algae and some species of bacteria, amoebae and fungi [47]. Irrespective of its source, cellulose is a white fibre-like structure with no smell and has a density of around 1.5 g/cm^3. Since its discovery by Payen, in 1838, the physical and chemical aspects of cellulose have been intensively studied [48]. Today it has, without any doubts, a hierarchical and complex structure that can be analysed on different levels: structural, morphological (macrofibrils, fibres, pores), supramolecular (microfibrils, crystalline and amorphous regions, and hydrogen bonds), and finally the molecular level (glucan chains and hydrogen

bonds). So, hierarchically, arrangement design within wood fibres consists of its growth rings, cellular structure, cell wall, fibril matrix, microfibrils and cellulose molecule. This structure means that the design is dived into different dimensional scale i.e. from macro-scale to nano-scale level [46]. Cellulose is a linear homopolysaccharide of -1.4-linked anhydro-d-glucose units with a degree of polymerization (DP) of approximately 10,000 for cellulose chains in nature. The basic chemical structure of cellulose shows a dimer called cellobiose that appears as a repeated segment. The monomer, named anhydroglucose unit (AGU), bears three hydroxyl groups. These groups and their ability to form strong hydrogen bonds confer upon cellulose its most important properties, like its multi-scale microfibrillated structure, hierarchical organization (crystalline vs. amorphous regions), the highly cohesive nature (with a glass transition temperature higher than its degradation temperature) and rigidity [48]. Coupled with the ability of the cellulose molecule to be chemically modified, it is reengineered into potential applications ranging from papermaking, coatings and films, nanocomposites, pharmaceuticals, separation membranes, rheological modifiers and biomedical engineering [46]. Therefore, cellulose and cellulose derivatives are used as the main components of TE scaffolds and often as conditioning agents for other natural polymers such as alginate [49].

There are four different polymorphs of cellulose: cellulose I, II, III, and IV. Cellulose I, native cellulose, is the form found in nature with a semicrystalline fibrillar structure which is the main source of NC. About 36 individual cellulose molecules are brought together by biomass into larger units known as elementary fibrils or microfibrils, which are packed into larger units called microfibrillated cellulose (MFC) or NFC. The latter are in turn assembled into familiar cellulose fibers. This organization is described in Fig. 15 [48]. Depending on their origin the microfibrils diameters may vary, but in general they are within 2-20 nm and several microns in length. The microfibrils are formed during the biosynthesis of cellulose chains: van der Waals forces and hydrogen bonding between hydroxyl groups and oxygen of adjacent molecules promote parallel stacking of multiple cellulose chains forming elementary fibrils that further aggregate into larger microfibrils [47]. Each microfibril can be considered as a flexible hair strand with cellulose

crystals linked along the microfibril axis by disordered amorphous domains. The ordered regions are cellulose chain packages that are stabilized by a strong and complex network of hydrogen bonds that resembles nanocrystalline rods. This is way there are two main types of NC: cellulose nanocrystals and cellulose microfibrils [48].

Although, as raw material, cellulose fibres and many of their derivatives have been known and used for more than a hundred and fifty years, in the last decade cellulose has received a revived interest based in the understanding that macrofibers are built up by smaller and mechanical stronger entities, microfibres, which can be extracted under proper conditions. Extraction of nano-scale cellulosic elements from ligno-cellulosic fibres is a lot of studied; it is traditionally performed mainly by two routes, acid hydrolysis and mechanical treatment, detailly illustrated in Fig. 16 [47].

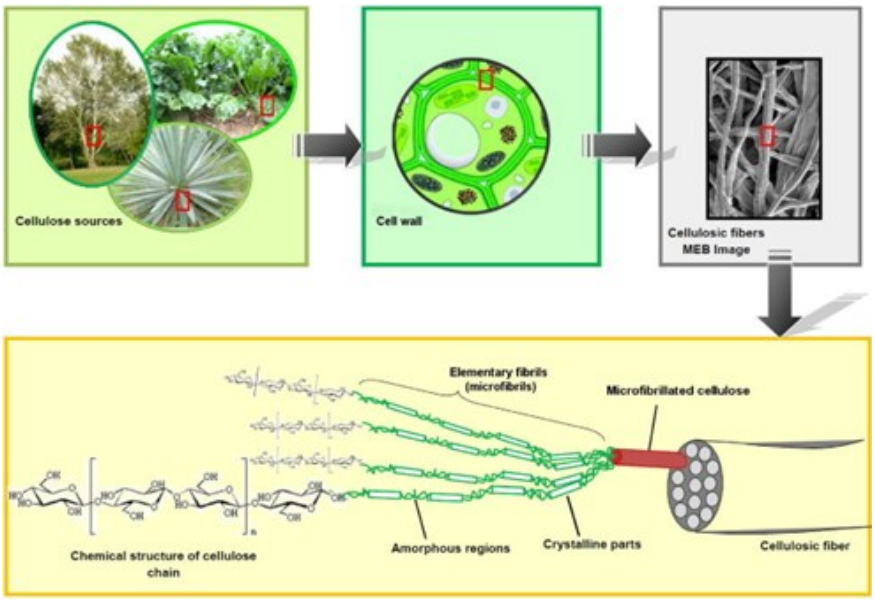

Fig. 15. From the cellulose sources to the cellulose molecules [48].

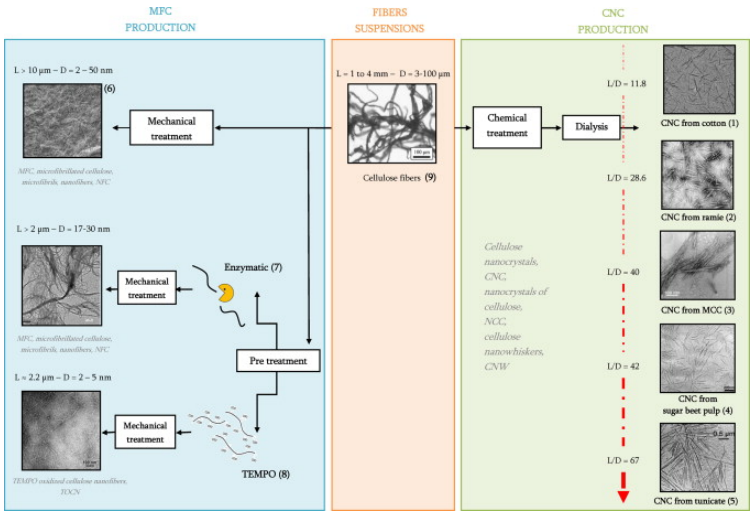

Fig. 16. From fibres suspension to different types of nanocellulose obtained through mechanical and chemical treatments [46].

It should be noted that there is still a lot of confusion regarding the terminology and nomenclature of NC. Indeed, many reports on NC are not consistent and do not make clear distinction between the different hierarchical levels, listed in Table 2 with specific dimensions. It must be pointed out that nanocellulose can be categorised into cellulose nanofibers and cellulose nanostructured materials. The first ones are subdivided into NCC and NFC; while the second ones are further sub-grouped into microcrystalline cellulose and MFC [46,50]. Although MFC and NFC are sometimes used as synonyms they differ in quality due to several reasons that include particle geometry (particle size and morphology), preparation method, raw material sources and surface chemical pretreatment involved. The defibrillation process generates fibres with smaller diameters for NFC (between 4 and 20 nm) and larger diameters for MFC (between 10 and 100 nm). However, this difference is not always considered and both terms appear in the literature interchangeably which may cause some confusion [51].

Table 2. Cellulosic nanomaterials dimensions [46].

Terminology and nomenclature of cellulose nanomaterials	Width (nm)	Length (nm)	Aspect ratio (length/width)
Cellulose nanofibril (CNF) Nanofibrillar cellulose (NFC)	2–10	>10,000	>1000
Cellulose nanocrystals (CNC) Nanocrystalline cellulose (NCC) Cellulose nanowhiskers	2–20	100–600	10–100
Cellulose microcrystal (CMC) Microcrystalline cellulose (MCC)	>1000	>1000	≈1
Cellulose microfibril (CMF) Microfibrillar cellulose (MFC)	10–100	500–10,000	50–100
Bacterial cellulose (BC) Microbial cellulose	10–40	>1000	100–150

6.1.2.2. Nanofibrillated cellulose

NFC is nanoscale cellulose obtained by degrading lignocellulose biomass; it is composed of many entangled nanofibers that contain amorphous and crystalline regions. NFC is prepared via high-pressure homogenization and grinding; mechanical treatment that imposes high shear forces to cellulose fibres, allows the extraction of microfibrils, thus nanofibrils. Size and strength of NFC depend mostly on source and preparation technique. It has an average length of approximately 0.5–2 μm, an average diameter of approximately 5–60 nm, a tensile strength of 1 GPa and a modulus of 30 GPa. Owing to its nanoscale size, NC has good mechanical capabilities, strong cell adhesion, good biocompatibility and water retention.

Globally, NFC has been reported positive outcomes in biomedical applications due to material-cell interaction and subsequent positive effects on cell fate processes which could be attributed to the highly hydrated cellulose nanofibrils and their morphological similarity with ECM components such as collagen. Furthermore, due to its high fidelity and biocompatibility, NFC-bioink is a great material for 3D bioprinting. NFC is used to modify the rheological characteristics of bioinks and enhance their printability; for example, many researchers have mixed NFC with alginate to compensate for its low zero-shear viscosity. Additionally, it has been found that cells encapsulated in NFC-Alginate bioink show moderate viability after bioprinting and crosslinking of the cell laden construct [24]. NFC-Alginate composite hydrogel scaffolds have

shown remarkable cartilage-promoting characteristic mainly due to NFC similarity in size to collagen fibres [49].

6.1.2.3. Nanocrystalline cellulose

NCC is the smallest of nanocellulose products with a length of 0.05–0.5 μm and a diameter of 3–5 nm; it is renowned for its high mechanical strength (~7,500 MPa), high aspect ratio (~70), amphiphilicity and high crystallinity. Indeed, compared with NFC, which contains amorphous regions, NCC contains only crystalline regions, which give it a more rigid structure. The preparation of NCC is more complex than that of NFC. Cellulose powder is first obtained by washing and mechanical grinding of lignocellulosic biomass, followed by purification via alkali treatment or acid-chlorite treatment to remove impurities, and finally, by acid hydrolysis to obtain NCC. The crystalline portions that are acid-resistant are maintained during acid hydrolysis, whereas the non-crystalline parts are hydrolysed because they are not acid-resistant. There are different preparation methods that have a direct effect on both morphological traits and physical properties: enzymatic hydrolysis against acid hydrolysis, the first one with better mechanical and heat properties, and sphere shaped NCC with greater heat resistance than usual rod-shaped NCC [49].

NCC is characterized by its high-water content capacity, good biocompatibility and excellent physical and chemical properties [33]. NCC has various applications in medicine, including TE, medication delivery systems and antibacterial agents [49]. Furthermore, its high biocompatibility and excellent printability make it the ideal material for 3D bioprinting; it offers fast gelling capacity when it is mixed with divalent cations, such as calcium, which enables the manufacturing of manageable scaffolds after bioprinting [33]. In bone and cartilage TE or even bioinks, NCC can be used as an enhancer, additive, or biomaterial to enhance the mechanical and biocompatibility of the scaffold. Indeed, NCC is often used in composite hydrogels since it promotes gelation through intermolecular hydrogen bonding, improving the mechanical properties of 3D bioprinting scaffold. Thus, inclusion of NCC enhances the viscosity, the Young's modulus, yield stress and energy storage modulus which significantly enhances printing as well as mechanical properties of the scaffold

[49]. Specifically, similarities in the chemical structure between alginate and CNC provide good compatibility: NC and alginate mixture as a bioink has been applied for the fabrication of 3D bioprinted scaffolds for cartilage regeneration as NC mimics the bulk collagen matrix of the cartilage tissue and alginate hydrogels have been reported to regenerate cartilage *in vivo* [33]. Additionally, chondrocytes cultured in NC-Alginate bioinks demonstrate proliferation and cartilage specific gene expression (Type 2 Collagen) over time indicating an inherent chondrogenicity of this material combination [3]. However, the addition of NCC results in low swelling efficiency, indicating a reduction in the capacity to absorb water, which may relate to the improved crosslinking ability of the composite scaffold [49].

6.1.2.4. Bacterial nanocellulose

The majority of cellulose is derived from plants, however in recent years another route for the production of micro/nanofibers of cellulose has received great attention. This is the microbial synthesis of cellulose in which specific bacteria, synthesize cellulose microfibrils as a primary metabolite. Cellulose molecules are synthesized in the interior of the bacterial cell and spun out to form nanofibrils which then aggregate in the form of ribbon-shaped microfibrils. The overlapping and intertwisted cellulose ribbons form a non-woven mat with very high-water content. Among different bacterial sources producing BNC with different properties there are *Acetobacter xylinum* and *Gluconacetobacter xylinus* which are the most widespread sources. Unlike plant cellulose, BNC does not contain lignin or hemicellulose; therefore, no complex steps, such as acidification and mechanical intervention are required for purification. Moreover, BNC has a high-water content, up to 99%, unmatched by other biomaterials, as well as the ability to absorb water of more than 100 times its weight. Additionally, BNC has a nanofiber network that is similar to the ECM, which has a significant impact on cell adhesion and migration. BNC is renowned for other qualities, including strong mechanical properties (Young's modulus up to 78 GPa), porous structure, and excellent biocompatibility. Thus, owing to its excellent mechanical properties and high fidelity, BNC is often used in addition to other bio-inks to modulate their properties. Furthermore, BNC fibrils, with their width of about 100 nm, are microscopically similar to collagen fibrils. This similarity makes this material

interesting to be used as component in scaffolds for soft tissues such as cartilage [45]. Nevertheless, BNC is more expensive than other cellulose derivatives because of high cost of the medium used to make it. Furthermore, BNC is limited in 3D printing because of the complex protofibrous structure that causes it to frequently clog the nozzles of 3D printers and to discourage cell migration [49].

6.2. Cells

The most preferred cell sources for cartilage TE are primary chondrocytes and stem cells. Primary chondrocytes are able to maintain cartilage ECM and more readily available, but they can only be obtained in a small amount from donor sites and have low proliferation rate. Stem cells proliferate easily, but they should be cautiously directed to differentiate into chondrocytes. Chondroprogenitors may act as a cell type intermediate to stem cells and chondrocytes, due to their high expansion capability, while preserving tendency towards chondrogenic differentiation. Typically, chondrocytes can be harvested from articular cartilages of low load bearing regions. But donor site morbidity after articular cartilage harvest remains a big drawback. Thus, harvest of nasal cartilage is advocated because nasal septoplasty is one of the most common operations performed in otolaryngology, with few sequelae or complications. Another benefit of utilizing nasal cartilage is that the proliferation rate of nasal chondrocytes is approximately four times of articular chondrocytes, making it possible to produce enough cells in limited time to engineer large pieces of cartilage. Nevertheless, another study showed that for auricular cartilage reconstructions, using cells derived from the auricle may lead to fabrication of elastin-containing cartilage, which has significant biomechanical and physiological functions. Chondroprogenitors are first detected in articular cartilage, and more recently it was also identified in the perichondral layer of auricular cartilage. Chondroprogenitors in auricular perichondral layer have high proliferation ability, generating a large number of progeny from a single founder cell while maintaining the ability towards chondrogenic differentiation and to produce elastic cartilage. In addition, stem cells derived from auricle are capable of reconstructing both the chondrium and perichondrium having the capacity to create and respond to tissue-specific developmental cues for normal growth regulations through the lifetime of an implant. Besides, chondroprogenitors proliferate quicker and generate cartilage ECM quicker than differentiated chondrocytes in cartilage TE.

Recently, MSCs have also been used as a substitute for chondrocytes in cartilage TE, mainly because of their easy availability, high in vitro expansion capacity and capability to differentiate towards chondrocytes. MSCs can be obtained from various tissues such as bone marrow, periosteum, synovium, adipose tissue, umbilical cord vein, and placenta. Moreover, human-derived induced pluripotent stem cell (iPSC) co-cultured with chondrocytes has also been bioprinted for cartilage lesion regeneration. iPSCs are able to maintain a pluripotent phenotype after 3D bioprinting, and chondrocytes could stimulate iPSCs differentiation by both cell-cell interaction and local inherent growth factors. In summary, there does not exist one single type of cell that is generally accepted as the best cell resource for auricular cartilage reconstruction, thus more research should be done to figure out the most optimal cell resource in this field. However, autologous cells are considered to be superior to allogenic cells due to the avoidance of immune rejection and reduced risk of transmitted diseases [5].

7. CROSSLINKING STRATEGIES OF ALGINATE BASED HYDROGELS

This section shows in detail those crosslinking strategies, introduced previously (sub-paragraph 6.1.1), used to increase the performance of alginate and alginate-based hydrogels respectively, such as NC-Alginate composite. Since alginate is composed of two structural units, G and M units, and contain a large number of reactive groups, there are several crosslinking strategies most of which realized by interaction forces between these reactive groups and other substances. According to these forces, the strategies can be divided into physical crosslinking and chemical crosslinking.

7.1. Physical crosslinking

Physical crosslinking is mainly characterized by interconnection of non-covalent bonds that include electrostatic interaction, hydrogen bonding, entanglement of molecular chains, etc. Among them the first one is one of the major strategies to form alginate-based hydrogels, including ionic crosslinking and macromolecular electrostatic crosslinking [21].

7.1.1. Ionic crosslinking

Combining alginate with divalent cations is the most common crosslinking strategy. Owing to the large amount of carboxyl groups in the structure, alginate can chelate with divalent metal cations to form hydrogels. Thus, the main method of crosslinking alginate-based hydrogels is through ionic crosslinking with Ca^{2+} ions; the addition of these ions causes formation of junctions between adjacent G-block polymer chains. Calcium ion binds to four G units forming a hexagonal lattice which is known as “egg-box” gel structure, shown in Fig. 17. The gelation rate can be modified by changing the temperature and the concentration of the crosslinking agent. The frequently used agent is $CaCl_2$ that is applied on the extruded after the printing process [20]. Studies have found that, although this crosslinking strategy is low-cost and simple in process, the obtained hydrogel usually has low mechanical properties and thermal stability, and it is prone to degradation under physiological conditions due to the exchange and release of Ca^{2+} ions into the surrounding media. These features maybe desirable only if the construct is designed to degrade over time and be replaced with cell-secreted ECM. Thus, alginate in physiological conditions releases Ca^{2+} due to the ion exchange reactions with Na^{+} present in culture medium. The ion exchange is facilitated

especially in phosphate buffered saline (PBS) than Dulbecco's Modified Eagle Medium (DMEM) because of its higher concentration of salt. Higher temperatures facilitate this exchange too [20]. Furthermore, calcium ions are cytotoxic in high doses: Ca^{2+} for ink preparation is osmotic and, thus, toxic to cells beyond certain concentrations, leading to disruption of homeostasis and to cell death. So, even if calcium ions are important in a variety of cellular properties such as enzyme activity, muscle contraction and cell proliferation, a low calcium concentration (2mM) must be maintained in the cytoplasm [44]. In addition, to make the crosslinking agent, like $CaCl_2$, effective, the printed scaffold must be taken immersed from 15 min to 30 min maximum. No better results have been shown with more time, but only side effects. Another agent used is $BaCl_2$ that releases Ba^{2+} as divalent cations. Barium gel is better than calcium gel in terms of stability, structural integrity and swelling degree. Nevertheless, barium is more cytotoxic in high concentrations. Generally, such alginate-based hydrogels crosslinked merely by cations have low mechanical strength, poor stability and rapid degradation rate. To overcome above problems other crosslinking strategies may be adopted [21].

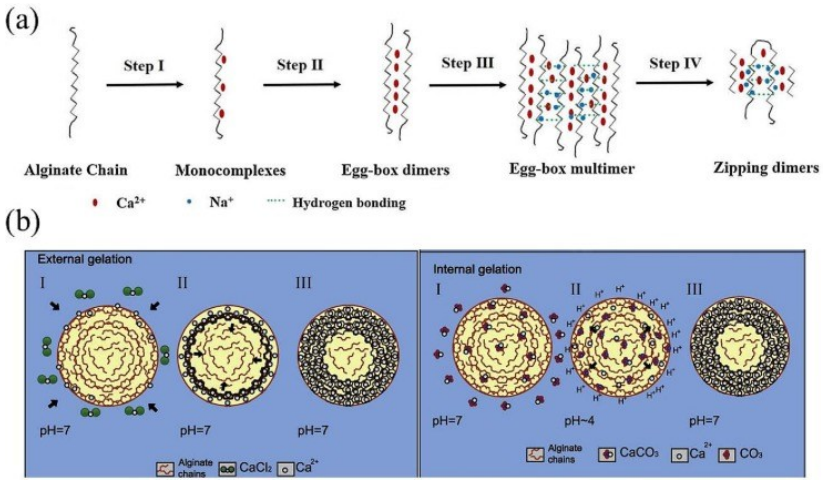

Fig. 17. (a) Schematic presentation of Ca-binding behaviours to alginate showing the "egg-box" structure; (b) the scheme of the external gelation method and the internal gelation method [21].

7.2. Chemical crosslinking

Because of the limited stability of the previous crosslinking agent, other crosslinking strategies have been considered such as chemical crosslinking, such as free radical polymerization crosslinking, and interpenetrating network (IPN) technology. However, these crosslinking strategies may introduce crosslinking agent, initiator and other toxic substances which limit their applications to a certain extent. Thus, there is research on strategies that limit the harmful effects. Chemical crosslinking refers to the 3D network structure formed by chemical bonding between monomers or polymers. Alginate contains a large number of reactive groups, such as hydroxyl and carboxyl groups, which are easy to be modified; the resulting alginate derivatives can be further polymerized or chemically reacted with other active groups to obtain chemical crosslinked alginate-based hydrogels. Compared with physical crosslinked alginate-based hydrogels, these hydrogels generally have higher mechanical strength and stability, which can be maintained for a longer time [21].

7.2.1. Free radical polymerization crosslinking

Free radical polymerization can convert linear polymers into 3D polymer networks, like that in Fig. 18. It uses free radicals generated by initiators to induce the formation of new free radicals on linear polymers under certain conditions of temperature, pH or radiation. So, the polymerization crosslinking is realized thorough the coupling of new free radicals.

Among the three conditions, photopolymerization has been widely used. The general principle is that in the presence of photoiniziator molecules, such as Irgacure 2959, Irgacure 1870, Lithium Phenyl-2,4,6-trimethylbenzoylphosphinate (LAP), VA-086 and VA-044, ultraviolet (UV) or visible light radiation is used to trigger polymerization of polymers containing unsaturated bonds (double or triple between carbon atoms) to form hydrogels. By itself alginate is not photopolymerizable, thus, to make it be able to react to UV radiation it has to be modified chemically. This can be done by adding photopolymerizable groups, such as acrylate, methacrylate, vinyl and other unsaturated units, into polymers like alginate. Then under the action of UV radiation of a certain wavelength, according to the initiator used, it is possible to obtain hydrogels with adjustable degradation rate and mechanical strength. Furthermore, studies have shown that these hydrogels have good cytocompatibility and low toxicity, and could encapsulate bovine chondrocytes in situ, and maintain its viability

and metabolic activity. The advantages of this method are mild reaction conditions, few by-products, and the mechanical properties and structural stability of the obtained hydrogels are far superior to those obtained by physical crosslinking. Therefore, photopolymerization crosslinking has attracted more and more attention [21].

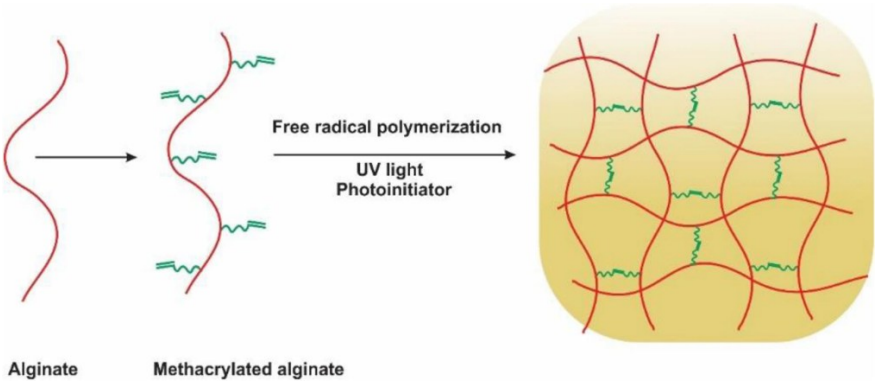

Fig. 18. Schematic representation of photocrosslinking of methacrylated alginate [52]

8. MATERIALS AND METHODS

8.1. Materials

8.1.1. Biomaterials and cells

Biomaterials

In this thesis low-cost Sodium-Alginate and CNC were used as biomaterials to realize the bioink for auricular cartilage reconstruction. Respectively, Sodium-Alginate, as thickening agent for alimentary use, was purchased from SaporePuro (Italy) and CNC hydrolysed from wood was supplied by Celluforce Inc. (Canada). The two products are shown in Fig. 18.

As chemical crosslinkers homemade $CaCl_2$ (80 mM), $CaCl_2$ (300 mM), $BaCl_2$ (0.5 mM) and $BaCl_2$ (3mM) solutions, and a solution of $BaCl_2$ (3 mM) and $CaCl_2$ (80 mM) were utilized at the bench.

DMEM with L-glutamine from Corning (USA), shown in Fig. 19 (left), was employed as culture medium. Absolute ethanol from PanReac AppliChem (ITW Reagents, Italy), imaged in Fig. 19 (right), was used to dry the scaffolds.

Cells

Primary Dermal Fibroblasts were used in this work. Normal, Human, Adult (HDFa) skin cell line was obtained from ATCC (Manassas, VA, USA). The cells were cultured in DMEM low glucose (Corning, New York, NY, USA) and added with 10% Fetal Bovine Serum (FBS) (Euroclone, Milan, Italy) and 1% antibiotic P/S (Euroclone). The cells were incubated at 37 °C in 95% air and 5% CO2 in CELBIO incubator. Subsequently, cells previously detached from a T75 flask were inoculated with EDTA trypsin (Corning) and counted using the LUNA II automatic counter (Logos biosystem, Annandale, VA, USA). Were used 1×10^6 number of cells for each matrix (alginate and CNC).

Fig. 18. Biomaterials used to produce the bioinks. On the left Sodium-Alginate powder for alimentary use from SaporePuro (ITA) while on the right spray-dried hydrophilic sulfated CNC from CelluForce (CA).

Fig. 19. On the left DMEM culture medium from Corning (USA) while on the right absolute ethanol from PanReac AppliChem (ITA).

8.1.2. Bioprinter

BIO X™ (CELLINK, Göteborg, Sweden), shown in Fig. 20, is the bioprinter employed in this thesis. It is a pneumatic-based extrusion bioprinter with up to three printheads for bioprinting hydrogel solutions and can easily fit in a standard biosafety cabinet allowing operation under sterile conditions: built-in UV sterilization and a HEPA filter bring the sterility of the biosafety cabinet to the benchtop. The availability of three printheads, enables multi-material and multi-cell flexibility during small and large TE. Moreover, with a printhead temperature range of 4°C to 250°C and a printbed temperature range between 4°C and 65°C, it ensures precise control of temperatures when working with temperature-sensitive materials. It operates with

DNA Studio 4 software that allows to select from a range of shapes and generate 3D models with just one tap. The software also allows to develop G-Code directly from an STL file; the G-code can also be edited effortlessly through the bioprinter thanks to an integrated G-Code editor [53]. Technical specifications of BIO X^{TM} are reported in Table 3.

The bioprinter works with several cartridges and nozzles; in this thesis a pneumatic 3 mL cartridge was used with a conical nozzle having a diameter of 410 μm. The tools are illustrated in Fig. 21. Moreover, the scaffolds and the human ear model were printed on a 6-wells plate and a Petri Dish like those depicted in Fig. 22.

Fig. 20. Cellink BIO X^{TM} bioprinter [53].

Table 3. BIO X™ Technical specifications [53].

Outer Dimensions (L x W x H)	484 mm x 441 mm x 365 mm
Weight	18.4 kg (40.56 lbs)
Build Volume	128 mm x 85 mm x 60 mm
Build Surface Compatibility	Multi-well plates, petri dishes, glass slides
Theoretical Resolution XY	1 µm
Theoretical Layer Resolution	1 µm
Pressure Range (internal pump)	0-200 kPa
Pressure Range (external air supply)	0-700 kPa
Printhead Slots	3
Photocuring Sources (built-in)	365 nm, 405 nm, 485 nm, 520 nm
Printbed Temperature Range	4-65 °C
Printhead Temperature Range	4-250 °C (printhead specific)
Filter Class, Chamber Air-flow	HEPA 14
UV-Sterilization	UV-C (275 nm) 20 mW output
Calibration Options	Manual and Automatic
User Interface	Integrated Display, Tablet or Computer
OS Compatibility	Windows
Connectivity	Ethernet
Supported File Formats	.gcode, .stl, .amf, .3mf, .obj

Fig. 21. Bioprinter tools. On the left sterile standard conical bioprinting nozzles, in the order Green-18G, Pink-20G, Blue-22G, Red-25G, Clear-27G, while on the right empty 3 mL pneumatic cartridge [53].

Fig. 22. Bioprinter tools. On the left 6-wells plate (Falcon), flat bottom and on the right cylindrical glass Petri Dish (Cellink) with dimensions 10x10x2 cm.

8.1.3. Tools and devices used for bioink preparation and characterization

For the preparation of the CNC-based blends tools and devices in Fig. 23 were used.

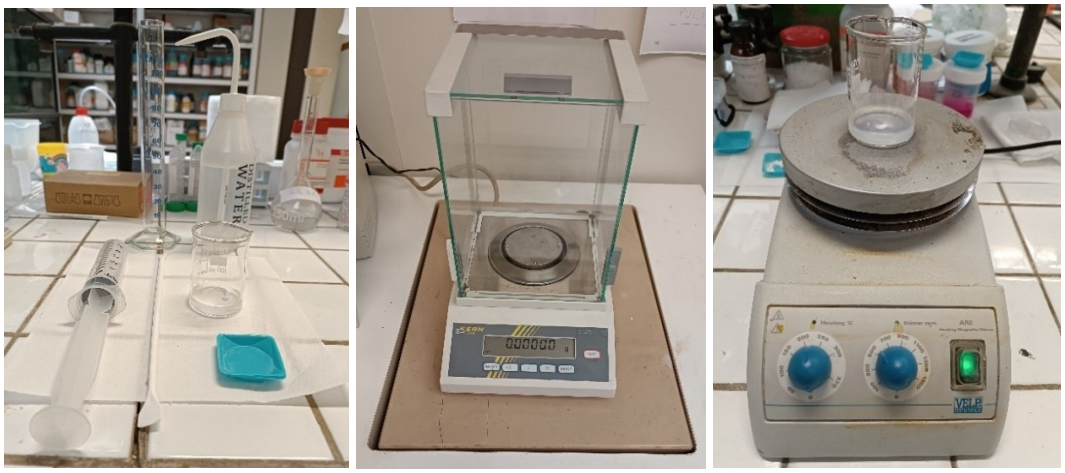

Fig. 23. From left to right: tools used for the preparation of CNC-based hydrogels, analytical balance (KERN), magnetic stirrer (VELP).

While for some characterization tests a digital calibre and a MCR 702e Anton-Paar rheometer (Graz, Austria) equipped with Peltier system for temperature control were employed (Fig. 24).

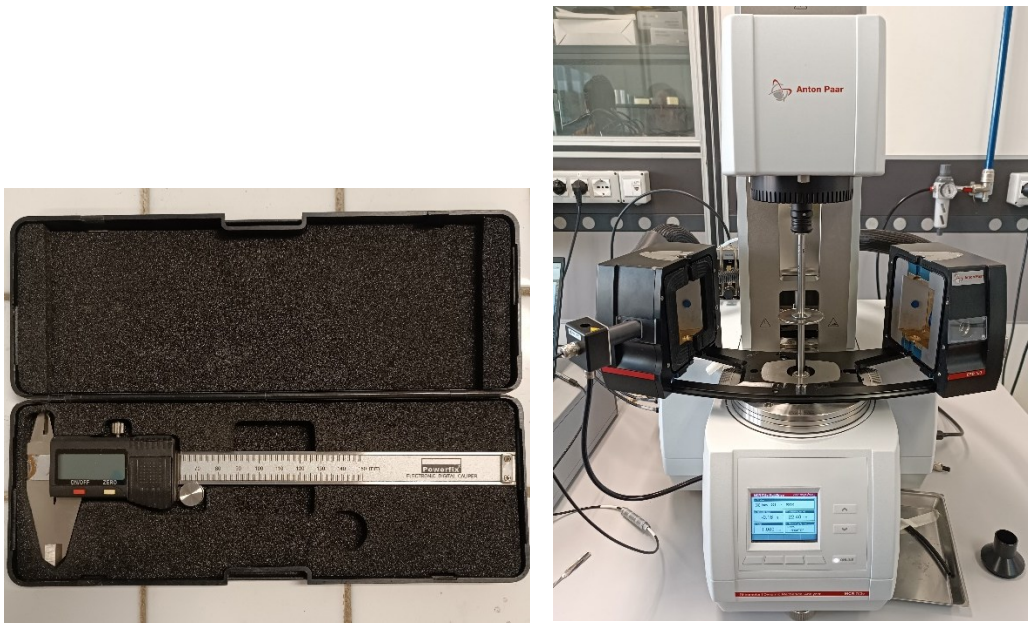

Fig. 24. From left to right: electronic digital calibre (Powerfix) with a measurement range between 0 mm and 150 mm and a resolution of 0.01 mm and MCR 702e Anton-Paar rheometer (Graz, Austria).

8.2. Methods

8.2.1. Bioink preparation and optimization

In this section all the steps performed to obtain the CNC-based bioinks at different concentrations are listed. Different preparation methods were tested, as well as several formulations, to select the best one in terms of bioink printability and shape fidelity, and thus able to realize a complex structure like the auricle.

8.2.1.1. Crystalline nanocellulose-Alginate bioinks

Seven bioinks, listed in Table 4, with different concentrations of both CNC and alginate were prepared by using the tools and the devices illustrated in the sub-sub-chapter 8.1.3.

For the preparation of sample 2/4 three different methods were evaluated in terms of viscosity and printability of the obtained blends. The best method was then adopted for all the samples.

Firstly, independently of the method used, both CNC and alginate powders were weighted. Then, the following procedures, varying among the three methods, were followed:

- *Method 1*: CNC and alginate powders were dissolved in distilled water separately, then the obtained solutions were mixed by stirring until a homogeneous blend was got. Specifically, CNC was dispersed by stirring, while for alginate two ways of dissolution were tested, by deposition and by magnetic stirring, as illustrated in Fig. 25 (a, b, c).
- *Method 2*: CNC was dispersed in distilled water by stirring, then alginate was added and dissolved by deposition. So, the stirrer was finally employed to homogenize the obtained solution.
- *Method 3*: it is like the second method, but alginate was dissolved in CNC-based solution by deposition and stirring concurrently and sufficiently to ensure a good dispersion of the first material into the second one, as shown in Fig. 25 (d).

Table 4. List of bioinks prepared with different concentrations of alginate and CNC.

Bioink Formulation	Alginate (% w/v)	CNC (% w/v)	Water content (% w/v)
2/1	2	1	97.1
2/3	2	3	95.2
2.5/3	2.5	3	94.8
2/4	2	4	94
2.5/4	2.5	4	93.9
3/4	3	4	93.5
2/5	2	5	93.5

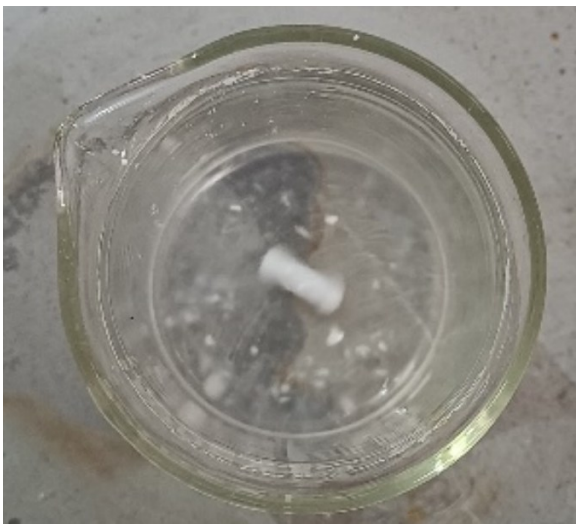

(a)

(b)

(c)

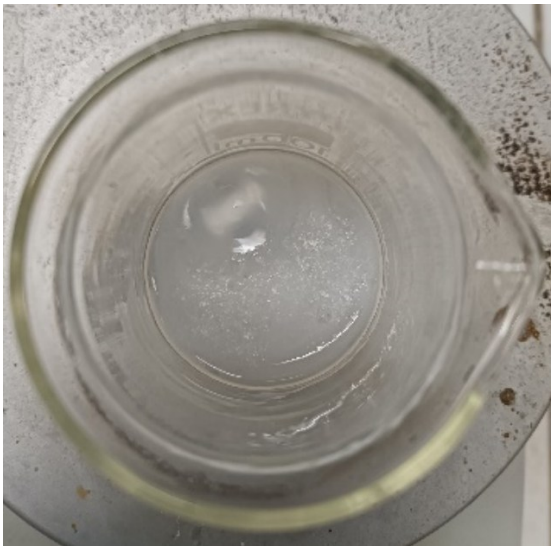

(d)

Fig. 25. Three possible methods for the preparation of CNC-based bioinks. (a) Dispersion of CNC in distilled water by stirring, (b) dissolution of alginate in distilled water by deposition and (c) by stirring, and (d) dissolution of alginate in CNC-based solution by deposition and stirring concurrently.

8.2.2. Three-dimensional bioprinting process

Each bioink, once prepared, was transferred firstly into the pneumatic cartridge (3 mL) through the big syringe, then printed. Before starting to print, a protocol for the bioprinter was edited where the model and the printing parameters, such as velocity and pressure, were set. Then the bioprinter was automatically and manually calibrated. The first calibration allowed the bioprinter to know the position of the printbed while the second to fix the position and distance of the cartridge from the substrate where the material was printed. All the scaffolds were printed by using only one cartridge, and with the printbed and the printhead temperature of 20 ±3 °C.

In Table 5 are shown the seven models employed according to the type of test performed while in Table 6 are listed the printing pressures, one for each formulation. Only the bioinks on which the tests of the following chapters were performed have been reported. The models are available in the bioprinter, but the cylinder was realized in Rhinos, then uploaded.

Once the scaffolds had been printed, they were crosslinked to confer them structure and stability. In this thesis each scaffold was crosslinked by ionic crosslinking. Five different ionic crosslinkers were tested, as introduced in sub-sub-chapter 8.1.1. Each scaffold was immersed in the aqueous solution, then removed after 15 min in case of $CaCl_2$ (80 mM), 5 min in case of $CaCl_2$ (300 mM) and 7/10 min in case of $CaCl_2$ (80 mM) mixed with $BaCl_2$ (3 mM). Time of immersion was chosen according to the

literature and the behaviour of the scaffold immersed. Thus, the ionic crosslinker as well as the bioink that limit the deformation of the scaffold during crosslinking immersion were searched. After being removed from the solution the scaffold was washed with distilled water to remove the excess of the ionic crosslinker, then eventually subjected to some tests.

Table 5. List of models with some printing characteristics used to print the scaffolds.

MODEL	CHARACTERISTCS
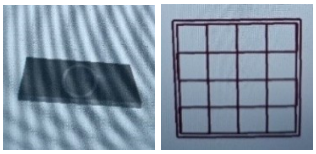	• Dimensions: (20x20x1) mm • Pattern: grid • Infill: 15% • 2 layers
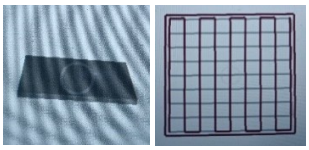	• Dimensions: (20x20x1) mm • Pattern: rectilinear • Infill: 15% • 2 layers
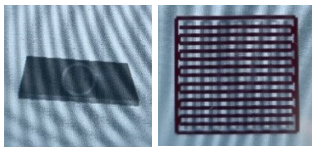	• Dimensions: (20x20x1) mm • Pattern: rectilinear • Infill: 25% • 2 layers
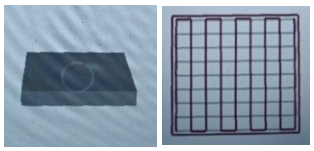	• Dimensions: (20x20x3) mm • Pattern: rectilinear • Infill: 15% • 7 layers
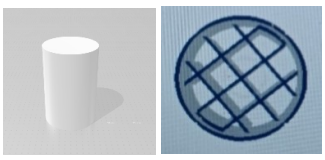	• Dimensions: (10x14,76) mm • Pattern: grid • Infill: 30% • 36 layers
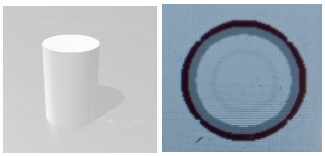	• Dimensions: (10x14,76) mm • Pattern: none • Infill: 0% • 36 layers

Table 6. Printing pressure for each bioink.

BIOINK	PRESSURE (kPa)
2/4	24 ± 2
2.5/4	41 ± 2
3/4	70 ± 2
2/5	40 ± 2

8.2.3. Bioink printability assessment

Rheological measurements were performed to assess the viscosity and behaviour of the blends under stress conditions, like those through the nozzle. Thus, it was possible to establish the goodness of the selected bioinks for bioprinting.

On the other hand, to identify the best formulation able to realize a detailed and high structure like that of the ear, the capability of the bioinks to realize high resolution and stable scaffolds was analysed. Thus, resolution and stability evaluations were performed. In the first analysis, the capacity of each bioink to realize a straight thin filament and the rectilinear models (height: 1 mm) with higher infill was evaluated. While in the second analysis, higher structures (height: 1 mm and 14,76 mm) were considered.

The printability tests, as well as the characterization ones, were performed only on 2/4, 2.5/4, 3/4 and 2/5.

8.2.3.1. Rheological measurements

The rheological properties of polymeric inks were investigated at 25 °C (bioprinting temperature) by using the rheometer shown in Fig. 24. The analyses were performed using plane–plane geometry. The upper geometry was a 25 mm of diameter with steel parallel plate with a gap of 1 mm and a loading gap of 60 mm. The shear viscosity (η) of the gels was determined as a function of shear rate ($\dot{\gamma}$) in stationary shear flow conditions, for $\dot{\gamma}$ varying in the range 0.01 s^{-1} – 1000 s^{-1}. The CNC-based gels were compared to commercial NC-based product, Bioink (Cellink).

8.2.4. Bioink characterization

8.2.4.1. Shape fidelity and shrinkage tests

Grid scaffolds (20x20x1mm, 15% infill) were printed by using the four selected bioinks and each one was evaluated in terms of shape fidelity. Thus,

for each scaffold a minimum of 6 grid areas was measured and compared to the designed area.

Owing to the large amount of preserved water in the network of hydrogels, comparison of the mean dimensions of each sample, crosslinked with $CaCl_2$ (80 mM) solution, before and after ethanol-drying was performed too. As scaffold dimensions, the line width, and the side length and width were considered. Measurements, for both the evaluation of the shape fidelity and the shrinkage, were taken through the digital calibre.

8.2.4.2. Swelling test

To analyse the uptake capacity of the bioinks, firstly each printed and crosslinked, with $CaCl_2$ (80 mM) solution, rectilinear scaffold (20x20x1 mm, 15% infill) was dried by ethanol and by air. So, the scaffold was immersed in absolute ethanol for 20 min, then removed and air-dried for other 20 min. After being weighted by using the analytical balance, the dried sample was put in DMEM at room temperature and weighted again at fixed time points: 5 min, 10 min, 15 min, 30 min, 45 min, 1 h, 1 h and 30 min, 24 h, 48 h and 72 h. At each time point, before recording the weight, the sample was systematically tapped 3 times to wipe off the excess of DMEM, and, after the measurement, it was immersed again in culture medium. Thus, the swelling ratio was computed for each time point by applying the eq. (8). The swelling test was performed even in water for 2/4, 2.5 and 2/5 bioinks.

The swelling test, for 3/4 only, was also performed on the scaffold crosslinked with $CaCl_2$ (80 mM) mixed with $BaCl_2$ (3 mM) solution. Then, results were compared to those obtained by crosslinking the bioink with $CaCl_2$ (80 mM) solution.

8.2.4.3. Degradation test

The degradation properties of the hydrogels were evaluated in terms of gel release. Thus, the printed grid scaffold, once crosslinked, with $CaCl_2$ (80 mM) solution, and dried, was weighted and then immersed in DMEM at room temperature. The gel release was calculated, by using eq. (11), 7 and 14 days after immersion in culture medium.

The test, for 3/4 only, was also performed at 37 °C constant temperature and the gel release was calculated 7 days after immersion in culture medium.

8.2.5. External ear reconstruction

Following the bioprinting process described in the sub-chapter 2.2, the first step to reconstruct the external ear was to get the CAD model of the designed organ. Firstly, it was attempted to obtain the human auricular model through a laser scanner (CREAFORM). Finally, an ear model available on the bioprinter library was employed. After being chosen the bioink formulation to use and set the several printing parameters and the model pattern and infill, the auricular structure was printed.

8.2.6. Preparation and three-dimensional bioprinting of cell-laden bioink

To prepare the cell-laden bioink, the cells were detached from T75 flasks (Corning), using trypsin-EDTA, then pelleted by centrifugation (250 rpm x 5 minutes), and resuspended in 1 mL of specific medium for these cells. Finally, cell suspension was mixed with the gel according to the following procedure. 100 µL of the obtained cell pellet and 1 mL of bioink (3/4) were taken and mixed. The mixture was performed by connecting the cartridge containing the bioink and the 1 mL Luer lock syringe with the cell suspension, as illustrate in Fig. 26, and gently mixing back and forth between the syringes. At the end the obtained mixture was loaded in the printing cartridges (CELLINK Inc, Sweden). The cell-laden bioinks had final concentrations of cells of 5×10^5 ml^{-1}.

Grid scaffolds (10x10x0.8 mm) were printed at 24 °C on a 6-wells plate using 22 G nozzle and with a printing pressure and velocity of 36 kPa and 2 mm/s respectively. After printing, the cell-laden scaffolds were crosslinked with $CaCl_2$ (80 mM) for 15 min. Once crosslinked, the scaffolds were washed with sterile PBS (Corning) to remove the excess of $CaCl_2$. Then, they were cultured in the six-wells plate with 5 ml of culture medium DMEM (Fig. 19) in the incubator (37 °C, 5 % CO2).

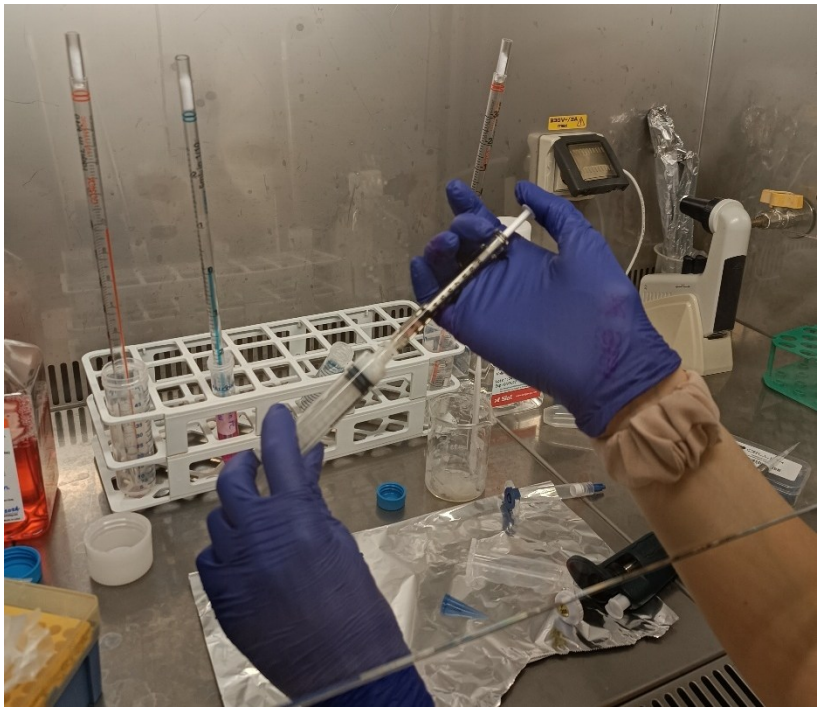

Fig. 26. Cellink cartridge loaded with CNC-based bioink and Luer lock syringe with cell suspension.

8.2.7. Cell-laden bioink characterization

8.2.7.1. Optical microscopy

The phase contrast optical microscope by Nikon (Nikon Europe, Amstelveen, The Netherlands) (Fig. 27) was used for monitoring cell proliferation over time, 1 day and 6 days after the culture in incubator.

Further analysis was conducted using Haematoxylin and Eosin Staining (H&S). Scaffolds were fixed in a 4% paraformaldehyde solution (Sigma-Aldrich, Merk, Darmstadt, Germany) and then embedded in paraffin. To prepare the paraffin sections, rehydration was carried out using xylene and a series of ethanol solutions with gradually decreasing concentrations. After washing with 50% ethanol, the sections were placed in distilled water for 5 min. The sections were then stained with haematoxylin (Bio-Optica, Milan, Italy) for 2 min, followed by rinsing in distilled water, and subsequently stained with Eosin (Bio-Optica) for 2 min. Another distilled water rinse followed the staining. The samples were then dehydrated through a graded ethanol series in ascending concentrations, treated with xylene, and finally mounted using Eukitt mounting solution (Orsatec GmbH and Co., Bobingen, Germany).

8.2.7.2. *Fluorescence microscopy*

DAPI staining was used to assess the presence of spheroids, proliferation and apoptosis in the spheroids. Sterile PBS was used to dilute the DAPI solution (ThermoFischer) to the final concentration of 300 nM. Firstly, the scaffolds containing the spheroids were washed 1–3 times with PBS and then were coated with the fluorescent dye solution of DAPI (300 nM) and incubated for 1–5 min, covered with silver paper to protect them from light. Finally, the solution was removed by washing 2–3 times with PBS and images were acquired by using a Nikon fluorescent phase contrast light microscope.

Fig. 27. Phase contrast optical microscope by Nikon (Nikon Europe, Amstelveen, The Netherlands)

8.2.7.3. *Field Emission Scanning Electron Microscopy*

The microstructure of the CNC-based hydrogel constructs was investigated using Field Emission Scanning Electron Microscopy (FE-SEM) ZEISS SUPRA 40 (Zeiss, Oberkochen, DE) from UNIVPM SIMAU Department. Both hydrogels with and without cell suspension were visualized. Inclusion procedure for SEM visualization of the samples is reported in Table 7.

Table 7. Inclusion procedure for SEM visualization.

1.	Fix the samples in gluta-para (2%) overnight
2.	Dilute 1:1 with (phosphate buffered saline) PBS
3.	Wash with PBS for 15 min at RT
4.	Post-fixation in 1% osmium tetroxide in PBS at 4°C for 1 hour
5.	Wash with PBS for 15 min at RT
6.	Dehydrate in EtOH at different concentration (20, 50, 70, 80, 95 %)
7.	Insert the samples into the filter paper sachets and place them in a beaker with 100% EtOH (4x15 min EtOH)
8.	Dry the samples using Critical Point Drying (CPD) with hexamethyldisilane (HMDS) (Sigma-Aldrich, Gillingham, UK)
9.	Mount the samples on aluminium stubs with graphite-based glue or with self-adhesive carbon discs (depending on the morphology of the sample) and store them in a small box (with silica gel) in a non-humid (dry) place.
10.	Samples on aluminum stubs are sputter-coated with gold before the visualization.

8.2.8. Informatic tools

GraphPad PRISM 10 (version 10.4.1) was used for statistical analyses while Microsoft Excel spreadsheet-Office Home Student 2020 was used for further data analysis and graphical representation. Statistical analyses for multiple comparisons were performed by non-parametric Krustal-Wallis test, followed by a post-hoc test. A value of $p < 0.05$ was considered statistically significant.

9. RESULTS

In this chapter results of the procedures, analyses and tests described in the previous sub-chapter (8.2) are reported in the form of tables, images and graphs.

9.1. Bioink preparation methods

As seen previously three different methods of blend preparation were tested and seven different formulations of CNC-based bioink were prepared. This section highlights how the preparation method and the formulation have influenced the bioink itself.

Fig. 28 shows how the same type of bioink, 2/4, varies, according to the preparation method adopted, in terms of appearance and printability.

While apparent different viscosities among the seven blends can be observed in Fig. 29, Fig. 30 and Fig. 31.

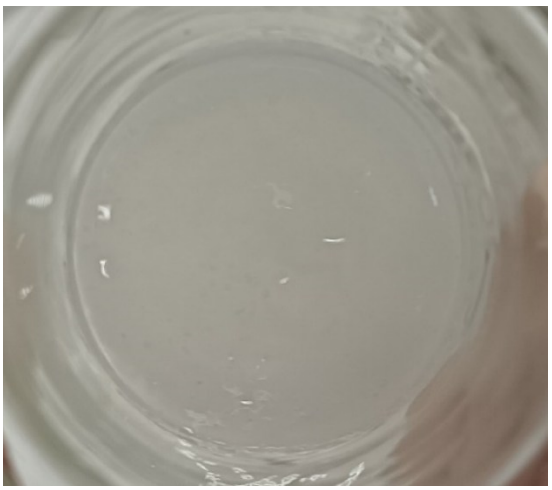

(a1)

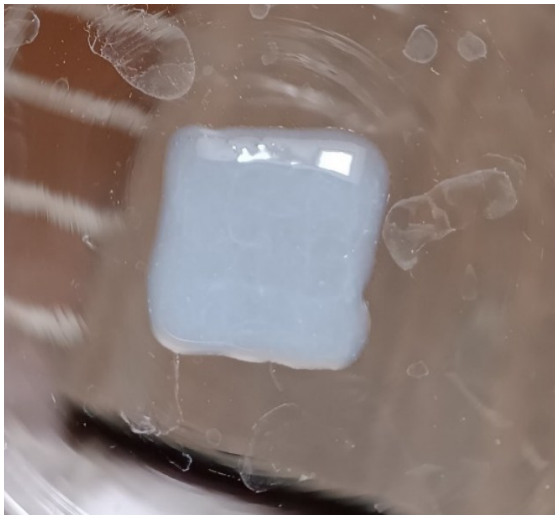

(a2)

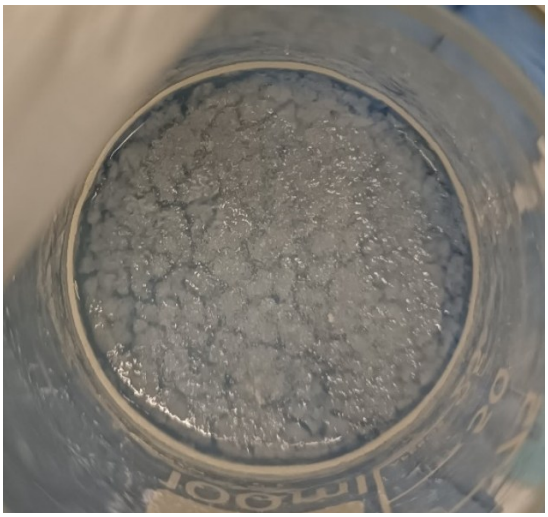

(b1)

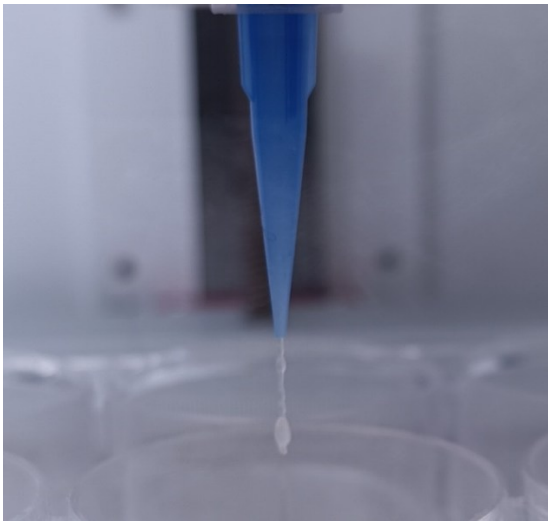

(b2)

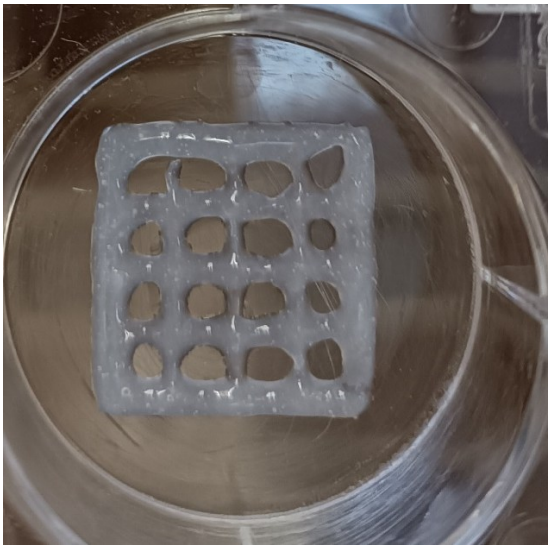

(b3)

(c1)

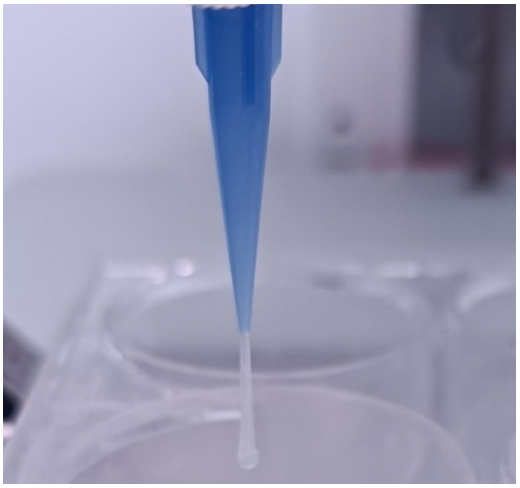

(c2)

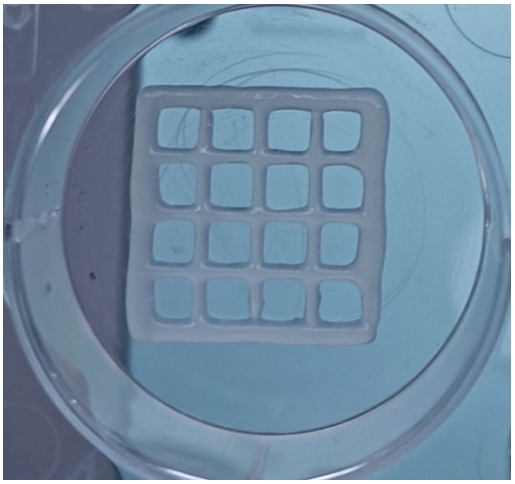

(c3)

Fig. 28. Variation of 2/4 bioink in terms of appearance and printability changing the preparation method: (a1, a2, a3) method 1, (b1, b2, b3) method 2 and (c1, c2, c3) method 3. (b2, c2) and (b3, c3) represent the filaments from the nozzle and the grid scaffolds respectively.

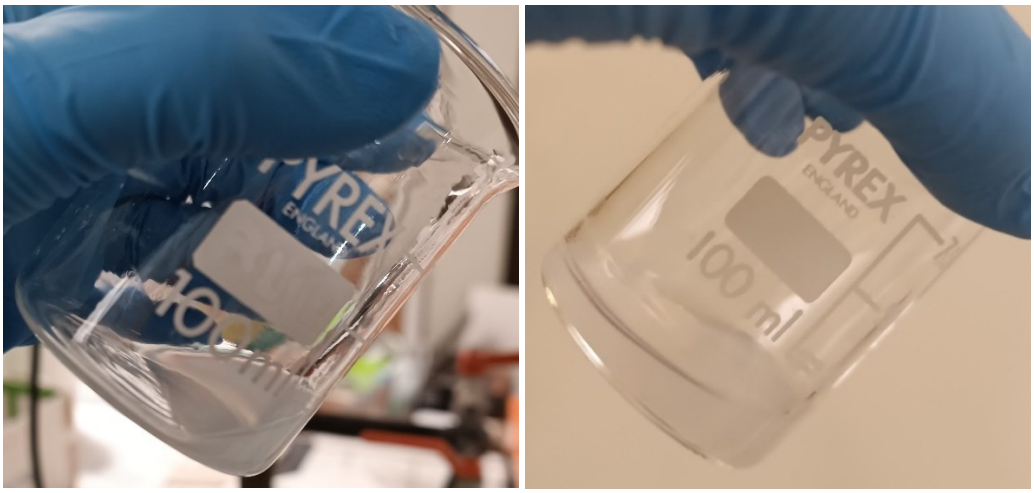

(a) (b)

Fig. 29. Two different concentrations of CNC-based solution: (a) 1% w/v and (b) 5% w/v.

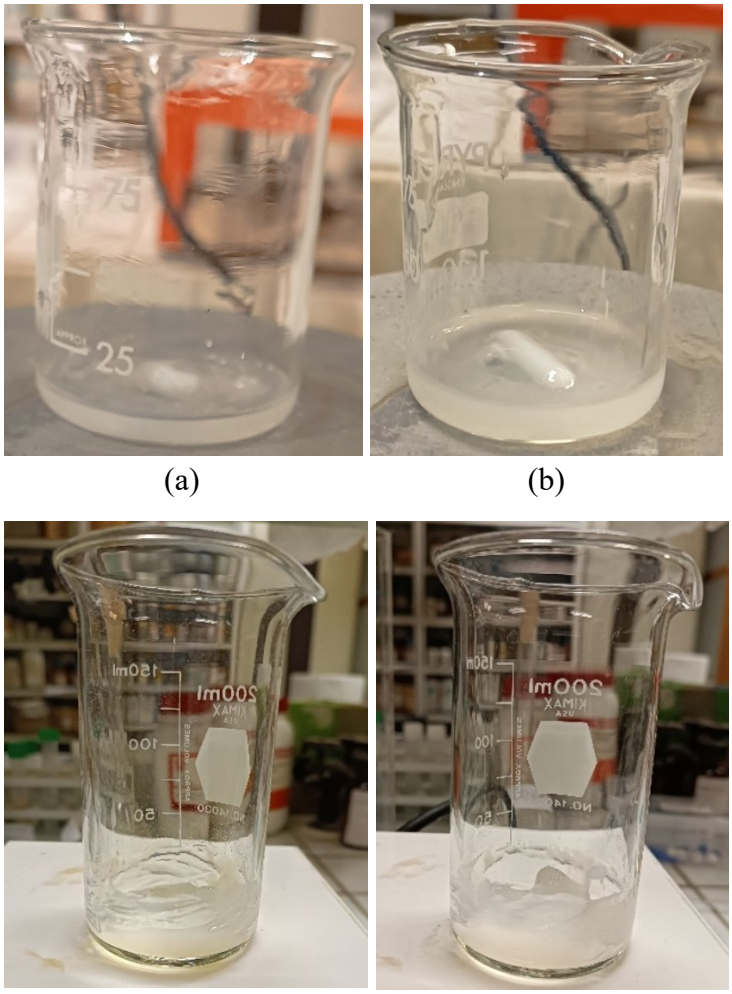

Fig. 30. Apparent variation of CNC-based bioink, prepared following the method 3, increasing the concentration of CNC and keeping constant the concentration of alginate: (a) 2/1, (b) 2/3, (c) 2/4 and (d) 2/5.

(b)

(c)

Fig. 31. Apparent variation of CNC-based bioink, prepared following the method 3, increasing the concentration of alginate and keeping constant the concentration of CNC: (a) 2/4, (b) 2.5/4 and (c) 3/4.

9.2. Bioink printability

The images in Fig. 32 show the first grid scaffolds printed to assess the printability in terms of apparent shape fidelity of the seven bioinks.

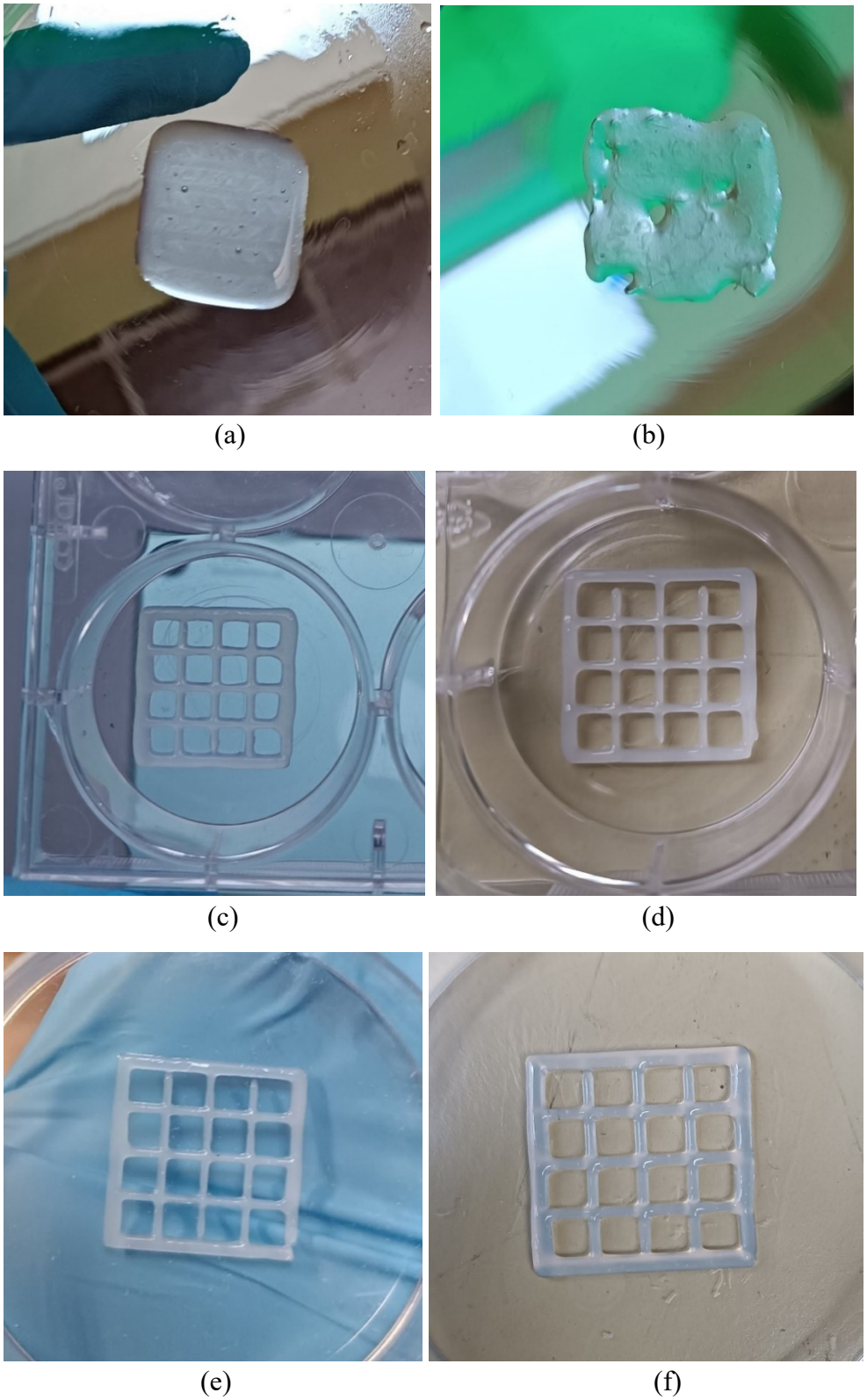

Fig. 32. Printed grid scaffolds whose bioink formulations are: (a) 2/1, (b) 2.5/3, (c) 2/4, (d)2.5/4, (e) 3/4 and (f) 2/5.

9.2.1. Rheological measurements

The results of the rheological analysis are reported in Fig. 33.

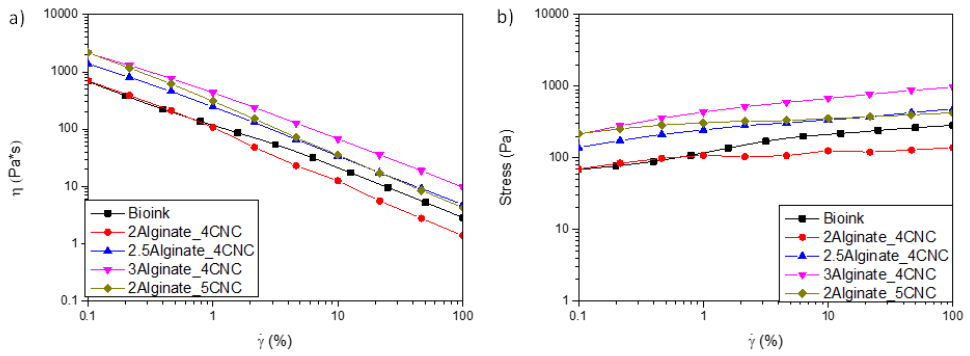

Fig. 33. Viscosity (a) and stress (b) as function of shear rate (γ̇) for Bioink (Cellink) and Alginate_CNC based gels.

9.2.2. Resolution

In this section the results of the evaluation of the selected bioinks, respectively 2/4, 2.5/4, 3/4 and 2/5, in terms of resolution are illustrated through images and tables.

The results related to the capacity of each selected bioink to produce a straight thin filament are shown in Fig. 34.

While the results of the resolution evaluation through rectilinear scaffolds are reported in Fig. 35, Fig. 36 and Fig. 37.

Table 8 contains the mean dimensions of the four rectilinear scaffolds (height: 1 mm) once printed. Thus, the rows of the table represent the line width, and the side width and length of the scaffolds, while the columns are the four bioinks, 2/4, 2.5/4, 3/4 and 2/5.

Table 9 contains the mean dimensions of the rectilinear scaffolds (height: 3 mm), realized with 2.5/4, 3/4 and 2/5, once printed. It differs from Table 8 only for one more row associated to the scaffold height and the reduced number of columns.

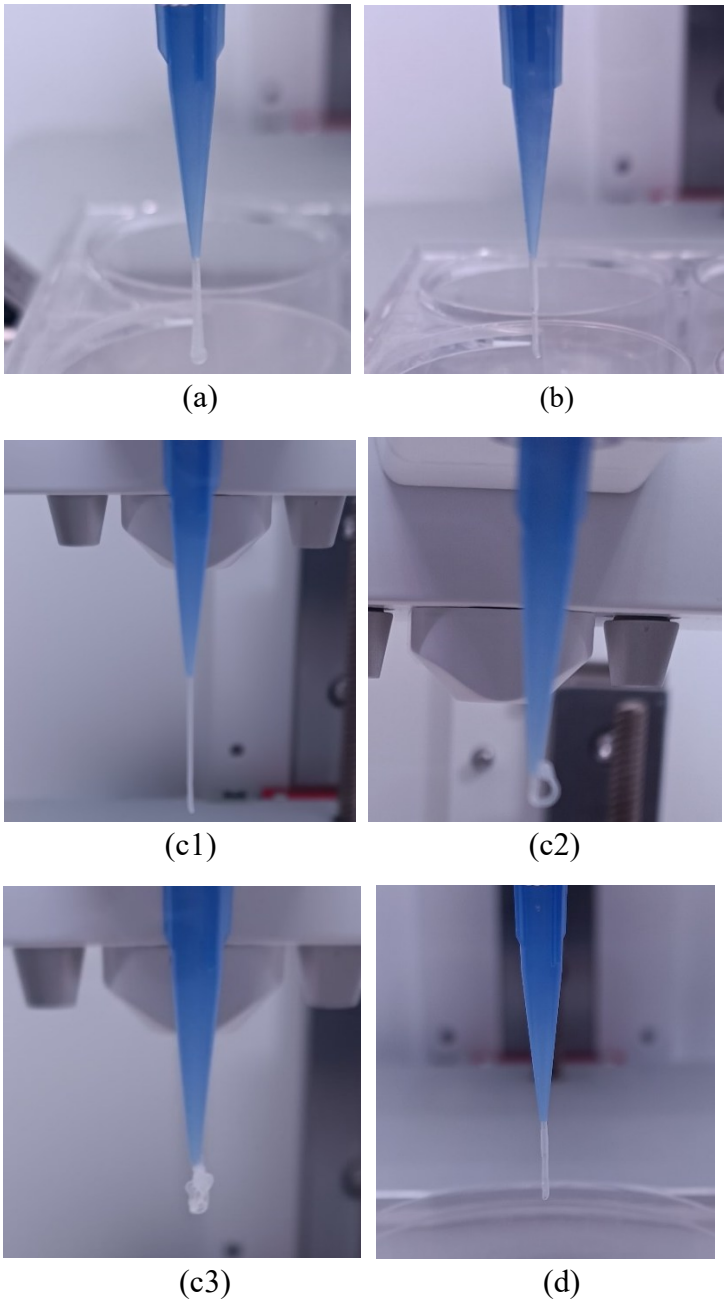

Fig. 34. Results of the test flow for (a) 2/4, (b) 2.5/4, (c1, c2, c3) 3/4 and (d) 2/5 bioinks.

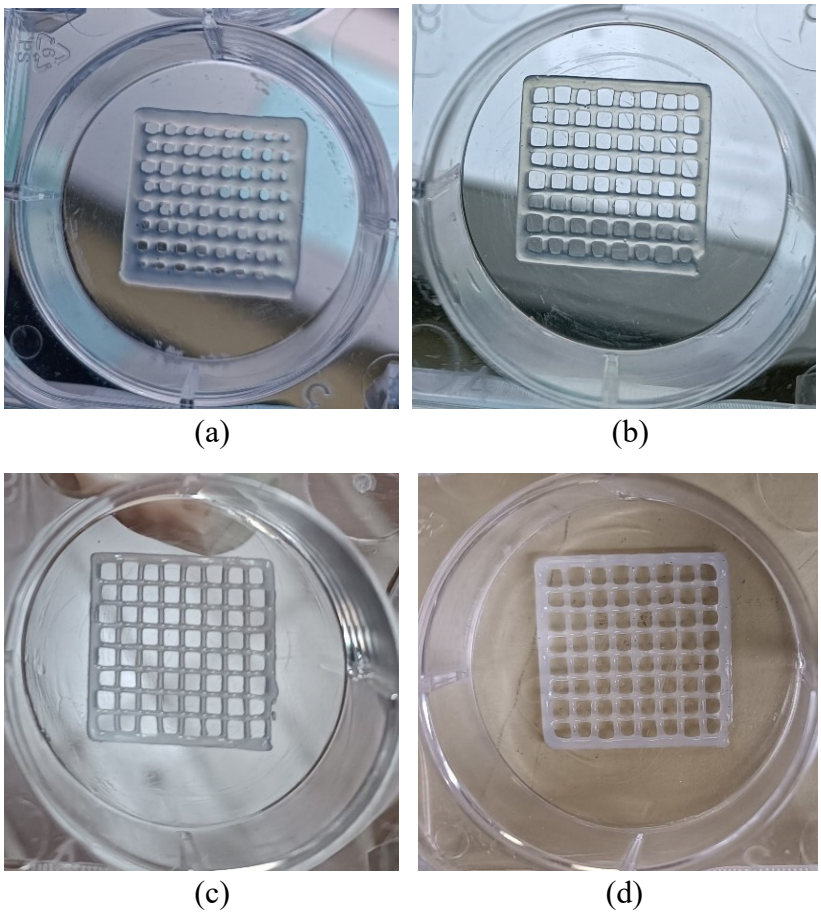

Fig. 35. Rectilinear scaffolds (20x20x1 mm, 15% infill) realized with: (a) 2/4, (b) 2.5/4, (c) 3/4 and (d) 2/5 bioinks.

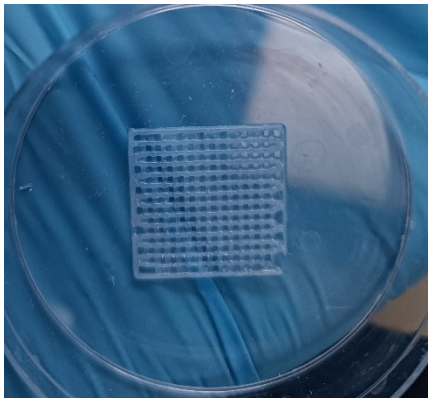

Fig. 36. Rectilinear scaffold (20x20x1 mm, 25% infill) realized with 3/4 bioink.

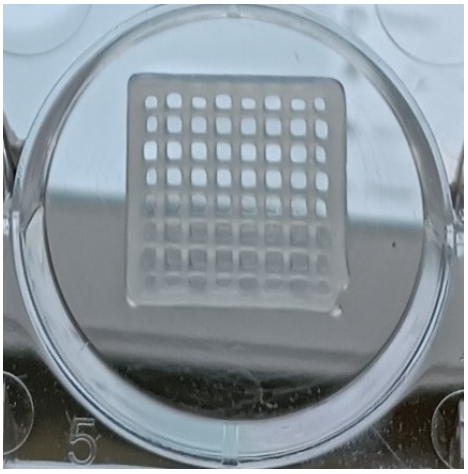

(a)

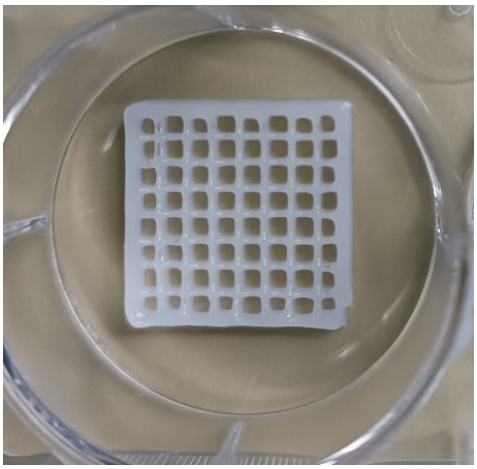

(b)

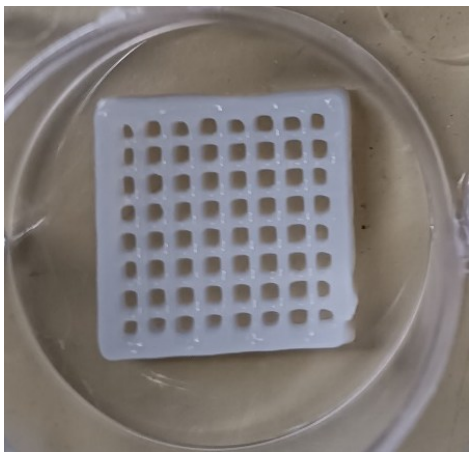

(c)

Fig. 37. Rectilinear scaffolds (20x20x3 mm, 15% infill) realized with: (a) 2.5/4, (b) 3/4 and (c) 2/5 bioinks.

Table 8. Mean dimensions (mm) of the printed rectilinear scaffolds (20x20x1 mm, 15% infill), in order 2/4, 2.5/4, 3/4 and 2/5. One scaffold per bioink was printed and the mean side width and length computed from all the 4 sides while the mean line width from a minimum of 4 lines.

	BIOINK			
DIMENSION	**2/4**	**2.5/4**	**3/4**	**2/5**
Mean line width (mm)	1.05	0.60	0.54	0.66
Mean side width (mm)	1.72	1.39	1.07	1.48
Mean side length (mm)	20.40	20.13	20.01	20.08

Table 9. Mean dimensions (mm) of the printed rectilinear scaffolds (20x20x3 mm, 15% infill), in order 2.5/4, 3/4 and 2/5. One scaffold per bioink was printed and the mean side width and length computed from all the 4 sides while the mean line width from a minimum of 4 lines and the height from a minimum of 4 random points.

	BIOINK		
DIMENSION	**2.5/4**	**3/4**	**2/5**
Mean line width (mm)	0.94	0.46	0.94
Mean side width (mm)	1.46	1.38	1.80
Mean side length (mm)	20.16	20.04	20.24
Mean height (mm)	2.91	2.97	2.63

9.2.3. Stability

In this sub-sub-chapter images describing the stability evaluation of the selected bioinks, thus 2/4, 2.5/4, 3/4 and 2/5, can be observed.

Fig. 38 and Fig. 39 describe the two types of cylinders, thus the hollow cylinder and the infilled one, made with the selected bioinks; in some cases, the instant at which the hollow cylinder failed has been reported too.

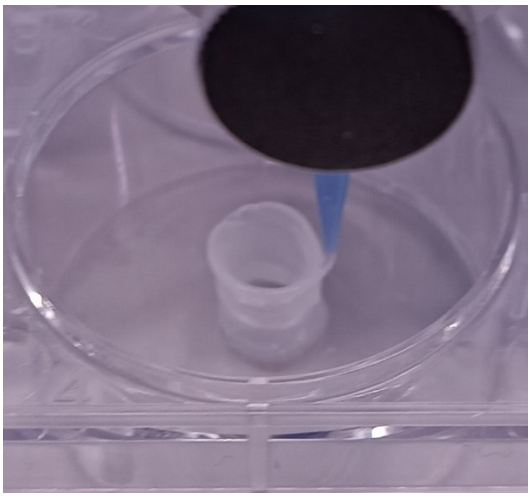

(a1)

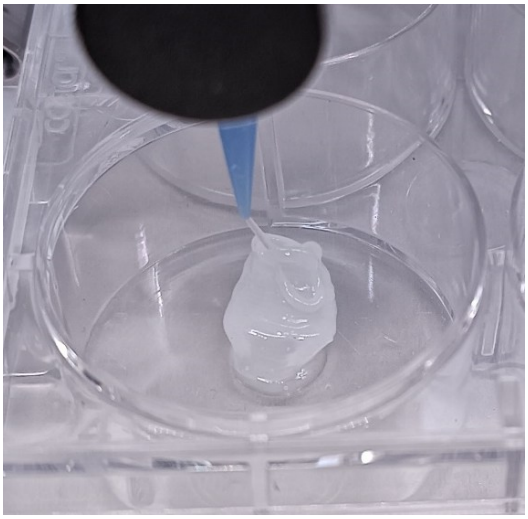

(a2)

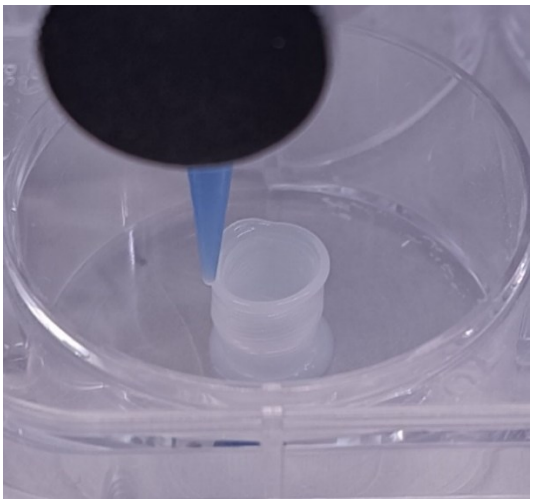

(b1)

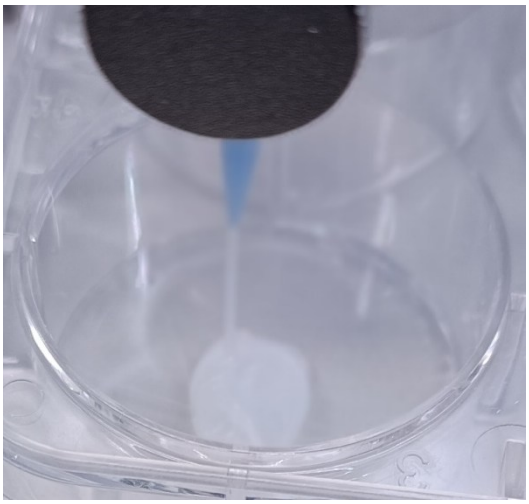

(b2)

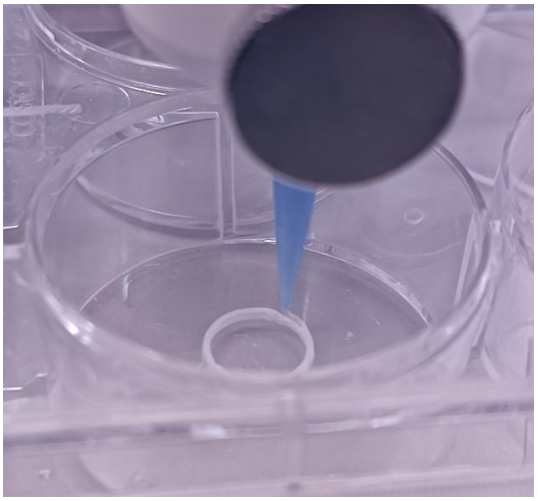

(c1)

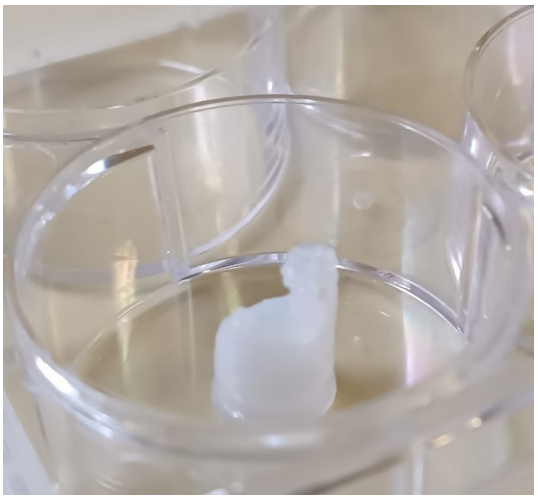

(c2)

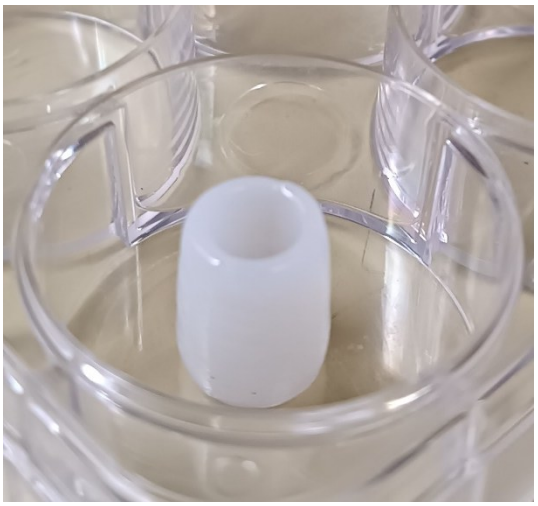

(d)

Fig. 38. Printed hollow cylinders. (a1, a2) Realization and failure of the cylinder with 2/4 bioink, (b1, b2) for 2.5/4, (c1, c2) for 3/4. (d) Hollow cylinder realized with 2/5.

(a)

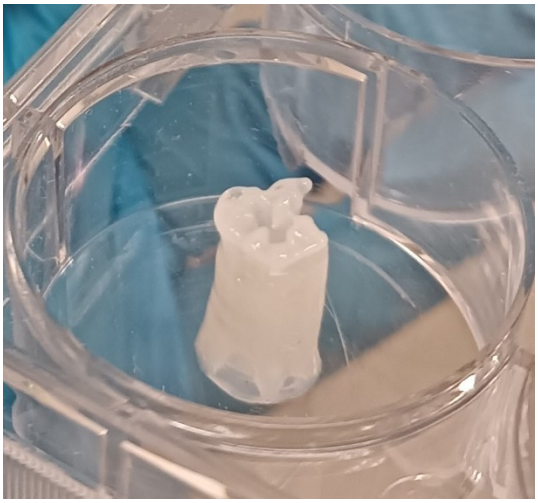

(b)

(c)

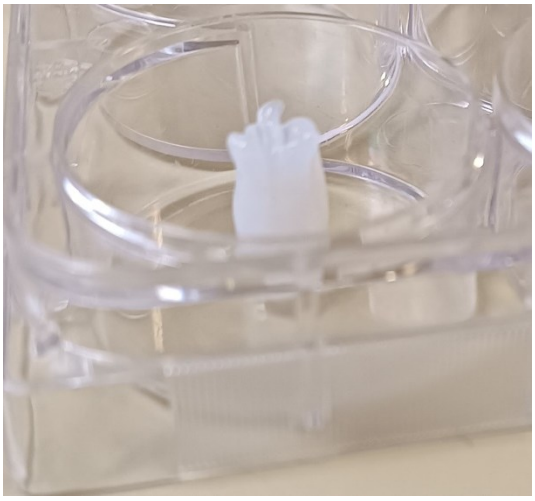

(d)

Fig. 39. Infilled cylinder realized respectively with the bioinks: (a)2/4, (b) 2.5/4, (c) 3/4 and (d) 2/5.

9.3. Bioink crosslinking effects

In this sub-chapter results obtained by changing the crosslinking procedure, the bioink crosslinked and the type of crosslinker are reported.

Results in Fig. 40 were got by using the same crosslinker, $CaCl_2$ (80 mM) solution, on the same type of bioink while changing the modality of application, from fast and randomly to slowly and gradually.

In Fig. 41, instead, can be observed the results got by using the same crosslinker, $CaCl_2$ (80 mM) solution, on the four different bioinks, respectively 2/4, 2.5/4, 3/4 and 2/5. For each bioink, the percentage deformation from the original size post-printing is graphically depicted in Fig. 42. The mean dimensions related to the line width, and the side width and length of the four scaffolds have been considered, for the computation.

While in Fig. 43 are illustrated the results obtained by using the same type of bioink, 2.5/4, but testing three different crosslinkers, exactly $CaCl_2$ (80 mM), $CaCl_2$ (80 mM) combined with $BaCl_2$ (3 mM) and $CaCl_2$ (300 mM) solutions. Additionally, in Table 10 there are the mean widths of the side for each scaffold. Thus, the table has 3 rows as many as the crosslinkers used, identified with their chemical formula and reported in the first column; the second column corresponds to the mean side width.

In Fig. 44 there the images of the bioinks 2.5/4, 3/4 and 2/5, crosslinked with $CaCl_2$ (80 mM) combined with $BaCl_2$ (3 mM) solution. For each bioink, the percentage deformation from the original size post-printing is graphically depicted in Fig. 45.

The mean dimensions related to the line width, the side width and length, and height of the three scaffolds have been considered, for the computation.

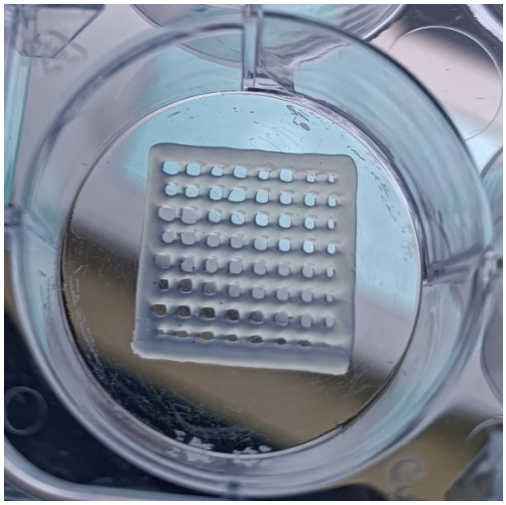

(a)

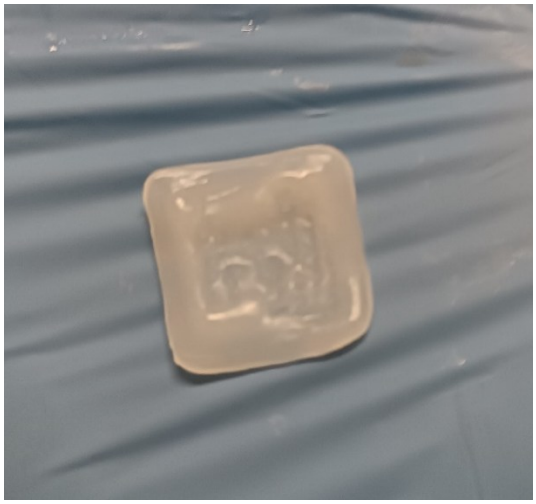

(b)

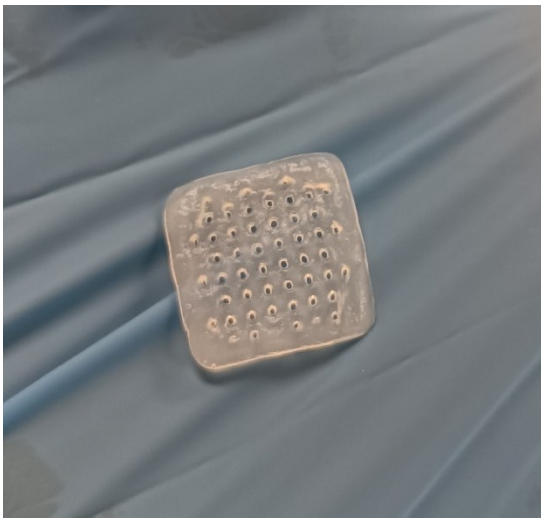

(c)

Fig. 40. Printed rectilinear scaffold (20x20x1 mm, 15% infill) made of 2/4 bioink (a), crosslinked through the same crosslinker, $CaCl_2$ (80 mM) solution, but in different ways. (b) Crosslinker provided fast and randomly while (c) slowly and gradually.

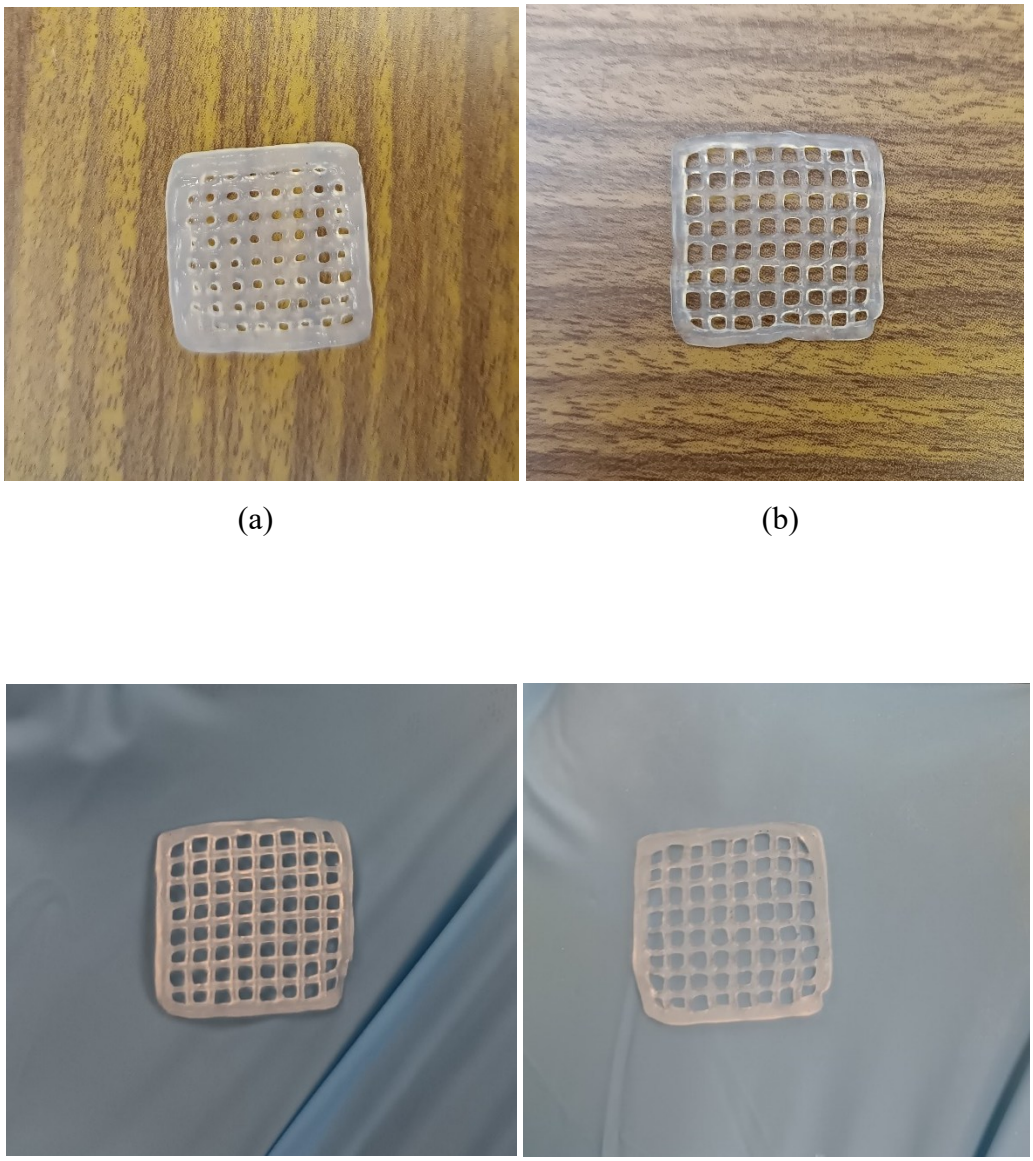

Fig. 41. Rectilinear scaffolds (20x20x1 mm, 15% infill) realized with (a) 2/4, (b) 2.5/4, (c) 3/4 and (d) 2/5 bioinks, all crosslinked with $CaCl_2$ (80 mM) solution.

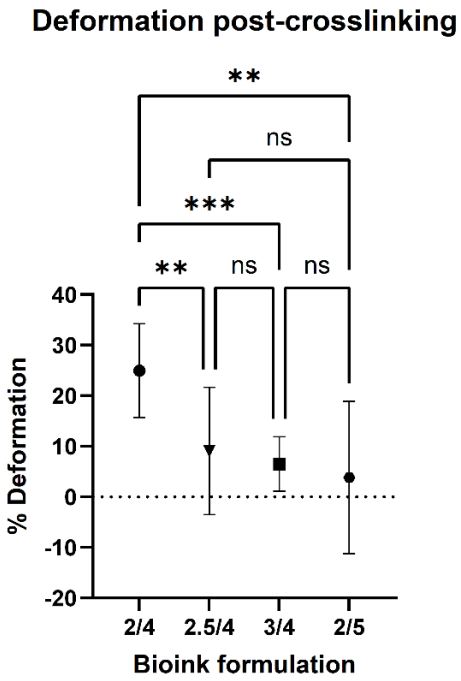

Fig. 42. Deformation of the bioinks, after printing and crosslinking with $CaCl_2$ (80 mM) solution, expressed as a percentage of the original size post-printing. The mean values were computed from the side and line of the rectilinear scaffold for each bioink: 2/4, 2.5/4, 3/4 and 2/5. They are presented with error bars depicting standard deviation (n=12). Positive values stand for shrinkage while negative ones for swelling.

Fig. 43. Three rectilinear scaffolds (20x20x3 mm, 15% infill) realized with the same bioink, 2.5/4, but crosslinked with different crosslinkers. Respectively, starting from left: $CaCl_2$ (80 mM) combined with $BaCl_2$ (3 mM), $CaCl_2$ (80 mM) and $CaCl_2$ (300 mM) solutions.

Table 10. Mean border widths (mm) of the rectilinear scaffold (20x20x3) crosslinked respectively with $CaCl_2$ (80 mM) mixed with $BaCl_2$ (3 mM), $CaCl_2$ (80 mM) and $CaCl_2$ (300 mM). One scaffold per crosslinker was printed and the mean border width computed from all the 4 sides.

	DIMENSION
CROSSLINKER	**Mean side width (mm)**
$BaCl_2$ (3 mM) + $CaCl_2$ (80 mM)	*2.12*
$CaCl_2$ (80 mM)	*2.29*
$CaCl_2$ (300 mM)	*2.70*

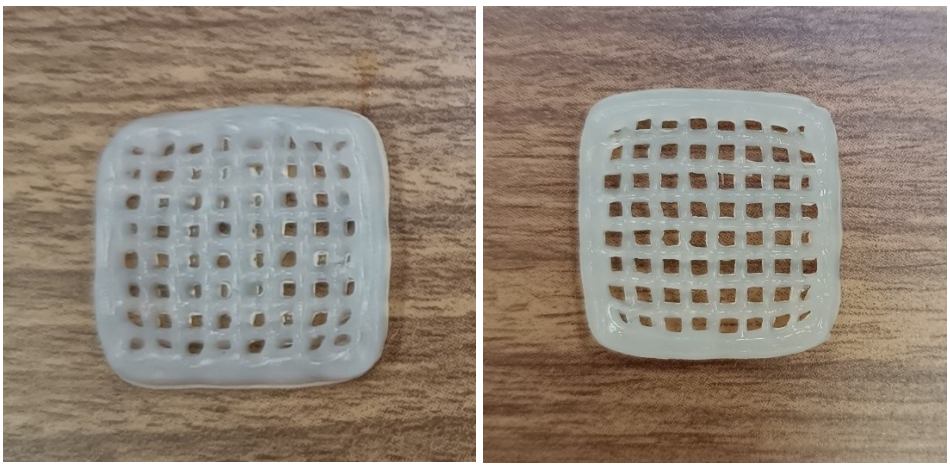

(a) (b)

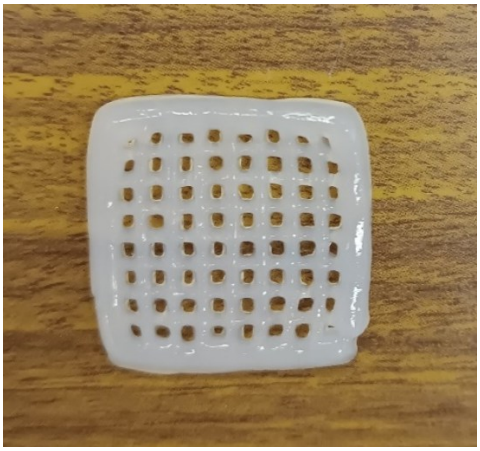

(c)

Fig. 44. Three rectilinear scaffolds (20x20x3 mm, 15% infill) realized with different bioinks and all crosslinked with $CaCl_2$ (80 mM) combined with $BaCl_2$ (3 mM) solution. In (a) the bioink is 2.5/3, in (b) 3/4 and in (c) 2/5.

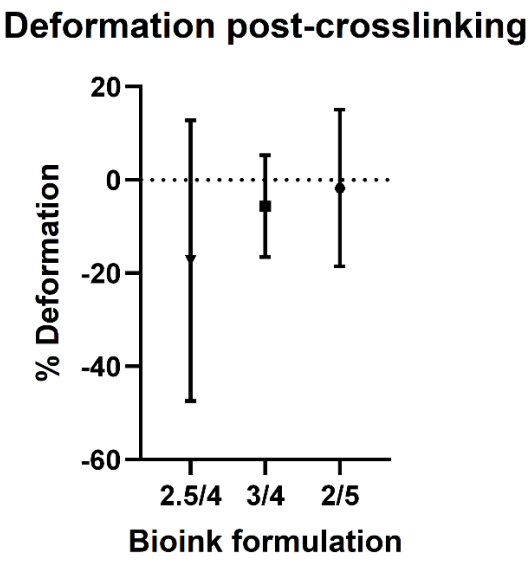

Fig. 45. Deformation of the bioinks, after printing and crosslinking with $CaCl_2$ (80 mM) mixed with $BaCl_2$ (3 mM) solution, expressed as a percentage of the original size post-printing. The mean values were computed from the side, line and height of the rectilinear scaffold (20x20x3 mm, 15% infill) for each bioink. They are presented with error bars depicting standard deviation (n=16). Positive values stand for shrinkage while negative ones for swelling. No significant differences were observed between mean percentage deformations ($p > 0.1082$).

9.4. Bioink characterization

9.4.1. Shape fidelity and shrinkage tests

In this section the results obtained from the shape fidelity and the shrinkage tests on the selected bioinks are shown with tables.

Table 11 contains the mean grid areas of the three printed bioinks, compared to the intended one. Thus, the rows represent the grid areas of the model and of the printed scaffolds respectively, while the columns are the four bioinks. For each bioink, the mean grid area and the standard deviation are graphically depicted in Fig. 46.

The percentage shrinkage from the size post-crosslinking, with $CaCl_2$ (80 mM) solution, is graphically depicted for each bioink in Fig. 47. For the results the mean dimensions related to the line width, and the side width and length of the four scaffolds have been considered.

Table 11. Mean grid areas (mm^2) of the printed grid scaffolds (20x20x1 mm, 15% infill), in order 2/4, 2.5/4, 3/4 and 2/5, compared to the intended one. One scaffold per bioink was printed and the mean grid area computed from a minimum of 6 grids. The ranges and deviations from the intended grid area are also presented in the table.

	BIOINK			
GRID AREA	**2/4**	**2.5/4**	**3/4**	**2/5**
Intended grid area (mm^2)	16	16	16	16
Mean grid area (mm^2)	8.92	14.92	15.12	10.32
Range of grid areas (mm^2)	0.37	0.42	0.78	1.05
Mean area discrepancy (mm^2)	7.08	1.08	0.88	5.68

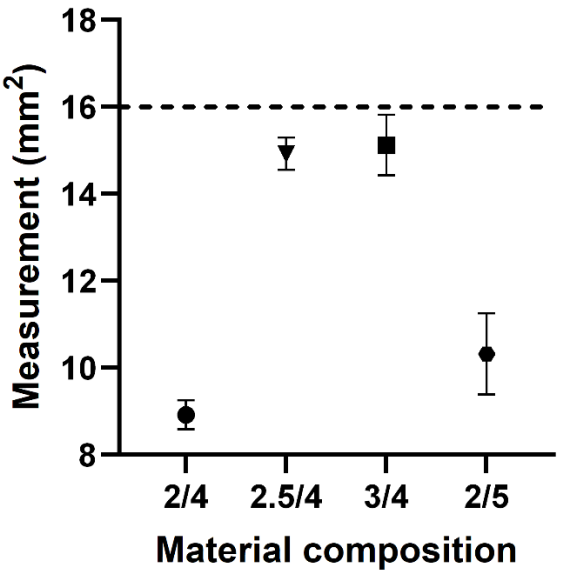

Fig. 46. Graphical representation of the mean grid areas computed from a minimum of 6 grids for each bioink: 2/4, 2.5/4, 3/4 and 2/5. Standard deviation is also depicted. A dotted horizontal line represents the intended grid area of 16 mm² reference.

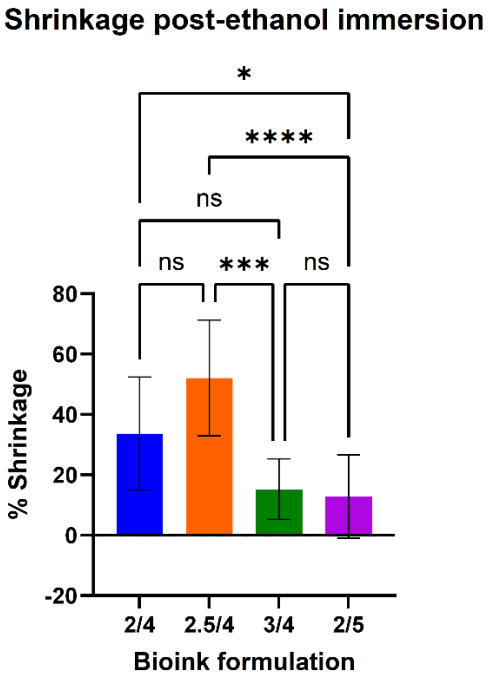

Fig. 47. Shrinkage of the bioinks, after crosslinking with $CaCl_2$ (80 mM) and immersion in ethanol, expressed as a percentage of the original size post-crosslinking. The mean values were taken from the side and line of the rectilinear scaffold for each bioink: 2/4 (blue), 2.5/4 (orange), 3/4 (green) and 2/5 (purple). They are presented with error bars depicting standard deviation (n=12).

9.4.2. Swelling test

In this section results of the swelling test, with the scaffolds immersed in distilled water and in culture medium respectively, for the selected bioinks, are reported.

Swelling in water

In Table 12 are reported the weights of the scaffolds, realized respectively with 2/4, 2.5/4 and 3/4 bioinks, at fixed time points, from the starting point, time 0, which the dried weight corresponds to, to the end point, 72 h. There are as many rows as the time points which are in the first column; follow three columns identified with the three bioinks: 2/4, 2.5/4 and 3/4.

The swelling ratios obtained through eq. (8) are graphically represented in Fig. 48. In this figure there is a line graph with indicators, where on the x-axis there are the fixed time points while on the y-axis the swelling ratios respectively for the three bioinks.

Table 12. The table has 11 rows as many as the fixed time points, from 0 to 72 h, that contain the weights (g) assumed by the three bioinks, 2/4, 2.5/4 and 3/4, during water immersion.

Time	2/4 (g)	2.5/4 (g)	3/4 (g)
0 min	0.01444	0.00723	0.03725
5 min	0.02796	0.01486	0.05829
10 min	0.03094	0.01413	0.06085
15 min	0.03088	0.01544	0.06364
30 min	0.03142	0.0146	0.06464
45 min	0.03309	0.01619	0.06544
1 h	0.03333	0.01714	0.06762
1 h 30 min	0.03473	0.0167	0.0689
24 h	0.03405	0.0155	0.07118
48 h	0.03533	0.01753	0.07517
72 h	0.03327	0.01861	0.07424

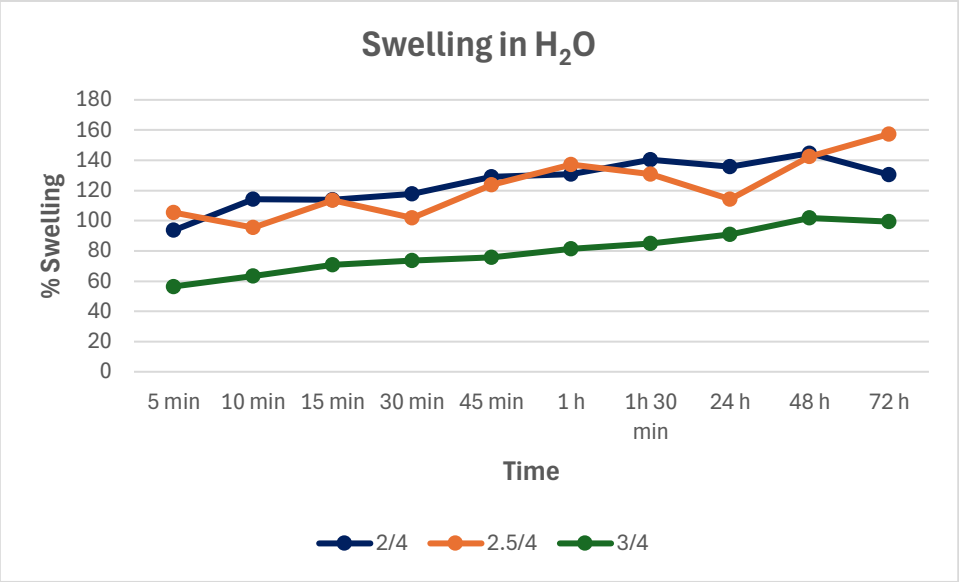

Fig. 48. In the graph on the x-axis there are the fixed time points while on the y-axis the percentage swelling ratios. Three curves can be observed with indicators at each time point, indicating the swelling ratios of three bioinks, respectively 2/4 (blue), 2.5 (orange) and 3/4 (green).

Swelling in culture medium

Results are shown like those for swelling in water, but with the addition of 2/5 bioink.

Weights are contained in Table 13 and the graph with the swelling ratios versus time, for all the four bioinks crosslinked with $CaCl_2$ (80 mM) solution, is illustrated in Fig. 49.

While Table 14 contains the weights for 3/4 bioink crosslinked with $CaCl_2$ (80 mM) mixed with $BaCl_2$ (3 mM) solution, and Fig. 50 compares the swelling ratios versus time of 3/4 bioink crosslinked with $CaCl_2$ solution and the mixed solution.

Fig. 51 shows 2.5/4 scaffold post-crosslinking with $CaCl_2$ (80 mM) solution, post-drying and 5 min, 1 h, 1 day and 3 days after swelling in culture medium respectively. In Fig. 52, instead, there are the same images but for 2/5 bioink and in Fig. 53 for 3/4 crosslinked with $CaCl_2$ mixed with $BaCl_2$ solution. Whereas Fig. 54 shows 3/4 scaffold post-crosslinking with $CaCl_2$ solution, post-drying and 5 min and 1 h after swelling in culture medium.

Table 13. The table has 11 rows as many as the fixed time points, from 0 to 72 h, that contain the weights (g) assumed by the four bioinks, 2/4, 2.5/4, 3/4 and 2/5, during immersion in culture medium.

Time	2/4 (g)	2.5/4 (g)	3/4 (g)	2/5 (g)
0 min	0.03244	0.02124	0.01807	0.01301
5 min	0.06864	0.04185	0.03912	0.03157
10 min	0.09331	0.05848	0.05625	0.03774
15 min	0.11243	0.074	0.07982	0.04752
30 min	0.15234	0.10113	0.11175	0.06328
45 min	0.17704	0.12704	0.13675	0.07789
1 h	0.20107	0.13862	0.14885	0.08281
1 h 30 min	0.22219	0.15095	0.16536	0.09826
2 h	0.24428	0.16094	0.17396	0.1026
24 h	0.27314	0.17834	0.20525	0.11537
48 h	0.33144	0.18638	0.22554	0.11134
72 h	0.32876	0.184	0.23234	0.11259

Table 14. The table has 11 rows as many as the fixed time points, from 0 to 72 h, that contain the weights (g) assumed by 3/4 bioink, crosslinked with $CaCl_2$ (80 mM) mixed with $BaCl_2$ (3 mM) solution, during immersion in culture medium.

Time	3/4 (g)
0 min	0.01906
5 min	0.03413
10 min	0.05316
15 min	0.06037
30 min	0.08153
45 min	0.09243
1 h	0.10745
1 h 30 min	0.1063
2 h	0.10652
24 h	0.13131
48 h	0.11558
72 h	0.11608

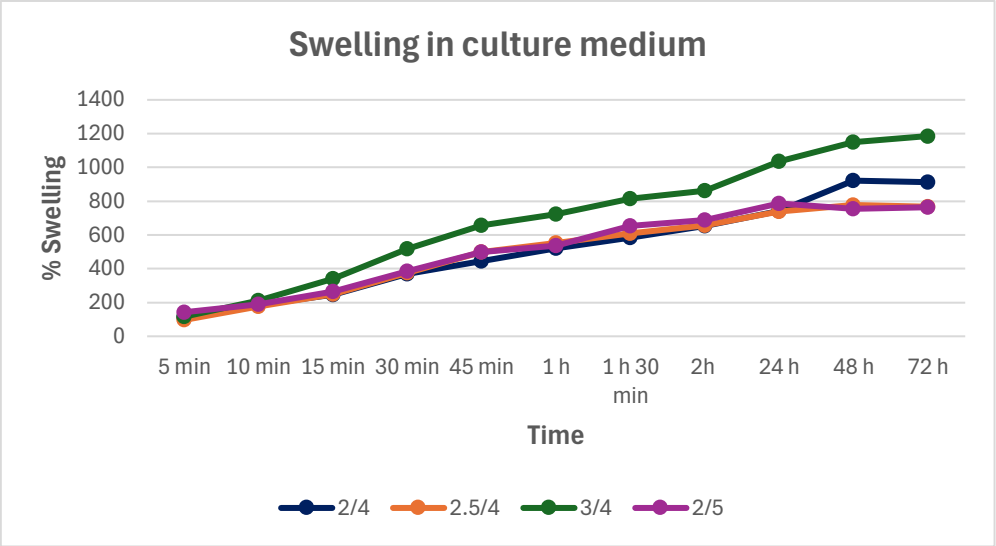

Fig. 49. In the graph on the x-axis there are the fixed time points while on the y-axis the swelling ratios. Four curves can be observed with indicators at each time point, indicating the swelling ratios of the four bioinks, respectively 2/4 (blue), 2.5 (orange), 3/4 (green) and 2/5 (purple).

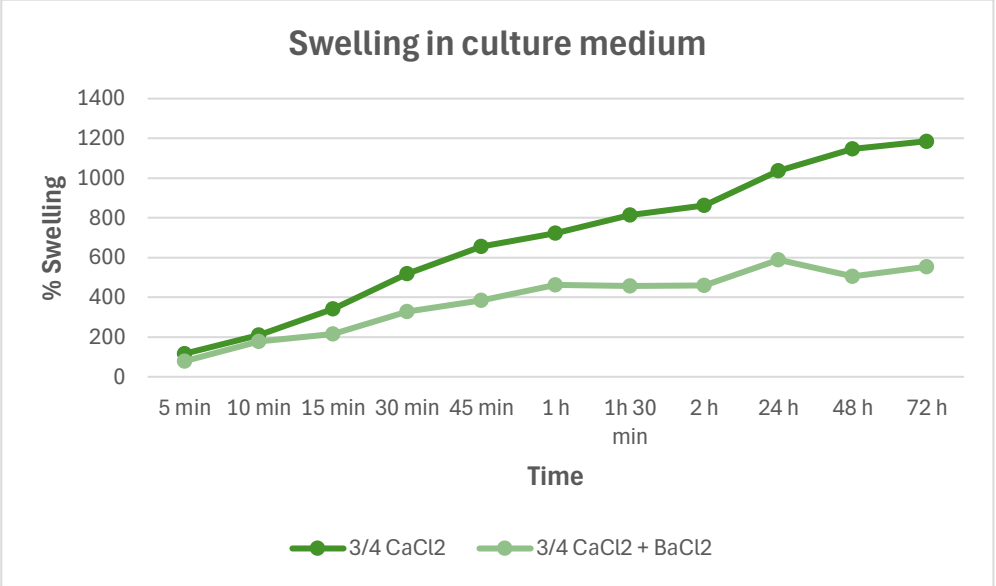

Fig. 50. The graph compares the swelling ratios versus time of 3/4 bioink crosslinked with $CaCl_2$ (80 mM) solution and the same bioink crosslinked with $CaCl_2$ (80 mM) mixed with $BaCl_2$ (3 mM) solution. The first one is represented in green while the second in light green respectively.

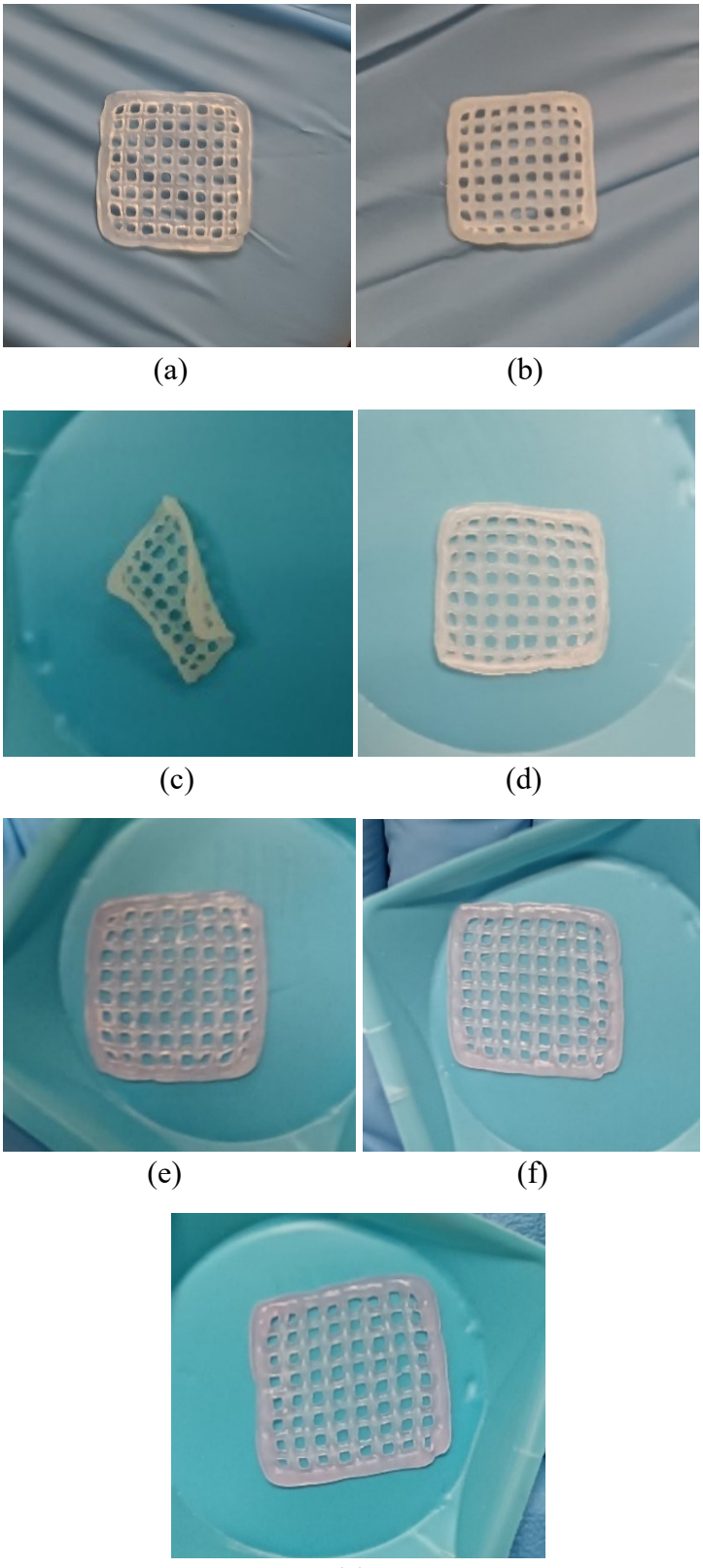

Fig. 51. Rectilinear scaffold (20x20x1 mm, 15% infill) realized with 2.5/4 bioink. (a) Post-crosslinking with $CaCl_2$ (80 mM) solution, (b) after ethanol immersion, (c) after air-drying and during immersion in culture medium, respectively (d) 5 min, (e) 1 h, (f) 1 day and (g) 3 days after.

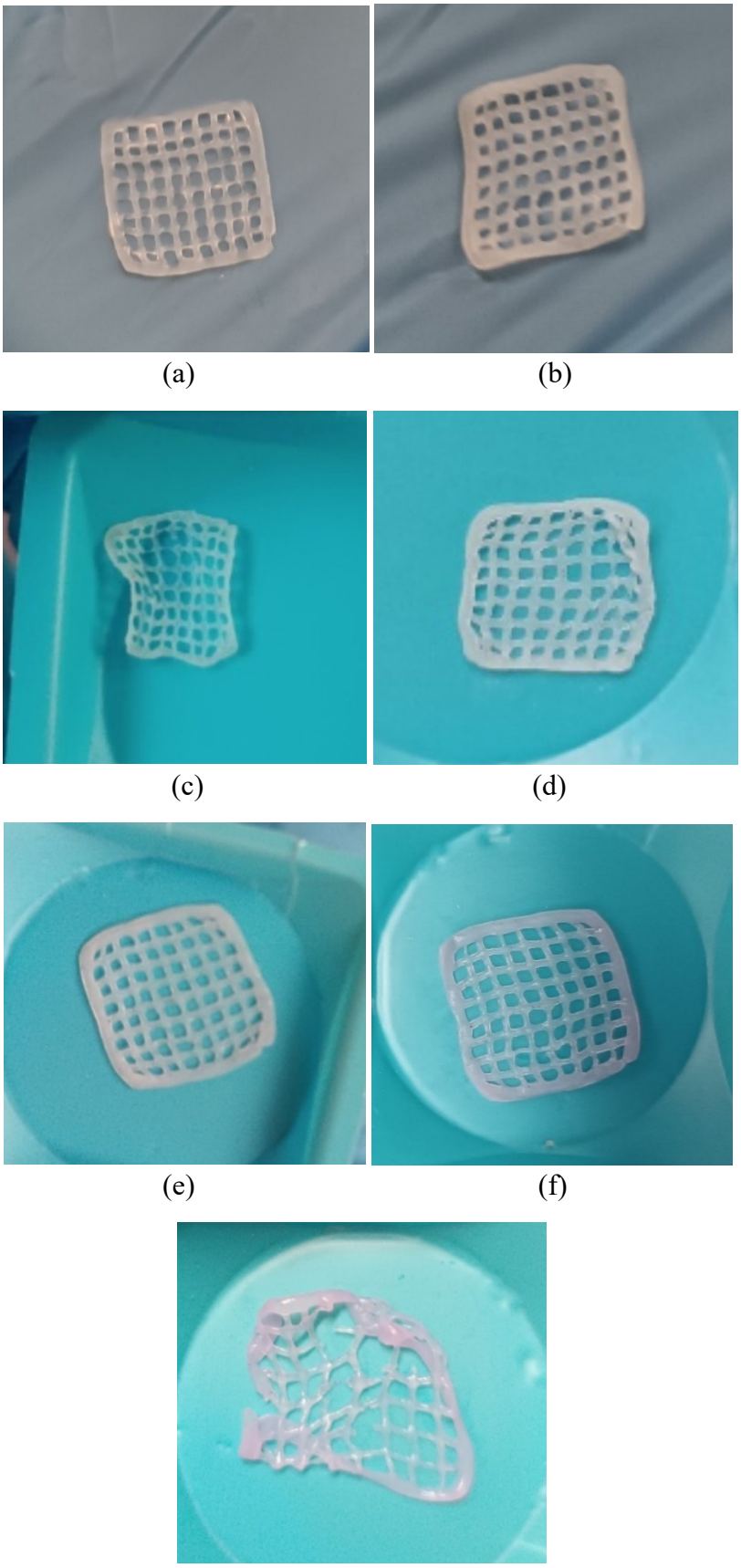

Fig. 52. Rectilinear scaffold (20x20x1 mm, 15% infill) realized with 2/5 bioink. (a) Post-crosslinking with $CaCl_2$ (80 mM) solution, (b) after ethanol immersion, (c) after air-drying and during immersion in culture medium, respectively (d) 5 min, (e) 1 h, (f) 1 day and (g) 3 days after.

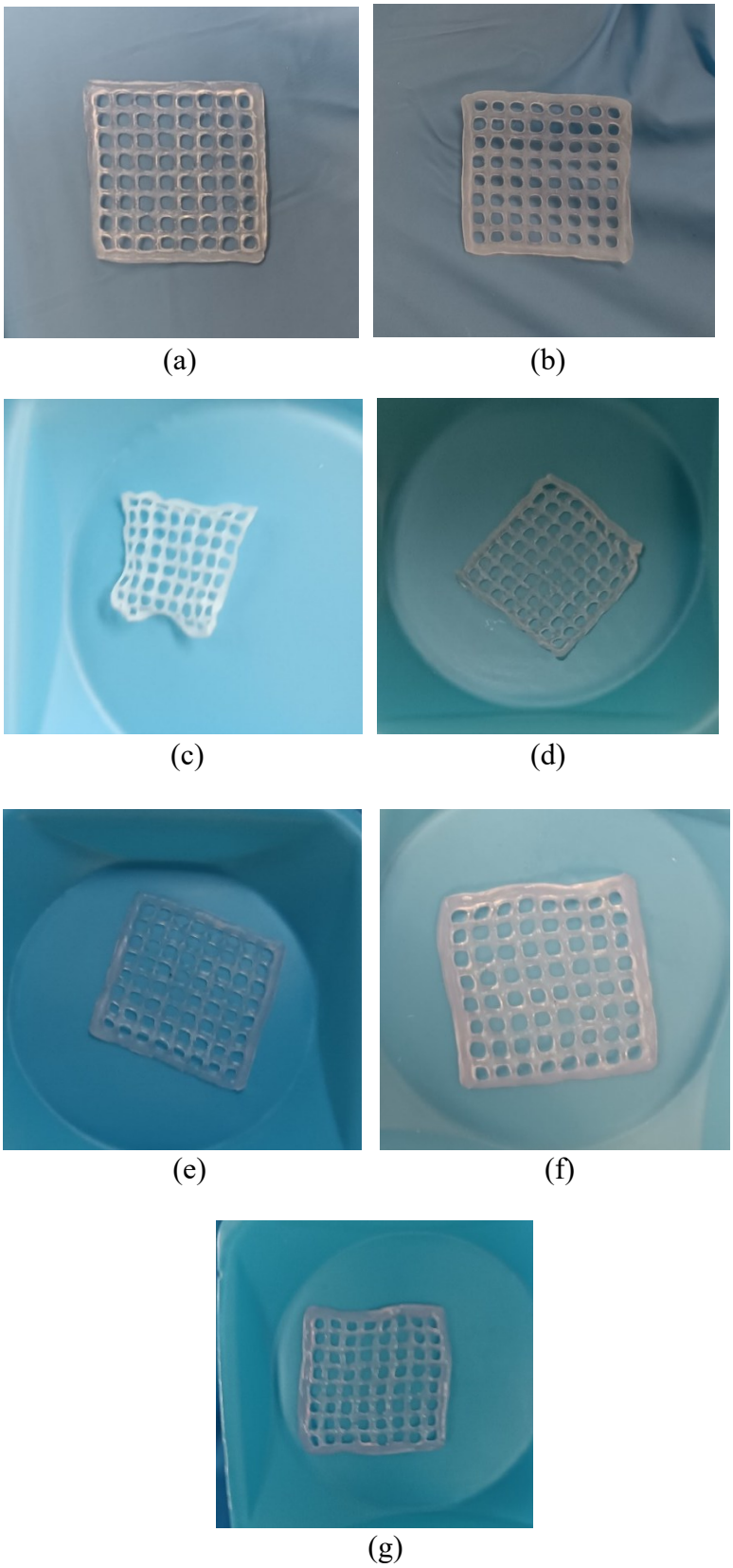

Fig. 53. Rectilinear scaffold (20x20x1 mm, 15% infill) realized with 3/4 bioink. (a) Post-crosslinking with $CaCl_2$ (80 mM) mixed with $BaCl_2$ (3 mM) solution, (b) after ethanol immersion, (c) after air-drying and during immersion in culture medium, respectively (d) 5 min, (e) 1 h, (f) 1 day and (g) 3 days after.

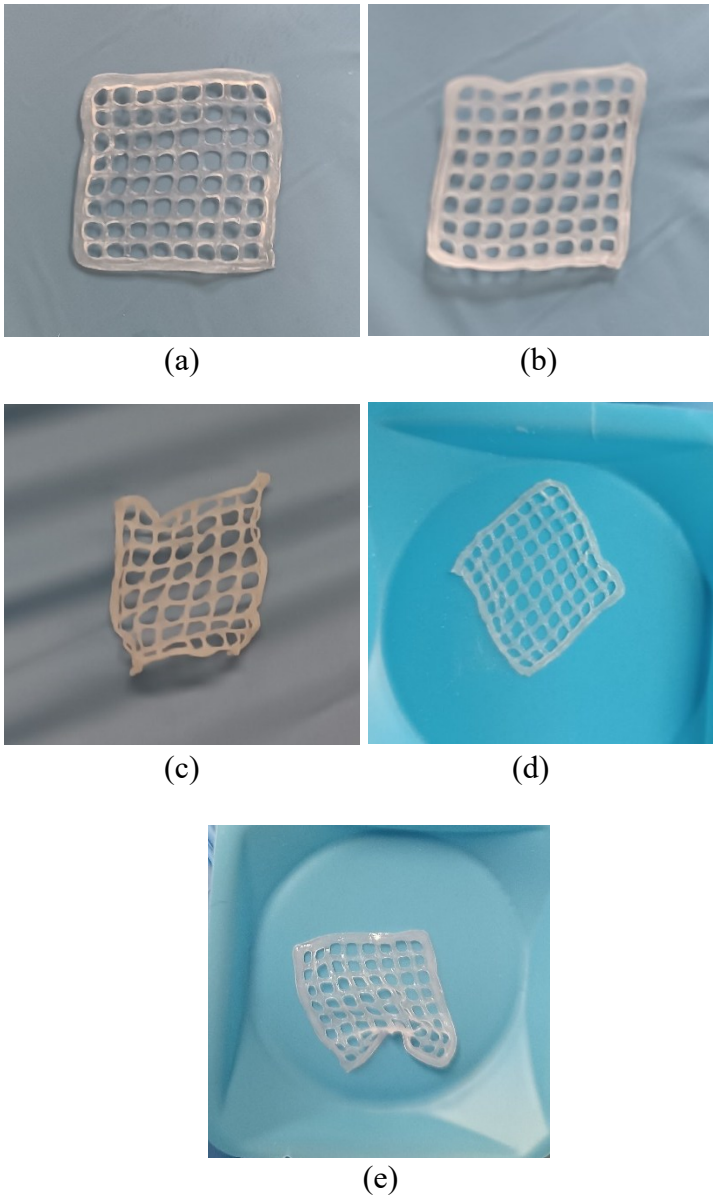

Fig. 54. Rectilinear scaffold (20x20x1 mm, 15% infill) realized with 3/4 bioink. (a) Post-crosslinking with $CaCl_2$ (80 mM) solution, (b) after ethanol immersion, (c) after air-drying and during immersion in culture medium, respectively (d) 5 min and (e) 1 h after.

9.4.3. Degradation and gel release tests

In this sub-sub-chapter the results from the degradation test, performed on the four selected bioinks, are illustrated.

Data collected during the degradation test performed at room temperature are shown in Table 15. The table contains the dried weights of the four printed and crosslinked, with $CaCl_2$ (80 mM) solution, scaffolds, realized with 2/4, 2.5/4, 3/4 and 2/5 bioinks, before immersion in culture medium, and 7 and 14 days after. Thus, the table has 4 rows as many as the bioinks, identified with the formulations and reported in the first column; follow three other columns

containing the dried weights at 0^{th}, 7^{th} and 14^{th} days respectively. 2/5 was the only formulation subjected to gel release (41.32 %).

While 3/4 scaffold at 37 °C released only 38.45 % of gel, having a dried weight of 0.36721 g before immersion in culture medium and of 0.22600 g 7 days after immersion in culture medium. In Fig. 55 it is possible to observe the scaffold after crosslinking, and 7 days after immersion in culture medium, while subjected to tensile stress too.

Table 15. The table has 4 rows, named as the bioink formulations, that contain the dried weights (g) assumed by 2/4, 2.5/4, 3/4 and 2/5 scaffolds respectively, before immersion in culture medium, and 7 and 14 days after.

	WEIGHT (g)		
BIOINK	**Day 0**	**Day 7^{th}**	**Day 14^{th}**
2/4	0.01866	0.01944	0.01874
2.5/4	0.01912	0.01749	/
3/4	0.01373	0.01628	0.01466
2/5	0.03754	0.02203	0.01945

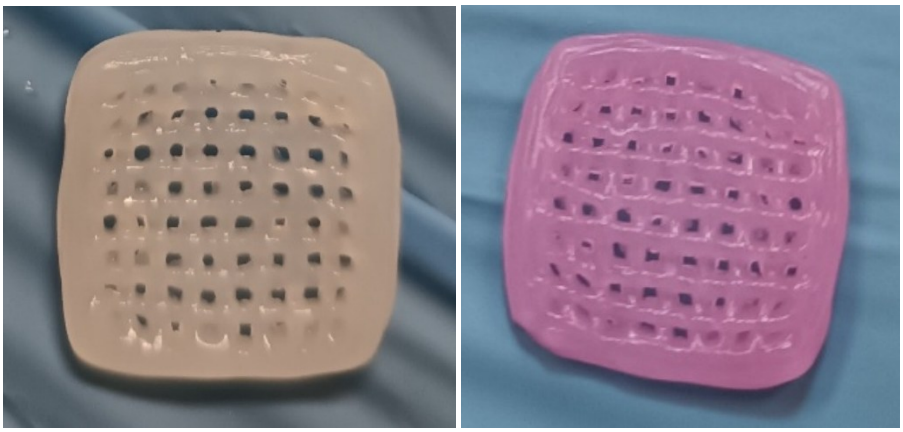

(a) (b)

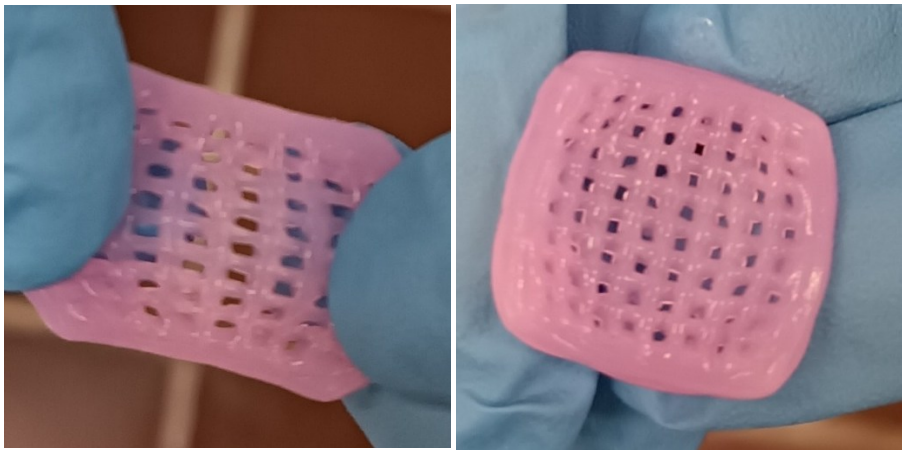

(c) (d)

Fig. 55. Degradation test for 3/4 scaffold at 37°. (a) Scaffold after crosslinking with $CaCl_2$ (80 mM), (b) 7 days after immersion in culture medium, (c) under applied tensile stress and (d) after the stress have been removed.

9.5. External ear reconstruction

The auricle reconstructed through laser scanner is illustrated in Fig. 56. Fig. 57 illustrates the ear model available on the bioprinter without, and with pattern and infill set. While in Fig. 58 there are the auricle structure post-printing and post-crosslinking with the mixed solution.

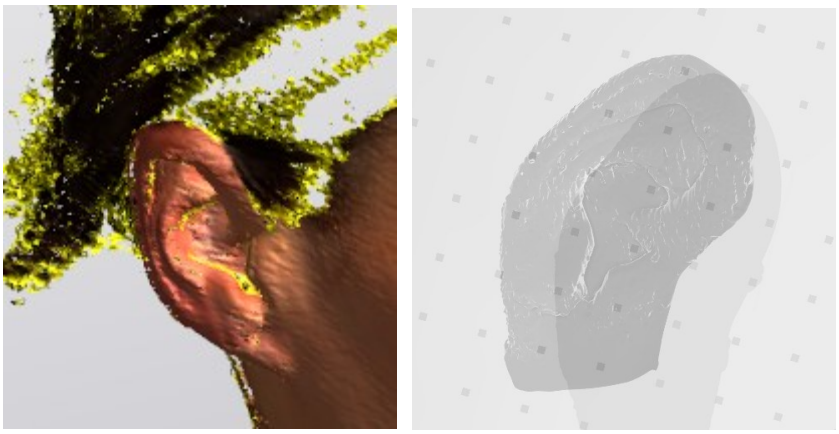

(a) (b)

(c)

Fig. 56. Ear model reconstruction attempts through laser scanner. (a) Acquired image of a human ear, (b) front and (c) back view of the a-posteriori auricular CAD model.

(a)

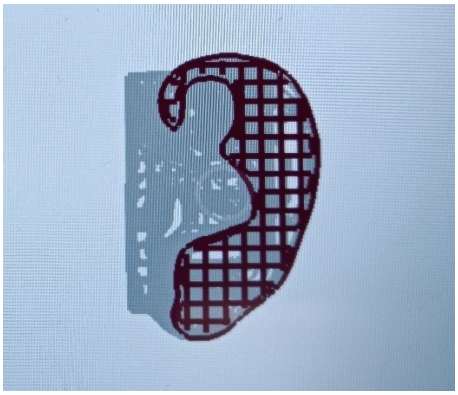

(b)

Fig. 57. (a) Auricular CAD model (Cellink, 20.43x31.50x11.10 mm) and (b) the ear model with grid pattern and 35 % infill.

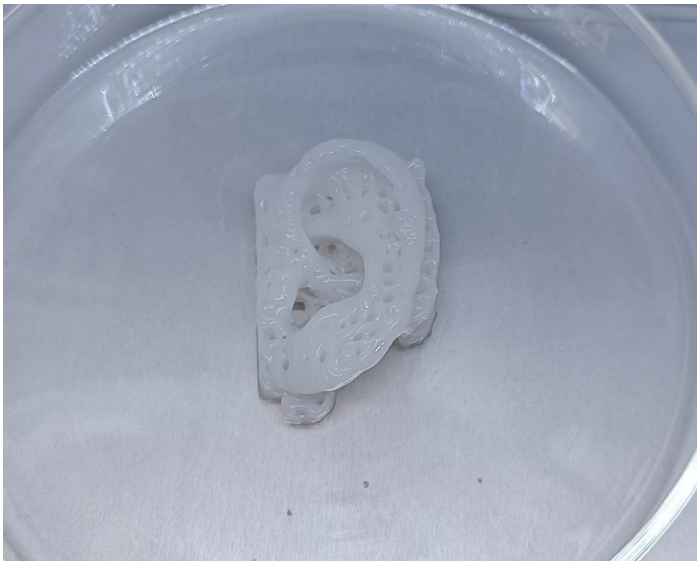

(a)

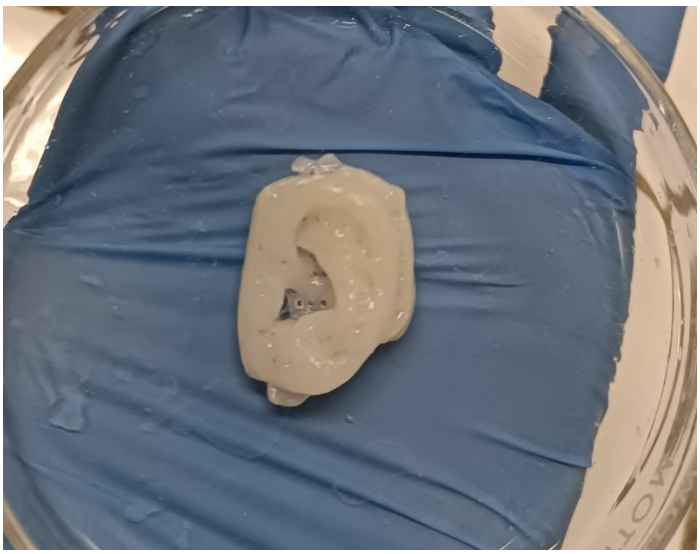

(b)

Fig. 58. Auricular structure post-printing (a) and post-crosslinking with $CaCl_2$ (80 mM) mixed with $BaCl_2$ (3 mM) solution.

9.6. Cell-laden bioink characterization

This section is related to the results of the microscopy analysis performed on the cell-laden scaffolds 7 days after immersion in culture medium in incubator (Fig. 59).

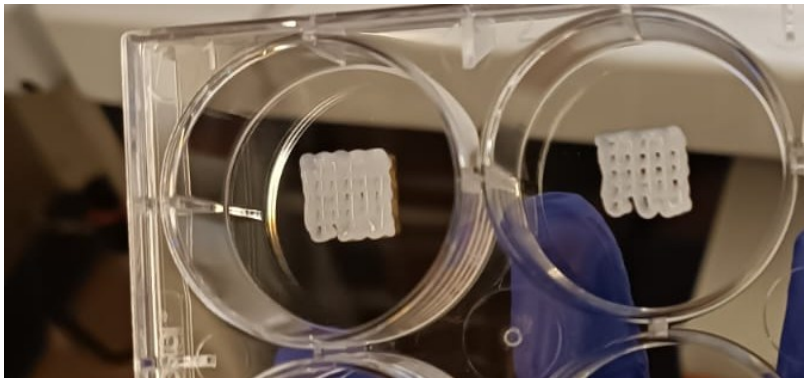

(a)

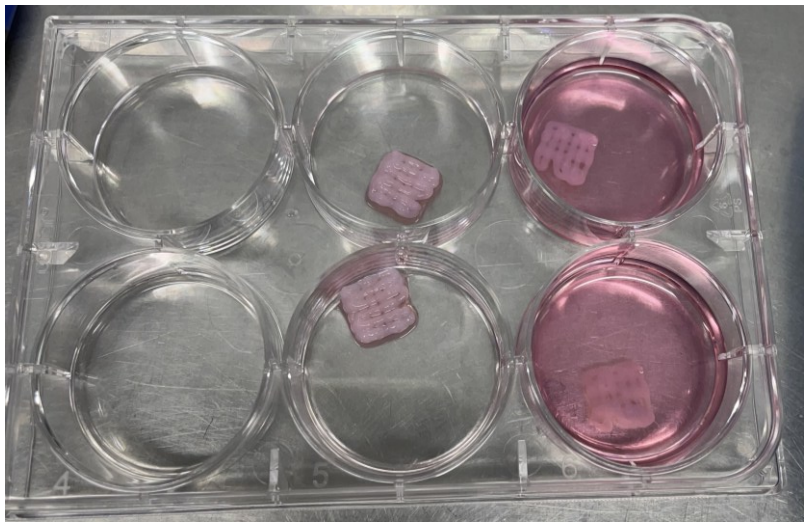

(b)

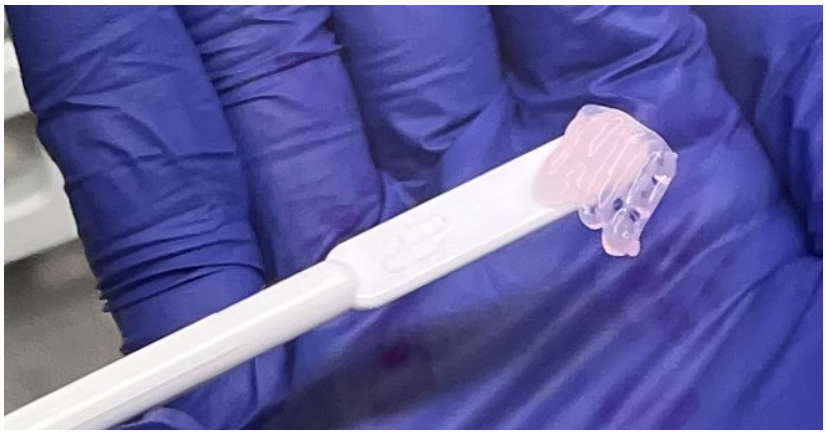

(c)

Fig. 59. Fibroblast-laden CNC-based scaffolds post-printing and crosslinking (a) and 7 days after immersion in culture medium (37°,5% CO2) (b, c).

9.6.1. Optical microscopy

Fig. 60 and Fig. 61 show the results of the optical microscopy analysis 1 day and 6 days after immersion in culture medium. While Fig. 62 illustrates the images taken during the analysis conducted using H&S, 7 days after the culture.

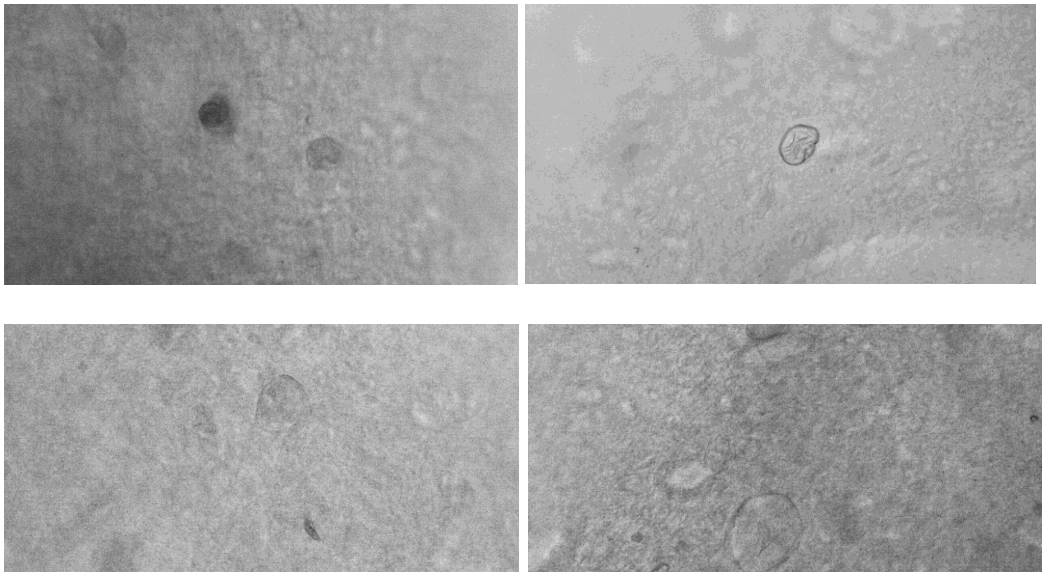

Fig. 60. Optical microscope photographs (x20 objective) of CNC-based scaffold with fibroblasts after 1 day of culture.

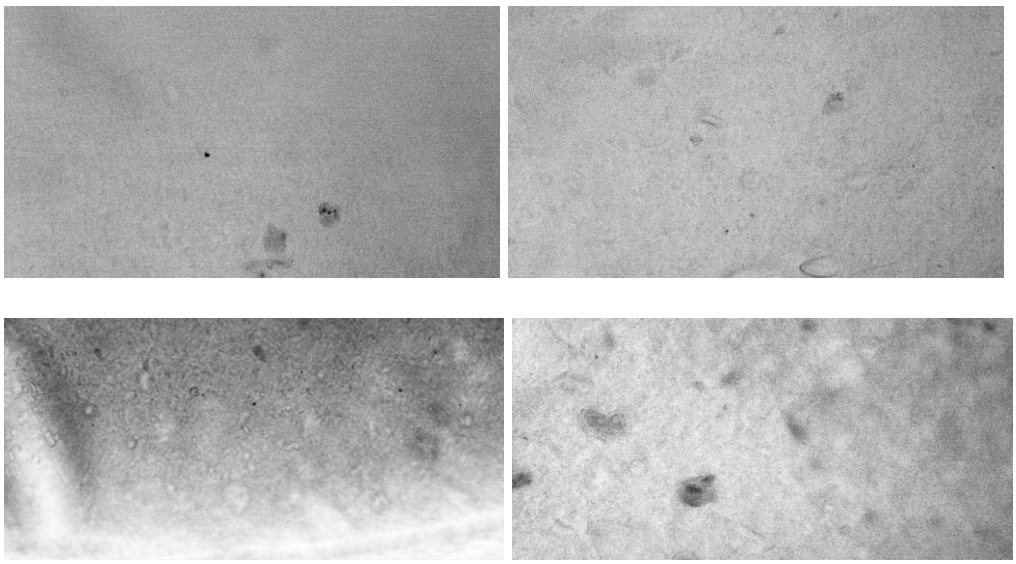

Fig. 61. Optical microscope photographs (x20 objective) of CNC-based scaffold with fibroblasts after 6 days of culture.

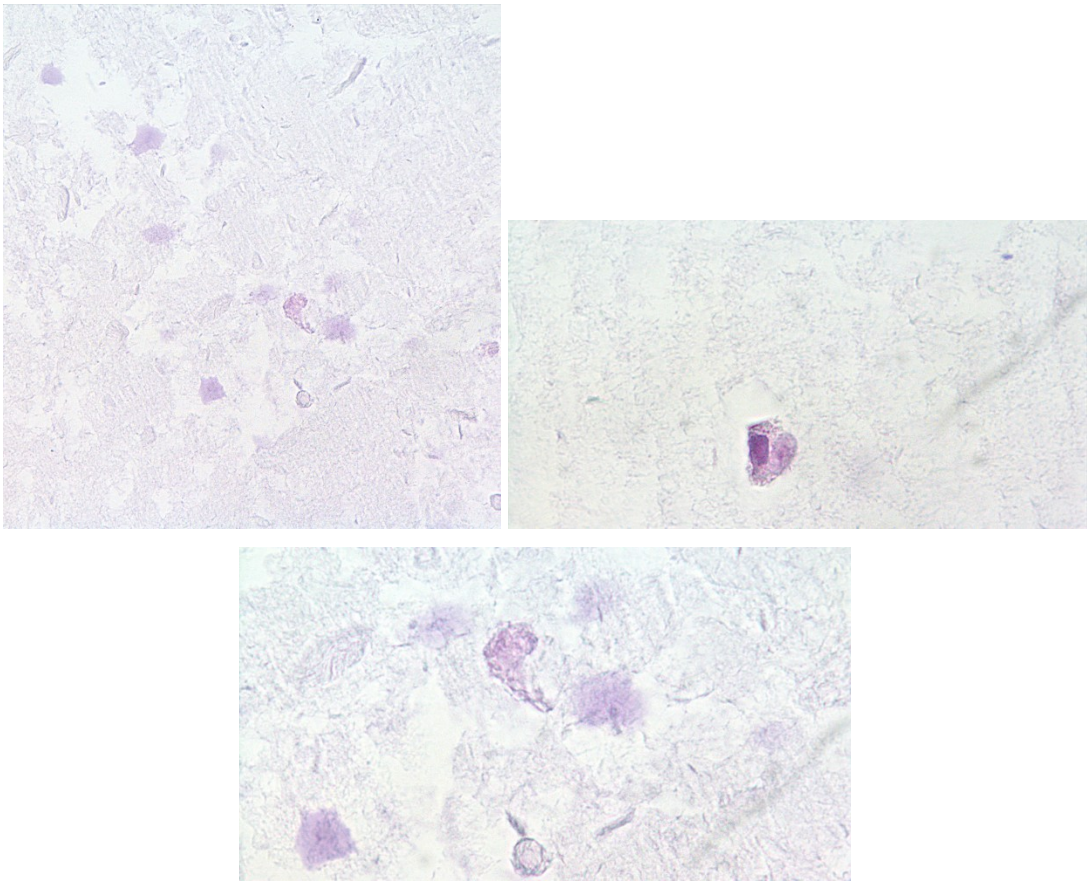

Fig. 62. H&S images (x100 objective) of CNC-based scaffold with fibroblasts after 7 days of culture.

9.6.2. Fluorescence microscopy

Results of the further cell growth analysis through DAPI staining are reported in Fig. 63.

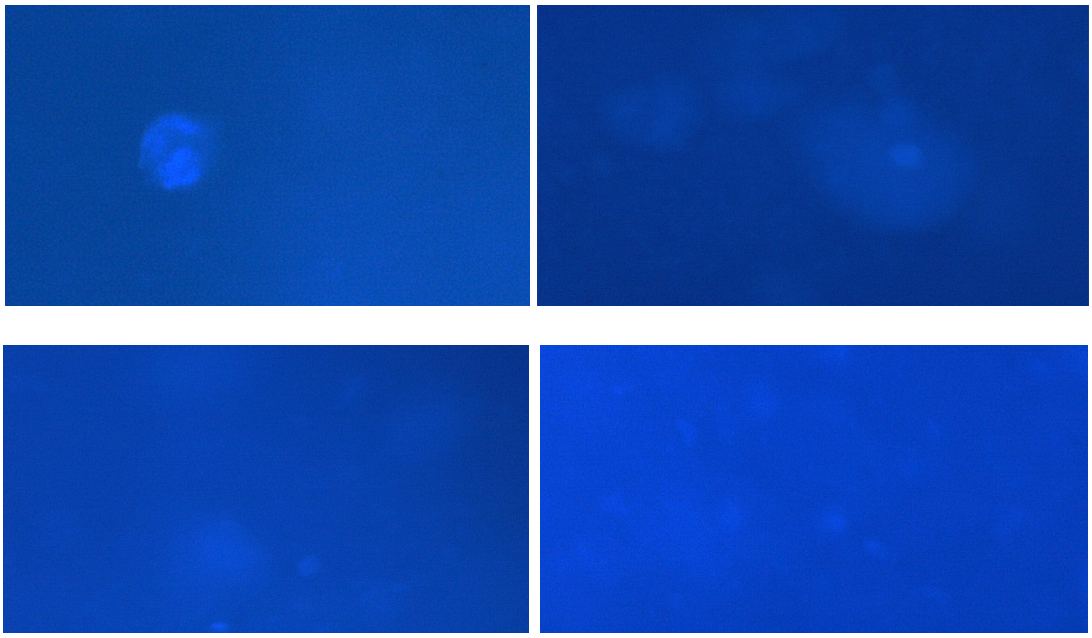

Fig. 63. Images of the spheroid' nuclei with DAPI staining. The images were taken 7 days after the culture.

9.6.3. Field Emission Scanning Electron Microscopy

In this section are reported the results obtained from SEM analysis. Images in Fig. 64 are related to the CNC-based scaffold without cells highlighting the microstructure of the lattice while images in Fig. 65 refer to the scaffold with cell suspension.

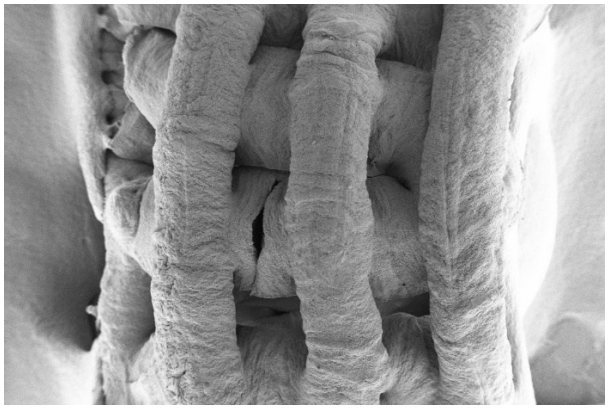

(a)

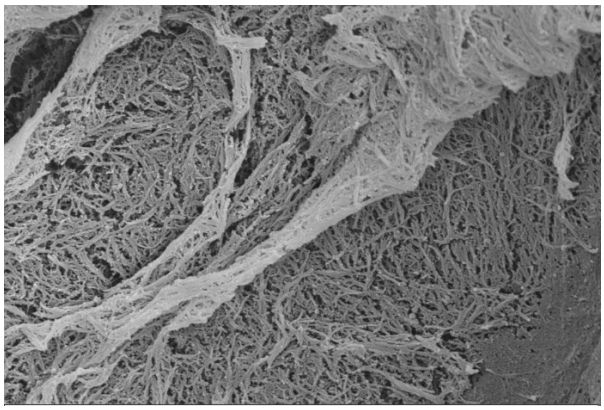

(b)

Fig. 64. SEM photographs of CNC-based scaffold without cells. (a) Lattice microstructure at low magnification (x75). Scale bar is 200 µm. (b) Lattice microstructure at high magnification (x51.68 K). Scale bar is 200 nm.

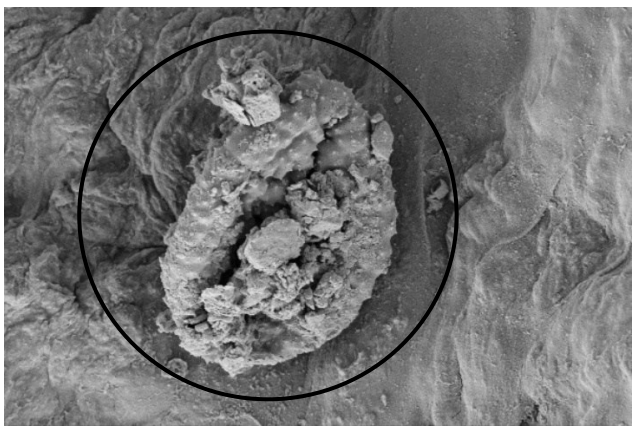

(a)

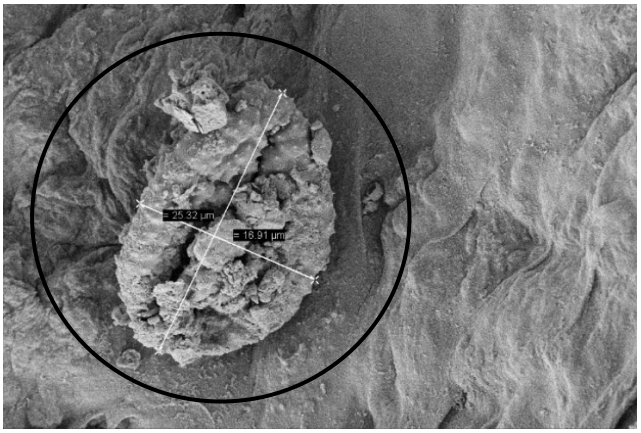

(b)

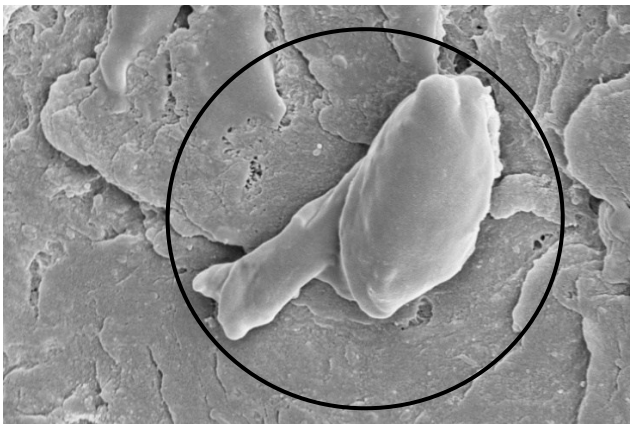

(c)

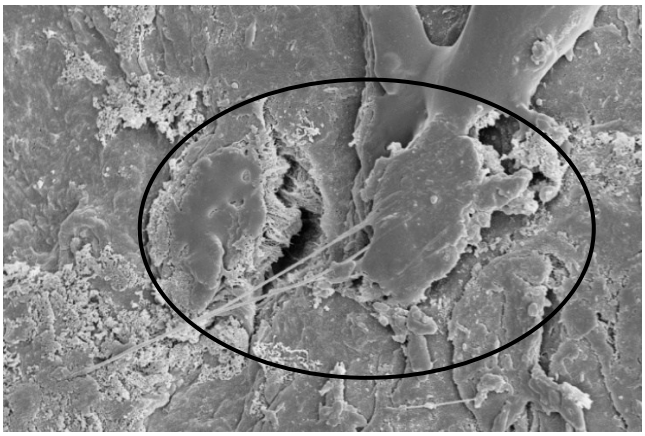

(d)

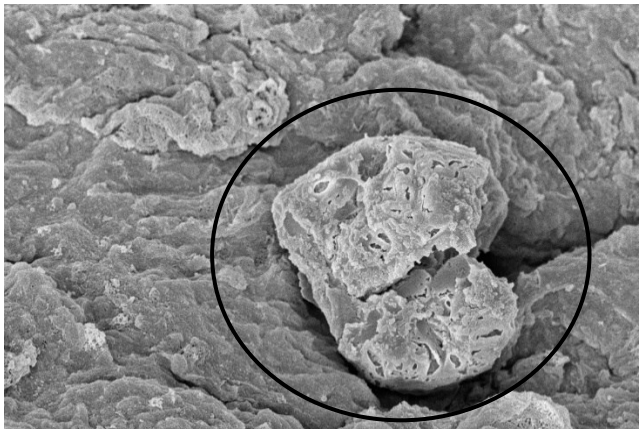

(e)

Fig. 65. SEM images of CNC-based construct with fibroblasts after 7 days of culture in vitro. Images were acquired at different magnifications and with different scale bars: (a) (x5.79 K; 2 µm), (b) (x5.33 K; 2 µm), (c) (x30.00 K; 1 µm), (d) (x10.00 K; 2 µm) and (e) (x13.92 K; 2µm). The biological structures are circled.

10. DISCUSSION

Alginate has gained a lot of attention in the research field of 3D bioprinting because of its attractive characteristics, among which biocompatibility and structural similarity to ECM. Nevertheless, it is also known to quickly lose its mechanical properties and reverse back to its soluble form, through ion exchange with monovalent cations in the physiological environment. Considering the several ways used to strengthen alginate-based hydrogels, in this work a composite hydrogel made of alginate and CNC was produced. CNC was chosen, rather than other types of biomaterials and NC, because of its availability and similarities with alginate in the chemical structure that provide good compatibility and improve the mechanical properties, through intermolecular hydrogen bonding. Specifically, CNC and alginate mixture, as bioink, has been found to promote cartilage regeneration.

Once chosen the biomaterials, an optimization procedure regarding the bioink preparation method, formulation and crosslinking strategy was adopted. It was done to identify the best bioink in terms of printability and shape fidelity, after printing and crosslinking, to be used for realizing the auricular structure. As regard the blend preparation, method 1 was discarded since it generated the bioink with the least viscosity and printability. Indeed, Fig. 28 (a2) shows a scaffold that does not resemble at all the grid shape and that is not stable, where the first layer has not managed to sustain the weight of the second one. Method 2 was rejected too. The alginate did not dissolve homogeneously in CNC-based solution, forming large and highly viscous clumps, as highlighted in Fig. 28 (b1), that were impossible to remove even by stirring. As consequence, they caused the blockage of the nozzle, leading to discontinuous and uneven filament that in turn generated a poor shaped fidelity scaffold, as can be observed in Fig. 28 (b2, b3). Thus, method 3 was selected as the best one since it allowed to obtain a blend with the right viscosity and printability, necessary to print a scaffold that resembled the model, like that in Fig. 28 (c3). Indeed, as it is shown in Fig. 28 (c2), from the nozzle a continuous and uniform filament went out.

As concern the seven bioink formulations prepared, a first selection was done by visual quality evaluation of the related printed scaffolds. 2/1, 2/3 and 2.5/3 formulations were excluded immediately since all of them were not able to reproduce the grid model, as can be seen in Fig. 32 (a, b). Even if no image of 2/3 scaffold was reported, it was very similar to 2/1. First good results were obtained with 2/4, then the accuracy was improved by increasing the alginate concentration up to 3 % w/v, as shown in Fig. 32 (c, d, e). Thus, to get a sufficiently good scaffold, the minimum quantity for CNC required is 4 % w/v, and the increment of

alginate leads to the increase in viscosity, as also illustrated in Fig. 30 and Fig. 31, so accuracy. Positive results were obtained even with 2/5 bioink (Fig. 32 (f)). As consequence, on 2/4, 2.5/4, 3/4 and 2/5 further tests were performed in order to identify the best formulation.

The evaluation of rheological properties of medical inks/gels are very important for achieving satisfactory 3D bioprinting [54]. It was observed that CNC-based inks during the printing process must exhibit shear-thinning behaviour to enable efficient flow through fine deposition nozzles, recovering a solid-like response with a sufficiently high storage modulus (G'') and yield stress (σ_y) to ensure its filamentary shape at the time of printing [55,56]. Fig. 33 shows the dependence of viscosity (Fig. 33 (a)) and stress ((Fig. 33 (b)) as function of shear rate ($\dot{\gamma}$) for commercial bioink and Alginate_CNC based formulations. The commercial and Alginate_CNC based formulations showed non-Newtonian behaviour. The apparent viscosity curves reported in Fig. 33 (a) show the dependency on shear rate ($\dot{\gamma}$). According with the literature increasing the shear rates the shear-thinning behaviour is observed, and consequently the values of shear-thinning influence the different inks printability [57]. In addition, it is important to underline that the impact of the different component and concentrations on rheological behaviour with respect to the shear rate determined a variation of viscosity characteristic. As the viscosity decreases with increasing the shear rate, all the formulations have shear-thinning characteristics [58]. The gels can be extruded for shear stress values above yield stress, σ_y, (Fig. 33 (b)) when the viscosity rapidly decreases, and the material starts to flow. The value of yield stress mainly reveals the resistance of the fluid to flow during the extrusion process, additionally this value is also directly correlated to the gel strength required to support subsequent 3D printed layers [59]. All developed formulations showed similar behaviour to the commercial product (Bioink) taken as a reference. Additionally, the developed formulations (Alginate_CNC) showed optimal printing parameters, as shown in Table 6, considered harmful for the cells above 200 kPa [53].

All the bioinks demonstrated satisfactory printing resolution, even if the best one was 3/4, followed by 2.5/4, 2/5 and 2/4. Generally, bioinks with high viscosity have higher printing precision. Indeed, 3/4 bioink was able to produce the longest and thinnest straight filament, as depicted in Fig. 34 (c1), by which the best rectilinear scaffold (20x20x1 mm, 15% infill), with a line width of 0,41 mm, was realized compared to the other bioinks (Fig. 35). Indeed, as reported in Table 8, with 3/4 bioink it was possible to realize a rectilinear scaffold with a mean line width of 0.54 mm against 2.5/4 with 0.60 mm, 2/5 with 0.60 mm and 2/4 with 1.05 mm. Particularly, for 2/4 bioink there was evidence of filaments broadening, caused by gravity

and the weight of the upper layer (Fig. 34 (a) and Fig. 35 (a)). Additionally, 3/4 successfully produced the rectilinear scaffold but with a higher infill of 25%. Nevertheless, the flow of the thin and straight filament of 3/4 formulation may not be always continuous: the high viscosity could cause the blockage of the nozzle and lead to a filament that tangles on itself. As consequence there was an uneven accumulation of bioink, shown in Fig. 34 (c2, c3). Fig. 37 highlights how the high viscosity can keep the shape of a multi-layer structure, like a rectilinear scaffold (height: 3 mm), and improve the mechanical stability. Indeed, 3/4 bioink was able to accurately sustain a structure of seven layers where the resolution was still maintained high. The corresponding scaffold had a mean height and line width of 2,97 mm and 0,46 mm respectively, the nearest to the model values, as highlighted in Table 9. Interestingly, good results were obtained with 2/5 bioink, with mean height of 2.63 mm and line width of 0.94, even if it was less viscous than 2.5/4 and 3/4. This may be justified with the capacity of CNC to provide high stability and, thus, in higher scaffolds both the resolution and the accuracy are guaranteed.

The cylindrical structure was printed to demonstrate shape stability and fidelity in the z-direction. The hollow cylinder, as described in Fig. 38, was completed only through 2/5 bioink, supporting the idea that CNC provides excellent support in the spatial network skeleton, and thereby, the shape of the scaffold is well maintained during printing. Even if, the dimensions of the printed cylinder did not respect those of the model. As concern the other three bioinks, 2/4 failed at 32^{nd} layer, 2.5/4 at 36^{th} while 3/4 failed at 36^{th} but the lower part of the cylinder remained standing. Whereas the infilled cylinder was best realized with 3/4, as can be observed in Fig. 39 (c). No evidence of filaments merging or collapsing, suggesting a dense polymer network and entanglements of polymer chains. Moreover, good shape accuracy can be observed from the top and side views of the printed structure.

Another indicator of dimensional stability is the shape fidelity post-crosslinking. Despite demonstrating good-post printing fidelity, each bioink undergoes swelling after immersion in crosslinking agent. This is mainly due to the immersion in an aqueous solution. As consequence, in the present work several strategies were adopted to reduce the changes in construct size because of the crosslinking process. Firstly, the modality of the crosslinker application was analysed and, comparing Fig. 40 (b) and (c), it was found that by providing the crosslinker, $CaCl_2$ solution, slowly starting from the peripheral border and then gradually proceeding with the infill significantly reduces the swelling of the scaffold. The high deformation of the scaffold, that happened when the crosslinker was given too fast, may be

linked to a rapid crosslinking process that leads to a formation of a reticulated external layer, much denser than the inner region that consequently absorbs water in a nonuniform way. Moreover, many studies have confirmed that this type of crosslinking process, external gelation method, can be accomplished instantaneously, but the internal crosslinking density of obtained hydrogels in unbalanced [21].

Another strategy applied to reduce the deformation of the scaffold, after immersion in $CaCl_2$ solution, was to gradually increase the concentration of alginate in the hybrid bioink, thus, from 2 % w/v up to 3 % w/v. This strategy was born taking in account that in the hybrid bioink only the alginate can crosslink with metal ions, and what happens from a chemical point of view during the crosslinking procedure. In most of the studies, that uses alginate as biomaterial, the main problem associated with ionic crosslinking is the swelling of scaffold during immersion in the aqueous solution. Indeed, alginate tends to absorb water because of its hydrophilic chemical structure and the presence of polar functional groups, hydroxyl and carboxyl ones, that form hydrogen bonds with water molecules. Alginate, when it is crosslinked with salt solutions, forms a 3D network that reduces the pores size and stabilizes the structure. Thus, the higher the degree of reticulation the lower the capacity of alginate to absorb water; increasing the alginate concentration can lead to a denser reticulated structure since the number of groups available for the reticulation is higher. Indeed, the aggregation structure of the obtained alginate-based hydrogels is strongly dependent on the composition of molecular chains: with the increase of alginate concentration, Poly-M chain tends to form dimer and highly ordered clusters by transverse bonding, whereas poly-G chains initially bound by zipper binding and then formed highly ordered clusters in higher concentration solutions [21].

The strategy was successful since 3/4, (Fig. 42), showed the least deformation (6.49 %) from the original size post-printing, after crosslinking with $CaCl_2$ (80 mM), compared to 2.5/4 (9.07 %) and 2/4 (29.96 %). There were significant differences between 2/4 and 3/4 ($p = 0.004$), 2/5 ($p = 0.0028$) and 2.5/4 (0.0098) respectively while none between 2.5/4 and 3/4. Additionally, 2/4 scaffold was the only one having some grids closed, as Fig. 41 (a) shows. Despite other studies [3, 21], it has been observed that all scaffolds were mainly subjected to shrinkage rather than swelling while being crosslinked. The scaffold immersed in a salt solution may be subjected to an osmotic gradient that leads to the loss of water entrapped in its structure. Interestingly, the minimum deviation from the original size post-printing was demonstrated by 2/5 bioink. This behaviour may be linked to the chemical structure of CNC: even if the CNC structural property underpins the affinity to absorb water, its networks demonstrate

compact nanorods packed together with relatively low porosity. Additionally, similarities in the chemical structure between alginate and CNC provide good compatibility; during crosslinking the alginate pulls the crystals together to reduce voids within the material and produce a firm structure [3, 4]. However, a greater range of values was observed in 2/5 than 2.5/4, 2/4 and 3/4, indicating a greater degree of deformation consistency post-crosslinking was achieved in the 3/4 scaffolds, also shown in Fig. 41.

The last strategy adopted to maintain the shape fidelity post-crosslinking was to modify the $CaCl_2$ solution. Even though other studies, among which [4], highlight that the higher the crosslinker concentration the higher the stability and strength of the bioink, $CaCl_2$ (300 mM) was discarded as alternative crosslinker. Fig. 43 shows how the scaffold crosslinked with $CaCl_2$ (300 mM) was the worst one because of higher reduction of the global size and swelling of the border leading to the proximal grids closure. This result was comparable to that obtained with the crosslinker provided in a fast way: the higher crosslinker concentration leaded to a rapid crosslinking resulting in an inhomogeneous structure. The best result was got with the mixed solution of $CaCl_2$ and $BaCl_2$ (Table 10) since the border of the crosslinked scaffold had the least mean width (2.12 mm) against that crosslinked with $CaCl_2$ (80 mM) (2.29 mm) and that crosslinked with $CaCl_2$ (300 mM) (2.70 mm). Furthermore, the crosslinker with barium applied on 2.5, 3/4 and 2/5, the best formulations in terms of the crosslinking effects, showed an evident reduction of post-crosslinking deformation (Fig. 45) if compared to the $CaCl_2$ (80 mM) solution, (Fig. 42): 2.5/4 (17.33 %), 3/4 (5.63 %) and 2/5 (1.74 %). The better results obtained with $CaCl_2$ mixed with $BaCl_2$ solution demonstrate the superior stability and structural integrity of the barium gel than those of calcium gel. This is a consequence of the larger radius of Ba^{++}, which is better adapted to the "egg-box" structural cavity of the hydrogel [21]. Nevertheless, barium ions are more cytotoxic than calcium ones. Thus, in this thesis a very low concentration of $BaCl_2$ was used and it was combined with $CaCl_2$, otherwise ineffective alone. Indeed, both $BaCl_2$ (1mM) and $BaCl_2$ (3mM) solutions, used alone, demonstrated incapability of crosslinking, even with prolonged time of action.

For what concerns the shape fidelity, 3/4 had the best reproducibility in grid sizes, with a more consistent mean grid area (15.12 mm^2), closer in area to the model (16 mm^2) when compared to 2.5/4 (14.92 mm^2), 2/5 (10.32 mm^2) and 2/4 (8.92 mm^2), as illustrated in Fig. 46 and Table 11. There were significantly different measurements only with 2/4 compared to 3/4 (p = 0.0010), and to 2.5/4 (p = 0.0019). Nevertheless, the path that the printhead must perform to realize the grid model combined with the higher viscosity of 3/4 and 2.5/4 prevented two lines

from reaching the border of the related scaffolds. Above all, all the bioinks demonstrated satisfactory post-printing shape fidelity.

After ethanol-drying all the bioinks showed a mean shrinkage lower than 60% (Fig. 47), 2/5 (12.77 %), 3/4 (15.25 %), 2/4 (33.67 %) and 2.5/4 (52.08 %), compared to the 90% that could have happened in case of air-drying. Additionally, no formation of wrinkles on the surface of the scaffolds were observed because of the formation of a robust polymer network due to the entanglement of CNC chains and intermolecular hydrogen bonding between alginate and CNC [34]. Furthermore, the increase of CNC portion up to 5 % w/v leaded to the least shrinkage, demonstrating the improved mechanical strength of the structure. Comparable results were obtained with 3/4. due to the denser structure deriving from the increase of alginate portion. Moreover, 3/4 showed the least range of values compared to the other bioinks, with 2.5/4 and 2/4 having the most inhomogeneous shrinkage.

The evaluation of swelling is one of the essential analyses in the 3D bioprinting field since it mainly relates to the capacity of the scaffold to uptake culture media and, thereby, supply nutrients to the cells, enhancing cells' viability and proliferation [34]. Regarding the test performed in water, all the bioinks had a good swell behaviour. Specifically, 2/4 and 2.5/4 swelled up by about 100 % in the first 5 min while 3/4 about 50 % (Fig. 48). The fast swelling may be caused by the hydrophilicity of CNC and alginate, and the presence of hydroxyl groups; the increased alginate portion in the composite resulted, as expected, in less uptake of water and in the stability reached in a shorter time, 72h. Indeed, swelling degree is usually related to the crosslinking density, consequently, it decreases as the inner structure becomes highly denser, as happened in case of 3/4 [6].

Whereas in case of the analysis in culture medium, all the four bioinks swelled up by about 100 % in the first 5 min, reaching swelling ratios around 1000 % in 72 h (Fig. 49). This faster and higher increase may be due the culture medium having higher density than water. Unexpectedly, 3/4 bioink showed an increased swelling degree with respect to 2/4. This behaviour may be linked to the presence of the culture medium that, differently from water, is reached in physiological ions that promote the exchange with Ca^{++} ions reducing the crosslinking degree, so facilitating the absorption of water. 2/5, 2.5/4 and 2/4 showed a similar behaviour, but the first two ones reached lower swelling ratios. This reduction, in case of 2/5, can be a consequence of the denser network structure, as previously observed, obtained from hydrogen bonding and characterized by smaller compact pores restricting the penetration of water molecules [34]. Nevertheless, 2/5 scaffold, differently from the others, was the only one

that lost its shape 72 h after immersion in culture medium (Fig. 51, Fig. 52, Fig. 53 and Fig. 54). This was a consequence of the increased portion of CNC that, despite it cooperates in the construction of the structure, it does not crosslink with salt solutions unless it is chemically treated. The stability and the more compact porosity provided by crosslinking 3/4 scaffold with the mixed solution was observed also during the swelling test: the composite crosslinked with the mixed solution started to stabilize just after 1 h and reached a maximum swelling ratio around the half of that of the scaffold crosslinked with $CaCl_2$ solution (Fig. 50).

About the results obtained from the degradation test, 2/4, 2.5/4 and 3/4 did not reveal gel release neither 7 days nor 14 days after immersion in culture medium (Table 15). Even if the test was conducted at room temperature rather than physiological one (37°), other studies, like [6], have noticed a controlled degradation behaviour over the time of the NC and Alginate-based scaffolds. Indeed alginate, although once crosslinked through calcium ions tends to dissolve in water because of the replacement of calcium ions by monovalent cations, when it is crosslinked with CNC, because of the entanglement between the molecular chains, shows crosslink networks more stable and so it could exist for a long time. Consequently, the reduced crosslinked portion in 2/5 made it release 41.32% of gel just after 7 days (Table 15). The test at 37°, performed with 3/4, resulted in only 38.45 % of gel release, 7 days after immersion in culture medium, against 62.50 % of alginate and gelatine-based scaffolds [37] and 45% of alginate and chitosan-based scaffolds [60]. Moreover, at the end of the test, the scaffold apparently did not show the loss of its shape and elastic properties (Fig. 55).

Because of the obtained results, principally in terms of stability, shape fidelity and resolution, 3/4 bioink was chosen to print the auricle structure. The ear model provided by the laser scanner was rejected since it slightly resembled the human ear, differently from the model available on the bioprinter library. The laser scanner, although a powerful instrument, demonstrated not to be idoneous for detailed human body parts and that cannot be captured at 360°, like the ear. Even if the auricle structure was successful printed, characterized by high shape fidelity and stability, after the crosslinking it was subjected to shrinkage as also happened with the simple scaffolds (Fig. 58). Differently, it was observed that only the external part was crosslinked while the internal one remained in gel form. This represents the big disadvantage of ionic crosslinking, especially when structures with high volume are involved: the outer portion is the first to be crosslinked preventing the crosslinker to act even in the inner structure.

In this work the formulation 3/4 showed a good rheological parameter and good printability of fundamental importance for medical regenerative applications. Thus, 3/4 was selected to print with the cells. The viscosity of the material, as expected, changed after the mixing with cells but still allowing the realization of a stable structure (Fig. 59). Additionally, the shape of the cell-laden scaffold was maintained after 6 days of immersion in culture medium, demonstrating the validity of the degradation tests done before.

The microscopy analysis demonstrated the sustained capacity of the CNC-based scaffold to promote cellular adhesion, growth and aggregation. Indeed, optical microscopy analysis provided an initial view of cell distribution within the substrate just after 1 day (Fig. 60). Increase in cell density was observed in 6 days: Fig. 61 shows cell aggregation indicating that the gel provided a supportive matrix for cell growth. Further analysis was conducted through DAPI staining and H&S. The fluorescence highlighted by DAPI allowed the nucleus of the cells to be identified, helping to confirm their viability and health within the bioink (Fig. 63). Haematoxylin, a blue-purple dye, binds to nucleic acids, marking the cell nuclei, while eosin imparts a pink hue to proteins; this combination allowed for visualization of tissue architecture, nuclei appeared blue while the cytoplasm and extracellular matrix varied in shades of pink (Fig. 62). Nevertheless, the opacity of the material was an obstacle in these types of observation and consequently the cells and their structures were not clearly distinguished. Differently, through SEM analysis it was possible to clearly identify cellular structures confirming the biocompatibility and bioactivity of the matrix. External structure and slightly the internal structure were observed, as being recognized as important factors for defining cellular behaviour [33]. Fig. 64 (a) shows well defined fibrous structures on the surface of the compact scaffold, while a more porous internal structure with channel-like arrangement suggesting that proper oxygen and nutrients transport can be ensured for achieving high cell viability and proliferation [33]. Indeed, Fig. 65 highlights individual cells and aggregation of cells whose shape resembles that of the fibroblasts: big and fusiform cells that often show sparse and thin ramifications [9]. It was possible to identify a structure with dimensions (25.32x16.91 μm) compatible with a compact spheroid formed by more cells (Fig. 65 (a,b)), a singular cell (Fig. 65 (c)), a singular cell with cytoplasmatic bridges (Fig. 65 (d)) and a portion of internal cellular structure (Fig. 65 (e)). These results suggested that the cells were responding favourably to the environment.

CONCLUSION

Auricle reconstruction is generally intended as auricular cartilage regeneration. The engineering of auricular cartilage construct remains challenging due to the lack of regenerative cells and limited mechanical integrity as well as the detailed anatomy. Hence, 3D bioprinting, by precisely placing biomaterials with living cells in 3D space according to a digital model, represents a potential technique to improve the regenerative performance of accurate engineered tissue products, like the external ear.

The current study developed a series of hydrogels composed of alginate and CNC as potential bioinks for printing 3D objects via the pneumatic extrusion-based technique. The primary goal was to identify the bioink with the best printability, stability and shape fidelity, post-printing and post-crosslinking, necessary to realize an accurate auricular structure. Secondary, the selected bioink was analysed if had a suitable behaviour in the physiological environment, absorbing nutrients while promoting fibroblasts viability and proliferation, and had a controlled degradation behaviour allowing the formation of neo-tissue. Starting from the minimum concentrations of alginate and CNC to have a good printability, even if 2/4, 2.5/4, 3/4 and 2/5 all showed satisfactory results, the increase of alginate rather than CNC revealed as the best strategy. Indeed, despite higher concentration of CNC demonstrated better stability, through 3/4 it was possible to print high stable geometries composed of 7 layers and 36 layers while maintaining high resolution and shape fidelity, thanks to its higher viscosity also highlighted by the rheological analysis. Despite its higher viscosity, 3/4 was printed at an acceptable pressure not dangerous for cells. Thus, the bioink was used to print the auricle and with cells. Different properties of the developed scaffolds were evaluated, and it was found that their swelling ratio and degradation rate were in line with those required for soft tissue engineering applications. All the four bioinks showed an increasing swelling ratio around the first minutes and it stabilized within 72 h, reaching values up to 1200 %. Nevertheless, more tests might be needed to identify the target behaviour of each formulation in culture medium at room and physiological temperatures. About the degradation property, due to a huge portion not crosslinked, 2/5 bioink started to release gel just at room temperature in 7 days after immersion in culture medium. Differently from 3/4 that remained stable at room temperature up to 14 days and released less than the half of the gel in 7 days at 37°. This demonstrated high compact structure provided by the combination of alginate with CNC. CNC-based scaffolds demonstrated slightly shape deformation after ionic crosslinking. Anyway, the increase in alginate concentration provided better results and the addition of $BaCl_2$ in $CaCl_2$ solution revealed much more strength and stability in the scaffolds, even during immersion in culture medium.

The results obtained with microscopy analysis demonstrated the potential use of NC for 3D bioprinting of living tissues and organs, despite its opacity that limited the optical observation. Whereas with SEM it was possible to clearly attest forms of cellular attachment and proliferation.

Another relevant aspect is the economic advantage of the prepared bioinks over commercially available bioinks. The in-house formulation of bioinks provided a cost-effective solution, allowing direct control over raw materials and reducing the costs associated with sourcing commercial bioinks. This aspect, coupled with the observed performance in rheological, morphological and cell proliferation properties, gave, principally to the selected bioink (3/4), a dual advantage.

In summary, the results highlighted the potential of the investigated cost-effective bioink as hydrogel for 3D bioprinting with living cells for growth of cartilage tissue. To sustain the suitability of the composite for auricle reconstruction further investigations are required: it must be analysed if chondrocytes might have the same good behaviour of fibroblasts and mechanical tests must be performed to identify if the hydrogel is able to withstand external compressive loads which a normal ear is generally exposed to.

In future studies, the fibroblasts activity in the NC-based bioink together with the bioprinter multiple-heads system could be exploited to realize the external ear with all its components: fat, cartilage and skin tissues. Furthermore, given the capacity of alginate, once chemically modified, to photopolymerize, the stability and the shape fidelity post-crosslinking of the scaffolds could be optimized using UV rather than metal ions for crosslinking.

References

[1] Kim M, Kim YJ, Kim YS, Roh TS, Lee EJ, Shim JH, Kang EH, Kim MJ, Yun IS. One-Year Results of Ear Reconstruction with 3D Printed Implants. Yonsei Med J. 2024 Aug; 65(8): 456-462.

[2] Griffin MF, Premakumar Y, Seifalian AM, Szarko M, Butler PE. Biomechanical Characterisation of the Human Auricular Cartilages; Implications for Tissue Engineering. Ann Biomed Eng. 2016 Dec; 44(12): 3460-3467.

[3] Thomas H. Jovic, Tamsin Nicholson, Hari Arora, Kim Nelson, Shareen H. Doak, Iain S. Whitaker. A comparative analysis of pulp-derived nanocelluloses for 3D bioprinting facial cartilages. Carbohydrate Polymers. 2023 Dec; 321.

[4] Jessop ZM, Al-Sabah A, Gao N, Kyle S, Thomas B, Badiei N, Hawkins K, Whitaker IS. Printability of pulp derived crystal, fibril and blend nanocellulose-alginate bioinks for extrusion 3D bioprinting. Biofabrication. 2019 Jul 8; 11(4): 045006.

[5] Jiang, Ruifang & Wang, Guo & Zhang, Jing & Zhang, Xinzhi & Zhou, Lian & Xu, Tao. Three-dimensional bioprinting of auricular cartilage: A review. Medicine in Drug Discovery. 2020 Feb 1; 3: 100016.

[6] Lafuente-Merchan M, Ruiz-Alonso S, Zabala A, Gálvez-Martín P, Marchal JA, Vázquez-Lasa B, Gallego I, Saenz-Del-Burgo L, Pedraz JL. Chondroitin and Dermatan Sulfate Bioinks for 3D Bioprinting and Cartilage Regeneration. Macromol Biosci. 2022 Mar; 22(3): e2100435.

[7] Khan N, Zaki DP, Brown WE, Halaseh FF, Willette D, Ziegler M, Athanasiou KA, Widgerow AD. Tissue Engineering Auricular Cartilage: A Review of Auricular Cartilage Characteristics and Current Techniques for Auricular Reconstruction. J Craniofac Surg. 2024 Mar 5.

[8] Karamanos, Nikos & Theocharis, Achilleas & Piperigkou, Zoi & Manou, Dimitra & Passi, Alberto & Skandalis, Spyros & Vynios, Demitrios & Orian-Rousseau, Véronique & Ricard-Blum, Sylvie & Schmelzer, Christian & Duca, Laurent & Durbeej, Madeleine & Afratis, Nikolaos & Troeberg, Linda & Marco, Franchi & Masola, Valentina & Onisto, Maurizio. A guide to the composition and functions of the extracellular matrix. The FEBS Journal. 2021 Mar; 288.

[9] Kenneth S. Saladin. Anatomia Umana. 2017. Piccin.

[10] Abdalla, M. K. T. M. Applied Basic Science of the Auricular Cartilage. InTech. 2018.

[11] Wang Haonan, Yu Huaqing, Zhou Xia, Zhang Jilong, Zhou Hongrui, Hao Haitong, Ding Lina, Li Huiying, Gu Yanru, Ma Junchi, Qiu Jianfeng, Ma Depeng. An Overview of Extracellular Matrix-Based Bioinks for 3D Bioprinting. Frontiers in Bioengineering and Biotechnology. 2022; 10.

[12] Ibrahim T. Ozbolat, Weijie Peng, Veli Ozbolat. Application areas of 3D bioprinting. Drug Discovery Today. 2016 Aug; 21(8): 1257-1271.

[13] Rodrigo A. Rezende, Vladimir Kasyanov, Vladimir Mironov, Jorge Vicente Lopes da Silva. Organ Printing as an Information Technology. Procedia Engineering. 2015; 110: 151-158.

[14] Huang, Ying & Zhang, Xiao-Fei & Gao, Guifang & Yonezawa, Tomo & Cui, Xiaofeng. 3D bioprinting and the current applications in tissue engineering. Biotechnology Journal. 2017 Jul; 12.

[15] Yong He, Mingjun Xie, Qing Gao, Jianzhong Fu. Why choose 3D bioprinting? Part I: a brief introduction of 3D bioprinting for the beginners. Bio-Design and Manufacturing. 2019 Nov 1; 2: 221-224.

[16] He, Y., Gu, Z., Xie, M. *et al.* Why choose 3D bioprinting? Part II: methods and bioprinters. Bio-des. Manuf. 2020 Feb 1; 3: 1-4.

[17] Tao Zhang, Wei Zhao, Zijie Xiahou, Xingwang Wang, Kunxi Zhang, Jingbo Yin. Bioink design for extrusion-based bioprinting. Applied Materials Today. 2021 Dec; 25.

[18] Selwa Boularaoui, Ghada Al Hussein, Kamran A. Khan, Nicolas Christoforou, Cesare Stefanini. An overview of extrusion-based bioprinting with a focus on induced shear stress and its effect on cell viability. Bioprinting. 2020 Dec.

[19] Rodrigo Curvello, Vikram Singh Raghuwanshi, Gil Garnier. Engineering nanocellulose hydrogels for biomedical applications. Advances in Colloid and Interface Science. 2019 May; 267: 47-61.

[20] Giuseppe MD, Law N, Webb B, A Macrae R, Liew LJ, Sercombe TB, Dilley RJ, Doyle BJ. Mechanical behaviour of alginate-gelatin hydrogels for 3D bioprinting. J Mech Behav Biomed Mater. 2018 Mar; 79: 150-157.

[21] Junyan Tan, Yuning Luo, Yuqiong Guo, Yue Zhou, Xinying Liao, Dingxilei Li, Xinyi Lai, Yang Liu. Development of alginate-based hydrogels: Crosslinking strategies and biomedical applications. International Journal of Biological Macromolecules. 2023 June 1; 239.

[22] Xingchen Yang, Zhenhui Lu, Huayu Wu, Wei Li, Li Zheng, Jinmin Zhao. Collagen-alginate as bioink for three-dimensional (3D) cell printing based cartilage tissue engineering. Materials Science and Engineering: C. 2018 Feb 1; 83: 195-201.

[23] Ibrahim, Eman Assem; Sarhan, Moamen Mohsen[1]; Ezzelarab, Salah; Marei, Mona K. A scoping review on the potential of three-dimensional bioprinting in auricular cartilage regeneration. SRM Journal of Research in Dental Sciences. 2024 Jul-Sep; 15(3): 111-120.

[24] Héctor Martínez Ávila, Silke Schwarz, Nicole Rotter, Paul Gatenholm. 3D bioprinting of human chondrocyte-laden nanocellulose hydrogels for patient-specific auricular cartilage regeneration. Bioprinting. 2016 Mar-Jun; 1-2: 22-35.

[25] Müller M, Öztürk E, Arlov Ø, Gatenholm P, Zenobi-Wong M. Alginate Sulfate-Nanocellulose Bioinks for Cartilage Bioprinting Applications. Ann Biomed Eng. 2017 Jan; 45(1): 210-223.

[26] Monika Hospodiuk, Madhuri Dey, Donna Sosnoski, Ibrahim T. Ozbolat. The bioink: A comprehensive review on bioprintable materials. Biotechnology Advances. 2017 Mar-Apr; 35 (2): 217-239.

[27] Barnes, H.A., Hutton, J.F., Walters, K.: An introduction to rheology. Elsevier, Amsterdam, 1989.

[28] Macosko, C.W. Rheology, principles, measurements, and applications. Wiley. 1994.

[29] Mario Chopin-Doroteo, Edna Ayerim Mandujano-Tinoco, Edgar Krötzsch. Tailoring of the rheological properties of bioinks to improve bioprinting and bioassembly for tissue replacement. Biochimica et Biophysica Acta (BBA) - General Subjects. 2021 Feb; 1865 (2): 129782.

[30] Mezger, T.G. The Rheology-Handbook. Vincentz. 2014.

[31] Schwab A, Levato R, D'Este M, Piluso S, Eglin D, Malda J. Printability and Shape Fidelity of Bioinks in 3D Bioprinting. Chem Rev. 2020 Oct 14; 120(19): 11028-11055.

[32] Reda M. Felfel, Mark J. Gideon-Adeniyi, Kazi M. Zakir Hossain, George A.F. Roberts, David M. Grant. Structural, mechanical and swelling characteristics of 3D scaffolds from chitosan-agarose blends. Carbohydrate Polymers. 2019 Jan 15; 204: 59-67.

[33] M. Lafuente-Merchan, S. Ruiz-Alonso, A. Espona-Noguera, P. Galvez-Martin, E. López-Ruiz, J.A. Marchal, M.L. López-Donaire, A. Zabala, J. Ciriza, L. Saenz-del-Burgo, J.L. Pedraz. Development, characterization and sterilisation of Nanocellulose-alginate-(hyaluronic acid)- bioinks and 3D bioprinted scaffolds for tissue engineering. Materials Science and Engineering: C. 2021 July; 126: 112160.

[34] Hossein Baniasadi, Erfan Kimiaei, Roberta Teixeira Polez, Rubina Ajdary, Orlando J. Rojas, Monika Österberg, Jukka Seppälä. High-resolution 3D printing of xanthan gum/nanocellulose bio-inks. International Journal of Biological Macromolecules. 2022 June 1; 209: 2020-2031.

[35] Sahai N, Gogoi M, Tewari RP. 3D Printed Chitosan Composite Scaffold for Chondrocytes Differentiation. Curr Med Imaging. 2021; 17 (7): 832-842.

[36] Laurean Dalton, Robin Young. Fundamentals of Cell Biology. Oregon State University. 2024.

[37] Schwarz S, Kuth S, Distler T, Gögele C, Stölzel K, Detsch R, Boccaccini AR, Schulze-Tanzil G. 3D printing and characterization of human nasoseptal chondrocytes laden dual crosslinked oxidized alginate-gelatin hydrogels for cartilage repair approaches. Mater Sci Eng C Mater Biol Appl. 2020 Nov; 116: 111189.

[38] Elliott AD. Confocal Microscopy: Principles and Modern Practices. Curr Protoc Cytom. 2020 Mar; 92(1): e68.

[39] Apelgren P, Amoroso M, Säljö K, Lindahl A, Brantsing C, Stridh Orrhult L, Gatenholm P, Kölby L. Skin Grafting on 3D Bioprinted Cartilage Constructs In Vivo. Plast Reconstr Surg Glob Open. 2018 Sep 14; 6(9): e1930.

[40] Visscher DO, Lee H, van Zuijlen PPM, Helder MN, Atala A, Yoo JJ, Lee SJ. A photo-crosslinkable cartilage-derived extracellular matrix bioink for auricular cartilage tissue engineering. Acta Biomater. 2021 Feb; 121: 193-203.

[41] Otto IA, Capendale PE, Garcia JP, de Ruijter M, van Doremalen RFM, Castilho M, Lawson T, Grinstaff MW, Breugem CC, Kon M, Levato R, Malda J. Biofabrication of a shape-stable auricular structure for the reconstruction of ear deformities. Mater Today Bio. 2021 Jan 21; 9: 100094.

[42] Ahmed Salisu, Mohd Marsin Sanagi, Ahmedy Abu Naim, Wan Aini Wan Ibrahim, Khairil Juhanni Abd Karim. Removal of lead ions from aqueous solutions using sodium alginate-graft-poly(methyl methacrylate) beads. Desalination and Water Treatment. 2016 July; 57(3): 15353-15361.

[43] Tezar Ramdhan, Su Hung Ching, Sangeeta Prakash, Bhesh Bhandari. Physical and mechanical properties of alginate based composite gels. Trends in Food Science & Technology. 2020 Dec; 106: 150-159.

[44] Chung JHY, Naficy S, Yue Z, Kapsa R, Quigley A, Moulton SE, Wallace GG. Bio-ink properties and printability for extrusion printing living cells. Biomater Sci. 2013 Jul 4; 1(7): 763-773.

[45] Markstedt, Kajsa & Mantas, Athanasios & Tournier, Ivan & Martínez Ávila, Héctor & Hägg, Daniel & Gatenholm, Paul. 3D Bioprinting Human Chondrocytes with Nanocellulose–Alginate Bioink for Cartilage Tissue Engineering Applications. Biomacromolecules. 2015 Mar 25; 16.

[46] Osong, S.H., Norgren, S. & Engstrand, P. Processing of wood-based microfibrillated cellulose and nanofibrillated cellulose, and applications relating to papermaking: a review. Cellulose. 2015 Oct 27; 23: 93–123.

[47] Charreau H, Foresti ML, Vazquez A. Nanocellulose patents trends: a comprehensive review on patents on cellulose nanocrystals, microfibrillated and bacterial cellulose. Recent Pat Nanotechnol. 2013 Jan; 7(1): 56-80.

[48] Lavoine N, Desloges I, Dufresne A, Bras J. Microfibrillated cellulose - its barrier properties and applications in cellulosic materials: a review. Carbohydr Polym. 2012 Oct 1; 90(2): 735-64.

[49] Lin L, Jiang S, Yang J, Qiu J, Jiao X, Yue X, Ke X, Yang G, Zhang L. Application of 3D-bioprinted nanocellulose and cellulose derivative-based bio-inks in bone and cartilage tissue engineering. Int J Bioprint. 2022 Nov 9; 9(1): 637.

[50] Boufi S, González I, Delgado-Aguilar M, Tarrès Q, Pèlach MÀ, Mutjé P. Nanofibrillated cellulose as an additive in papermaking process: A review. Carbohydr Polym. 2016 Dec 10; 154: 151-66.

[51] Rodrigo Felipe Santos, José Carlos Lopes Ribeiro, José Maria Franco de Carvalho, Washington Luiz Esteves Magalhães, Leonardo Gonçalves Pedroti, Gustavo Henrique Nalon, Gustavo Emilio Soares de Lima. Nanofibrillated cellulose and its applications in cement-based composites: A review. Construction and Building Materials. 2021 June 21; 288: 123122.

[52] Abasalizadeh F, Moghaddam SV, Alizadeh E, Akbari E, Kashani E, Fazljou SMB, Torbati M, Akbarzadeh A. Alginate-based hydrogels as drug delivery vehicles in cancer treatment and their applications in wound dressing and 3D bioprinting. J Biol Eng. 2020 Mar 13; 14: 8.

[53] https://www.cellink.com/bioprinting/bio-x-3d-bioprinter/

[54] Dorishetty, Pramod, Rajkamal Balu, Amy Gelmi, Jitendra P. Mata, Naba K. Dutta, and Namita Roy Choudhury. 3D printable soy/silk hybrid hydrogels for tissue engineering applications. Biomacromolecules. 2021; 22(9): 3668-3678.

[55] Gilberto Siqueira, Dimitri Kokkinis, Rafael Libanori, Michael K. Hausmann, Amelia Sydney Gladman, Antonia Neels, Philippe Tingaut, Tanja Zimmermann, Jennifer A. Lewis, André R. Studart. Cellulose nanocrystal inks for 3D printing of textured cellular architectures. Advanced Functional Materials. 2017; 27(12): 1604619.

[56] Studart, A. R. Additive manufacturing of biologically-inspired materials. Chemical Society Reviews. 2016; 45(2): 359-376.

[57] Bercea M. Rheology as a Tool for Fine-Tuning the Properties of Printable Bioinspired Gels. Molecules. 2023; 28(6): 2766.

[58] Habib, M. A., & Khoda, B. Rheological analysis of bio-ink for 3D bio-printing processes. Journal of manufacturing processes. 2022; 76: 708-718.

[59] Sakr MA, Sakthivel K, Hossain T, Shin SR, Siddiqua S, Kim J, Kim K. Recent trends in gelatin methacryloyl nanocomposite hydrogels for tissue engineering. J Biomed Mater Res A. 2022 Mar; 110(3): 708-724.

[60] Liu Q, Li Q, Xu S, Zheng Q, Cao X. Preparation and Properties of 3D Printed Alginate–Chitosan Polyion Complex Hydrogels for Tissue Engineering. Polymers. 2018; 10(6): 664.